OPTICAL WAVEGUIDE CHARACTERISATION OF HYBRID ALIGNED NEMATIC LIQUID CRYSTAL CELLS

Submitted by

Sharon Ann Jewell

To the University of Exeter as a thesis for the degree of Doctor of Philosophy in Physics, December 2002.

This thesis is available for Library use on the understanding that it is copyright material and that no quotation from the thesis may be published without proper acknowledgement.

I certify that all material in this thesis which is not my own work has been identified and that no material has previously been submitted and approved for the award of a degree by this or any other University.

……..... (signature)

Abstract

In an era where the demand for high quality liquid crystal devices is continually growing, the displays industry is constantly striving to provide more compact and efficient displays. It is only by understanding how well a particular alignment technique works or how quickly the director responds to a change in voltage, that the current high standard of displays can be improved upon.

In this thesis, highly powerful optical wave-guide techniques have been used to study the director profile and hence explore the fundamental physics associated with the commercially significant hybrid aligned nematic (HAN) liquid crystal geometry in various static and dynamic situations.

The fully-leaky guided mode technique has been used to explore the flexoelectric effect in HAN cells. The high sensitivity of this optical waveguide technique has enabled the subtle differences in the director profiles produced by forward and reverse bias dc voltages of equal magnitude to be ascertained. By then comparing this information with model data from a free-energy minimisation modelling program that has been produced, the sum of the splay and bend flexoelectric coefficients for E7 have been determined. This study also indicated the presence of surface polarisation at the homeotropic surface, which has been quantified and attributed to preferential alignment of dipolar liquid crystal molecules. A further static study was undertaken using polarimetry to evaluate the surface anchoring strength in a HAN cell filled with a material of negative dielectric anisotropy.

The dynamics of a HAN cell when voltages are both applied and removed have been measured for the first time, using an optical convergent beam technique. In both cases, collecting data on a sub-millisecond time-scale has enabled backflow to be observed during the initial re-orientation of the director. These measured profiles show excellent agreement with model profiles generated using a nematodynamics modelling code based on the Leslie-Eriksen-Parodi theory of nematodynamics and the viscosities of ZLI-2293 have been determined. The flow within the cell has also been modelled, and the influence of each of the viscosity coefficients on the dynamics of the system has been investigated.

Contents

Index of Figures

Index of Tables

Acknowledgements

As is traditional, I would like to take this opportunity to thank the many people who have made the past three years work so fulfilling and enjoyable. Firstly, I would like to thank my supervisor, Professor Roy Sambles for having confidence in me when at times I didn't. It has been a privilege to work with him, and his boundless enthusiasm has been inspirational. Thank you also to my CASE supervisor at Hewlett-Packard, Chris Newton and to Adrian Geisow for many useful discussions during my visits to Bristol. I'm also grateful to fellow HP workers Steve Kitson for providing me with enough ITO glass to glaze a greenhouse, and to Susanna Klein for showing me how BLCS talks *should* be done! A special thank you also goes to Ben Hodder, firstly for showing me the ropes in the early days of my PhD in Exeter, and then later on at HP for his help in collecting and fitting the Stokes' parameters data used in chapter 5.

A huge thank you goes to the convergent beam guru Nathan Smith for all his help and humour in the early days, and for being just an e-mail away when a query on dentist's drills or CCD arrays arose – you still owe me for BLCS 2002 though! My sincere thanks also goes to Fuzi Yang for his advice when I was getting to grips with the static measurements, and to fellow convergent-beam convert Lizhen Ruan. The liquid crystal team has also been enriched over the past few years by visits from Giusy Scalia and Vincenzo Bruno, and the new "phase" of liquid crystal recruits John Birkett and James Suckling look set to continue in the same spirit.

The unique atmosphere in group 20 has made working in the basement a real joy. Thank you to the two veterans - Mike Jory for giving me sound advice (sorry for ignoring most of it though) and ridicule in equal measure and to Pete V for rating the heat, despite usually instigating it. When it comes to harshness levels though, no one rivals Ian Hooper. However, hearing comments about my clothing every time I step into the office, from the man who thinks style is something used to climb over a fence really does take the biscuit (or brownie). Seriously though, thanks for all our discussions on optics and for proof reading this thesis. Thank you also to cute Jimi Kerslake for valiantly ensuring that no faux-pas (particularly during our attempt to

raise the “profile” of HAN cells in Edinburgh) has “scone” unridiculed. The fact that it’s usually justified *is not the point*. My education has been completed by Alastair Hibbins and Matt Lockyear who have taught me about humour well below levels that I previously thought existed. Cheers also to former G20 members Hazel Went for her cooking and appreciation of penguins and Nobuharu Okazaki for his surreal words of wisdom.

The members past and present of G13, led by Professor Bill Barnes, deserve a mention, and it is at this point that I feel that I should confess that any equipment that went missing over the past three years was probably borrowed by me. A huge thank you to Piers Andrew - despite the countless times that I’ve asked for his help, the only cross words between us have been in the Telegraph. Liquid crystal convert Phil Worthing has provided many laughs – sometimes even intentionally, and now that he has left I can finally wear purple in safety. I’ve also enjoyed my discussions with Pete Hobson comparing and contrasting OLEDS and liquid crystals – maybe one day he’ll admit that I’m right. Steve Wedge’s caustic wit and reassurances every Tuesday that “it looks better on the screen”, and Simon Garrett on “cleanroom fm” have also both provided much entertainment. The group atmosphere would not be complete without Andy Murray, the guy who never stops smiling, along with Jon Wasey, Simion Astilean and Lucy Smith.

This thesis would certainly not have been completed without the technical support that I have received from many areas. Firstly, thank you to Pete Cann for whom no job is too big and no request is too vague. Thanks also to Dave Jarvis for countless silicon monoxide evaporations, and to all of the other members of the workshop who have undoubtedly helped at times. Thanks also to Phil Vossler and the electronics workshop for help with all things computer related. I would also like to thank Professor John Inkson for the use of the department resources, and the secretarial staff for helping to keep paperwork to a minimum.

Last but certainly not least I would like to thank my parents for their constant supply of love, support and chocolate cake. I would also like to take this opportunity to apologise to my sister, Vicki, for doing such a conversation-stopping subject, and I promise that I will get a proper job now.

Chapter 1

The Liquid Crystalline Phase and Hybrid Aligned Nematic Cells

1.1 Introduction

In today's society, the ability to send and receive data on the move has become part of everyday life. The increase in the volume and complexity of the information sent in this way has inevitably lead to increasing demands on the displays used to access it.

Up until the end of the last century, the cathode ray tube (CRT) had adequately met the display requirements of non-portable devices, such as televisions and computers. However, this bulky and inefficient technology is totally incompatible with modern, compact portable devices. Over the past two decades, the use of liquid crystal displays for these purposes has steadily increased. The improvements and developments since the first liquid crystal display was developed in the 1970's have established the liquid crystal display as an alternative to traditional CRT devices.

Liquid crystal displays are yet to fulfil their full potential though, with areas such as power consumption, switching speed and viewing angle still in need of improvement. To enable this to happen, a thorough understanding of the underlying physics associated with these devices is crucial.

In this chapter, the fundamental properties of liquid crystals are discussed with particular emphasis on nematic liquid crystals. A brief description of liquid crystal displays along with techniques used to fabricate test cells is then given. Finally, the hybrid aligned nematic (HAN) cell structure, which has been explored in detail in this thesis is discussed, and its commercial uses in the new generation of bistable, low power displays is emphasised.

1.2 The Liquid Crystalline Phase of Matter

The liquid crystalline phase is a general term for a collection of mesophases that can occur in certain materials composed of anisotropic organic molecules. This "fourth state of matter" as it is sometimes referred to was first reported by Reinitzer (1888) and Lehmann (1890). These phases all posses a level of fluidity consistent with the liquid state of matter, but unlike in a fluid, the molecules form a partially ordered system where they tend to align with each other on a macroscopic scale. All liquid crystals fall into one of two groups:

- *Lyotropic* liquid crystals form a liquid crystalline phase when dissolved in a given solvent over a particular concentration range.
- *Thermotropic* liquid crystals form the liquid crystal phase between the solid and liquid states, with the transition occurring over a particular temperature range.

It is the thermotropic class of liquid crystals that are used in display devices, and will be the focus of the remainder of this thesis.

1.3 Thermotropic Liquid Crystals

Thermotropic liquid crystals can be categorised into one of three groups, depending on the nature of the composite molecule (Collings and Hird, 1998):

- *Calamitic* liquid crystals are generally composed of rod-like molecules with one axis longer than the other two and tend to align with their long axes parallel.
- *Discotic* liquid crystals are generally disc-shaped and have one axis shorter than the other two. These molecules tend to align by stacking on top of each other.
- *Polymeric* liquid crystals are composed of long-chain molecules.

Calamitic liquid crystals are commonly used in display applications, and early work by Freidel (1922) determined that calamitics can be further sub-divided into three classes, depending on the degree of order present.

- *Nematics* are the least-ordered phase, where the molecules tend to align in the same direction, but the centres of mass of the molecules are randomly distributed throughout the sample.
- *Smectics* tend to have an increased degree of order in the direction parallel to the long axis of the molecule causing 'layers' (actually a density wave) to form in the sample. The smectic phase is further classified by the degree of orientational alignment within each layer
- *Cholesterics* are essentially nematics that are composed of optically active molecules which arrange themselves in a helical structure with its axis normal to the alignment direction.

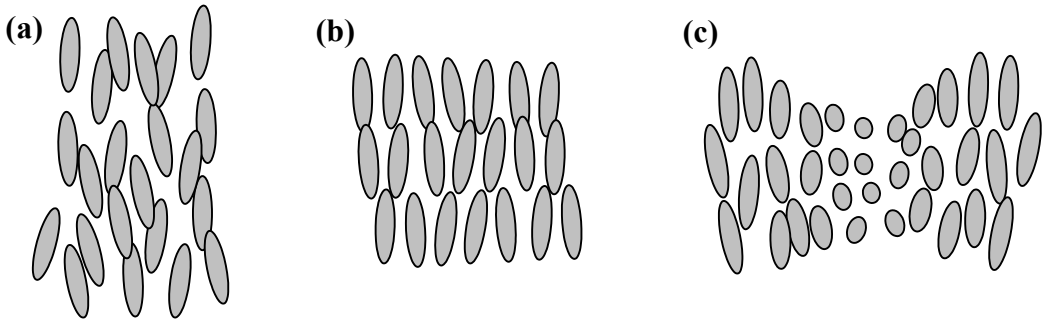

Fig. 1.1 Schematic diagram of the general alignment of molecules in (a) the nematic phase; (b) the smectic phase and (c) the cholesteric phase.

Although all three classes of liquid crystal have uses in the displays industry, this work is primarily concerned with nematic liquid crystals, and so the properties of these compounds will be focussed on in the next section.

1.4 The Nematic Phase

As is common with all liquid crystals, the nematic phase has orientational order, but no positional order. The liquid crystal molecules are uniaxial in shape - one axis (the extra-ordinary axis, denoted by the subscript $_{//}$) is longer than the other two (the ordinary axes denoted by $_{\perp}$) and the dimensions of the liquid crystal molecule is typically 5Å by 20Å.

The actual orientation of each molecule in a macroscopic region will vary slightly and thermal fluctuations cause this to change with time. Therefore, the average orientation of the molecules is denoted by a unit vector **n**. This is known as the director, and refers to a macroscopic region of the liquid crystal, rather than to individual molecules. Due to the symmetry of the uniaxial liquid crystal molecules, the directions of +**n** and –**n** are equivalent.

The amount of orientational order present in a macroscopic sample can be defined by the order parameter of the system (Tsvetkov, 1942). The order parameter can take any value between 0 (completely random orientation) and 1 (all molecules parallel to the director). This is calculated from:

$$S = \frac{1}{2}\left\langle 3\cos^2\theta - 1 \right\rangle \qquad \text{Eq. 1.1}$$

where θ is the angle between the director and the molecule, and the brackets denote an average taken over many molecules at an instance in time.

1.4.1 Optical Anisotropy

The anisotropic shape of nematic liquid crystal molecules results in the refractive index associated with light polarised parallel to the director ($n_{//}$, the extra-ordinary refractive index) being different to that of light polarised perpendicular to it ($n_{\perp}$, the ordinary refractive index) (de Jeu, 1980). This birefringence is the fundamental optics which is exploited in all liquid crystal displays, and will be discussed in more detail later in this section.

The optical anisotropy, Δn, of a material is defined as the difference between the refractive indices (i.e. $\Delta n = n_{//} - n_{\perp}$) and varies with wavelength. The value of Δn also decreases with increasing temperature due to the order parameter decreasing (de Gennes and Prost, 1995). Above the liquid crystal/isotropic-fluid transition temperature, the refractive index is obviously single valued.

1.4.2 Dielectric Anisotropy

As in the case of optical anisotropy, the dielectric permittivities along the extra-ordinary ($\varepsilon_{//}$) and ordinary ($\varepsilon_{\perp}$) axes of the liquid crystal differ (Raynes, 1991). This dielectric anisotropy (defined as $\Delta\varepsilon=\varepsilon_{//}-\varepsilon_{\perp}$) governs the response of the director to an applied electric field. If the material has positive dielectric anisotropy (i.e. $\varepsilon_{//} > \varepsilon_{\perp}$) the director will tend to align parallel to the applied field and conversely, a negative dielectric anisotropy ($\varepsilon_{//} < \varepsilon_{\perp}$) results in the director lying perpendicular to it. This interaction with an applied external field is used to switch between the light and dark states of a liquid crystal display.

1.4.3 Elastic Constants

When the director profile in a liquid crystal sample is confined between two aligning boundary layers or subjected to an applied field, the molecules will reorientate to minimise the free-energy per unit volume of the sample (Frank, 1958). This condition is the underlying physics of the continuum theory used to determine the director orientation within a given liquid crystal structure. The orientation of the director is dictated by three elastic constants referred to as *splay* (K_{11}), *twist* (K_{22}) and *bend* (K_{33}). These constants are analogous to the spring constant in Hooke's Law with each constant referring to a different spatial distortion of the director, as shown in fig. 1.2. All three elastic constants tend to be around 10^{-11} N in magnitude and generally $K_{33} > K_{11} > K_{22}$.

The resulting elastic free-energy per unit volume of a non-chiral nematic liquid crystal is given by:

$$F = \frac{1}{2}K_{11}\left[\nabla \cdot \mathbf{n}\right]^2 + \frac{1}{2}K_{22}\left[\mathbf{n} \cdot \left(\nabla \times \mathbf{n}\right)\right]^2 + \frac{1}{2}K_{33}\left[\mathbf{n} \times \left(\nabla \times \mathbf{n}\right)\right]^2 \qquad \text{Eq. 1.2}$$

The influence of this relation on the response of a liquid crystal structure is explored further in chapter 3.

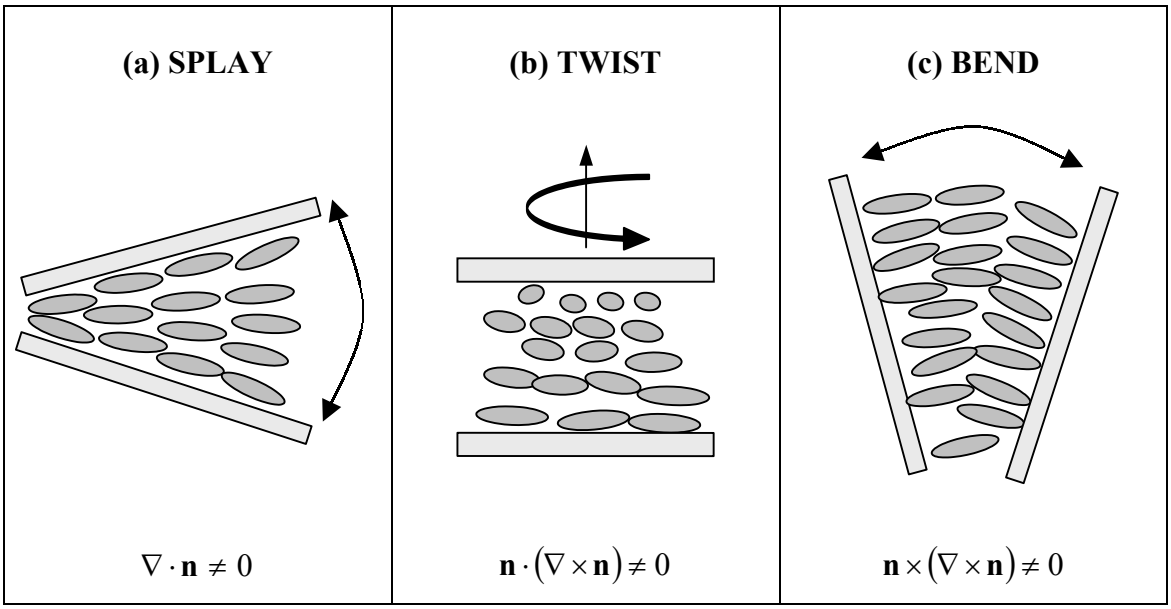

Fig. 1.2 Schematic diagram to show the relative orientation of the director in (a) splay; (b) twist and (c) bend distortions and the spatial derivatives associated with each.

1.5 Liquid Crystal Cells

To allow the dielectric and optical properties of liquid crystals to be exploited in display devices, the orientation of the director within the sample must be controlled by imposing constraints on the director at the upper and lower surfaces of the sample.

For all of the experiments recorded in this thesis, the liquid crystal structures examined are in cells similar in structure to commercially available liquid crystal displays. A liquid crystal layer of a few micrometers in thickness is contained between two glass substrates (of a low refractive index). The inner surfaces of these substrates have an optically thin layer of Indium Tin Oxide (ITO) which acts as a transparent electrode, on top of which are deposited aligning layers, as discussed later in this section.

Fig 1.3 is a schematic of a typical liquid crystal cell. In a liquid crystal display, the structure is obviously much greater in area and pixelated resulting in a far more complex arrangement, but the basic optical layers are the same.

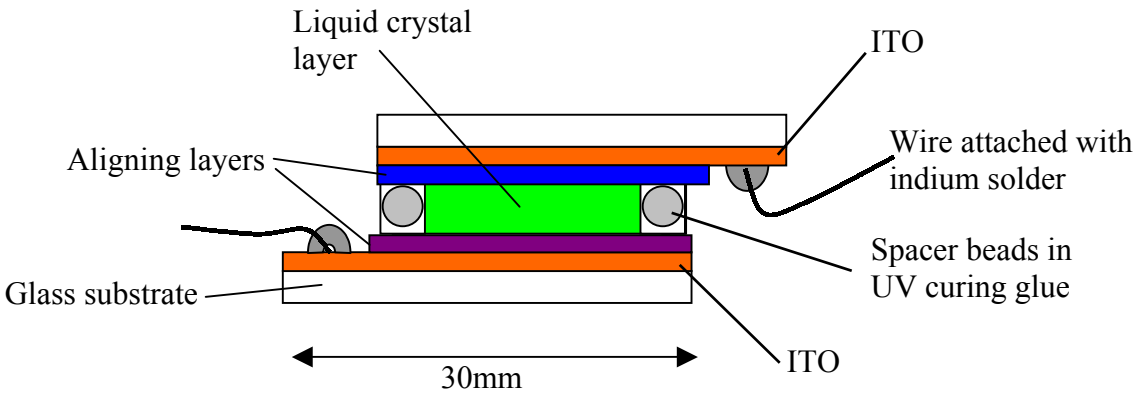

Fig. 1.3 Schematic diagram of a typical liquid crystal cell.

The cell fabrication process is always carried out in a cleanroom environment to minimise the risk of the structure being contaminated by dust. The low-index glass substrates used have a refractive-index of 1.52 (at 632.8nm) and are 1mm thick. The transparent ITO electrodes are pre-deposited on the glass substrates and have a thickness of ≈50nm. Aligning layers to promote a particular alignment direction at the two surfaces are deposited onto the ITO surfaces using one or more of the techniques outlined later in this section.

The cell is assembled using a line of UV glue (with spacer beads of diameter equal to the required cell thickness dispersed in it) along the two parallel short edges of the cell. It is then exposed to a UV lamp for 20 minutes to cure the glue. When set, the cell is filled by capillarity on a heat-stage held at a temperature above the isotropic transition point of the liquid crystal. Once filled, it is cooled to room temperature, and the two open ends are sealed with epoxy resin to prevent any contamination of the liquid crystal material. Finally, wires are attached at the exposed ITO surfaces using indium solder to allow fields to be applied perpendicular to the substrates.

1.6 Alignment Techniques – Homogeneous

Homogeneous alignment is where the liquid crystal director lies parallel to the substrate. In the coordinate system used in this thesis, this corresponds to the director having a tilt angle equal to, or close to 0°, where the tilt angle is measured from the substrate. In certain types of cell it can be preferable to have a pre-tilt at the homogeneous surface as this breaks the symmetry of the surface and can influence the

director profile and switching properties across the whole of the cell. Several techniques for producing homogeneous alignment are available, but only the ones used in this thesis are described here.

1.6.1 Rubbed Polyimide

Rubbed polyimide alignment is commonly used to provide uniform homogeneous alignment over a large surface area, relatively easily and cheaply. The polyimide used is generally a compound composed of long chain molecules which, in the case of a sample cell, is spun down onto the substrate at around 6000rpm, producing a uniform layer of a thickness of ≈ 100nm. The substrate is baked to harden the polymer, and allowed to cool. The polymer surface is then buffed using a rubbing machine composed of a velvet cloth attached to a rotating drum, under which the substrate passes. The alignment of the polymer itself due to the rubbing process, (rather than the microgrooves produced) is believed to be the most influential factor in aligning the liquid crystal layer in contact with the surface (Ito et al, 2000). Intermolecular interactions between the polymer and the liquid crystal molecules induce homogeneous alignment which then propagates into the bulk via elastic interactions.

Rubbed polyimide is commonly used in industry to produce homogeneous alignment in mass-produced liquid crystal displays (in this case the polymer is printed onto the ITO surface). The alignment produced is reasonably robust, and various pretilts can be produced. However, this method can produce ion contamination in the cell, as discussed in chapter 4.

1.6.2 Obliquely Evaporated Silicon Oxide

The evaporation of silicon monoxide at an oblique angle of incidence onto the cell substrate provides an excellent method of inducing homogeneous alignment at the surface. The layer of silicon monoxide deposited (usually around 20nm in thickness) is uneven yet structured to produce homogeneous alignment that is strongly anchored and does not vary over time. The pre-tilt at this surface can be controlled by careful selection of the angle of incidence that the silicon monoxide is evaporated at. Evaporation at a 60° angle from the normal produces a surface alignment parallel to the

substrate and perpendicular to the evaporation direction. If, for example, an 85° angle of incidence is used, the pretilt produced is 30° and along the evaporation direction.

Although this method of alignment has been used for many years to fabricate test-cells with good results, the mechanism by which the liquid crystal aligns on the substrate is still not fully understood (Welford, 1986).

1.7 Alignment Techniques – Homeotropic

Homeotropic alignment is where the director is oriented perpendicular to the substrate. The general method used to induce this alignment is the application of a layer of long chain molecules to the substrate, which orient themselves perpendicular to the surface and then induce the molecules in the neighbouring region to align with them.

1.7.1 Lecithin

Lecithin is a waxy solid which can be dissolved in ether to allow it to be either spun down or dipped onto the glass substrate. The solvent is allowed to evaporate, and any excess lecithin is washed off with ether leaving a monolayer of lecithin behind. It generally provides good but patchy alignment on the surface, but the quality of the alignment degrades over a period of weeks as the lecithin tends to dissolve in the liquid crystal. Any excess not removed after deposition can also migrate across the cell, producing homeotropic alignment on the opposite substrate.

1.7.2 Homeotropic Polyimide

Polymers inducing homeotropic alignment are becoming increasingly common. The polymer is spun-down and baked in the same way as a homogeneous polymer, producing a layer ≈50nm thick. The alignment produced tends to be robust, and different polymers can produce different surface pretilts if required. As in the homogeneous case though, the polymer can cause ions to seep into the liquid crystal. This method of producing homeotropic alignment is however highly suited to commercial applications.

1.7.3 Octadecyltrimethoxysilane ($C_{21}H_{46}O_3Si$)

Octadecyltrimethoxysilane (OTMS) is a molecule composed of an 18 chain carbon molecule attached to a silane group. It is applied to the substrate by mixing a solution of 90% de-ionised water, 9.9% iso-propanol and 0.1% OTMS. The substrate is then dipped into the solution, and the silane group bonds with the surface, producing a monolayer of the material. The substrate is then baked and the excess is removed with Iso-propanol.

This treatment is extremely robust, does not degrade with time and produces alignment with no noticeable pre-tilt and no ion contamination.

1.8 Cell Geometries

The use of various combinations of homogeneous and/or homeotropic alignment layers in conjunction with the many different forms of thermotropic liquid crystals available results in a large range of possible cell structures. Some geometries result in optical properties which can be used in a display, such as the twisted cell described below. Others are used for research purposes, and the director is constrained between the substrates in a way which allows the measurement of physical properties of the liquid crystal material contained within it.

1.8.1 The Twisted Nematic Cell

The twisted nematic geometry (Schadt and Helfrich, 1971) is composed of two orthogonal homogeneously aligning substrates (fig. 1.4 (a)) and polarisers are added either side of the cell oriented parallel to each rubbing direction. When the cell is filled with a nematic liquid crystal and no voltage is present, the director twists through 90° from one surface to the other with the director parallel to the substrate at all points along the *z*-axis.

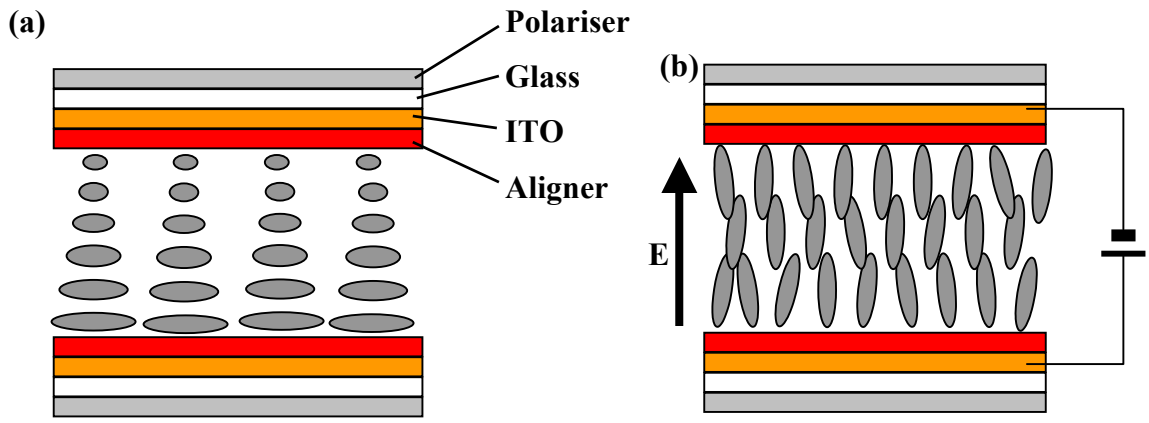

Fig. 1.4 **Schematic diagram of a twisted nematic device with (a) no field applied (the light state) and (b) a voltage applied perpendicular to the substrates (the dark state).**

Provided that the Maugin condition (Maugin, 1911) is satisfied:

$$d\Delta n >> \frac{\lambda}{2} \qquad \text{Eq. 1.3}$$

where d is the cell thickness, Δn is the optical anisotropy and λ is the wavelength of the light, the plane of polarisation of polarised light entering through one surface will be rotated through 90° as it passes through the cell (as described below), and will be transmitted through the top polariser. If the material is of a positive dielectric anisotropy, the application of a few volts across the cell causes the director to align with the field, the twist through the cell is destroyed, with the bulk of the cell becoming homeotropically aligned and the polarisation 'guiding' ceases.

1.8.2 The 'Guiding' Regime

When the pitch of a twisted liquid crystal structure is much greater than the wavelength of the incident light, the director orientation changes little over the distance of several wavelengths (Bahadur, 1990). To model this the twisted nematic structure is considered as composed of a series of parallel slabs of thickness ∂z normal to the helical axis. In each slab the director is uniform but rotated by an amount $\Delta\theta$ relative to the slab below (fig. 1.5).

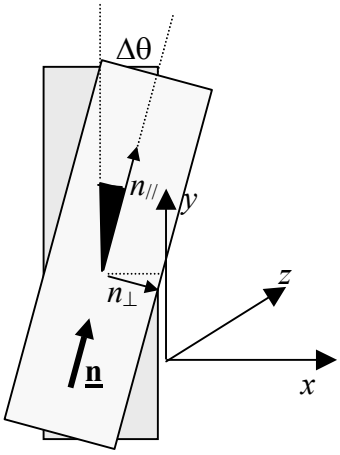

Fig. 1.5 Geometry of the plane of polarisation in a twisted structure.

For incident light polarised along the *y*-axis, it will pass through the first slab undeviated as E_0 is parallel to the director. In the second slice though, the director is at an angle $\Delta\theta$ to the *y*-axis, so the electric field has two components, one parallel to the extra-ordinary axis ($E_{//}$) and one parallel to the ordinary axis ($E_{\perp}$) given by:

$$E_{//} = E_0 \sin(\Delta\theta) \qquad E_{\perp} = E_0 \cos(\Delta\theta) \qquad \text{Eq. 1.4}$$

Due to the optical anisotropy of the liquid crystal (i.e. $n_{//} \neq n_{\perp}$) the two components will travel through the slabs at different speeds, and so will emerge from the slab slightly out of phase.

The *x*- and *y*-components of the emerging light are given by:

$$E_x(\partial z, t) = E_0 \sin(\Delta\theta)\cos(n_{\perp} k_0 \partial z - \omega t) \qquad \text{Eq. 1.5}$$

$$\begin{aligned} E_y(\partial z, t) &= E_0 \cos(\Delta\theta)\cos(n_{//} k_0 \partial z - \omega t) \\ &= E_0 \cos(\Delta\theta)\cos(n_{\perp} k_0 \partial z - \omega t + \Delta n k_0 \partial z) \end{aligned} \qquad \text{Eq. 1.6}$$

The emerging light is therefore elliptically polarised and the phase shift between the two is given by $\Delta n k_0 \partial z$. The angle, α, made by the semi-major axis of elliptically polarised light to the *x*-axis with a phase shift of δ between the two components is given by the standard equation for elliptically polarised light (Born and Wolf, 1999):

$$\alpha = \frac{1}{2}\tan^{-1}\left(\frac{2E_{0x}E_{0y}\cos\delta}{{E_{0x}}^2 - {E_{0y}}^2}\right) \qquad \text{Eq. 1.7}$$

Using eq. 1.4 and 1.5 gives the orientation as:

$$\begin{aligned}\alpha &= \frac{1}{2}\tan^{-1}\left(\frac{2\sin(\Delta\theta)\cos(\Delta\theta)\cos(\Delta nk_0\partial z)}{\left(\sin^2(\Delta\theta) - \cos^2(\Delta\theta)\right)}\right) \\ &= \frac{1}{2}\tan^{-1}\left(\frac{\sin(2\Delta\theta)\cos(\Delta nk_0\partial z)}{-\cos(2\Delta\theta)}\right)\end{aligned} \qquad \text{Eq. 1.8}$$

For an infinitely small thickness ∂z, eq. 1.8 reduces to:

$$\alpha = \Delta\theta \qquad \text{Eq. 1.9}$$

i.e. the rotation of the plane of polarisation is equal to the change in orientation of the director. Therefore, the light emerges from the second slice polarised parallel to the director. As the phase difference $\Delta nk_0\partial z$ is negligible, the emerging light can be considered as being linearly polarised.

This argument can be applied to each of the slabs through the twisted nematic device, and so, after passing through the entire cell, the plane of polarisation is rotated through 90°.

1.9 Hybrid Aligned Nematic Cells

As the name suggests, a hybrid aligned nematic cell contains two types of alignment. The ITO layer of one substrate is coated with a layer of homeotropically aligning layer (θ = 90°), and the other substrate is treated with a homogeneous aligner (θ = 0°). When the cell is assembled and filled with a non-chiral nematic liquid crystal, the director tilts through 90° from one surface to the other, as shown in fig. 1.6 (a).

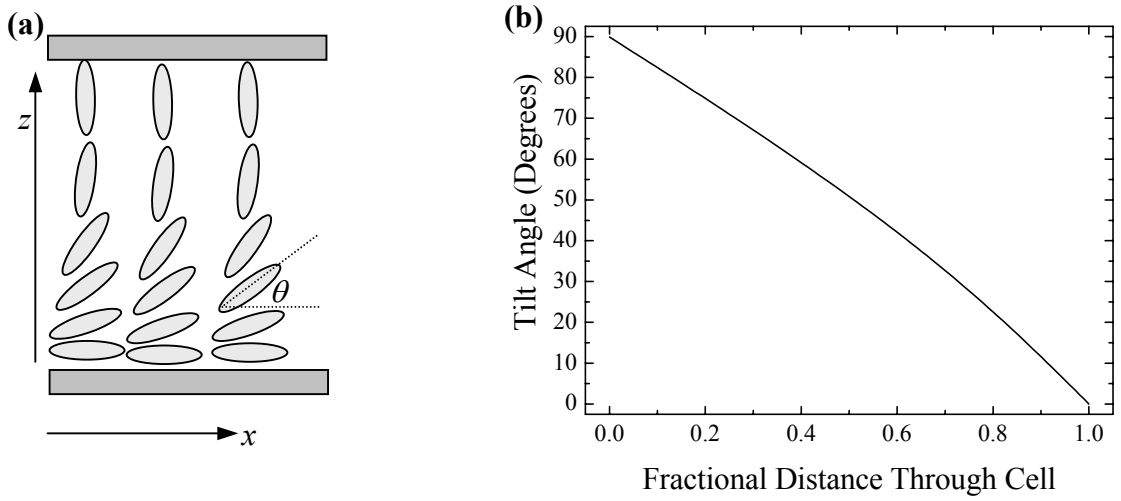

Fig. 1.6 (a) Schematic diagram of a HAN cell showing the definition of the tilt angle, θ and (b) Illustration of a typical tilt profile through a HAN cell at 0V.

As there is no twist present in the system, the structure can be considered as one-dimensional, with $\frac{\partial}{\partial x} = \frac{\partial}{\partial y} = 0$ and the director **n** can be denoted by:

$$\mathbf{n}_x = \cos\theta\,\hat{\mathbf{x}} \qquad \mathbf{n}_y = 0 \qquad \mathbf{n}_z = \sin\theta\,\hat{\mathbf{z}} \qquad \text{Eq. 1.10}$$

With no voltage applied, the variation of tilt with distance through the cell (referred to as the director profile) is close to, but generally not exactly, linear (fig. 1.6 (b)). This deviation is the result of the difference between the splay and bend coefficients (ignoring flexoelectric effects which are discussed later). From eq. 1.10 and fig.1.2 it can be seen that at the homeotropic surface, the distortion of the director is pure bend, and at the homogeneous surface, pure splay. The remainder of the cell is a combination of splay and bend distortion, but as the bend elastic coefficient is generally higher than the splay coefficient, the director is biased towards the homeotropic surface.

1.9.1 Dielectric response

Due to the elastic distortion imposed on the director by the constraints at the upper and lower substrates, a HAN cell has a near-thresholdless response to the application of an electric field perpendicular to the substrates. The application of even a

small voltage (≈0.1V) across a 5μm HAN cell will result in the director responding accordingly to minimise the sum of the elastic and dielectric free-energy. In the case of a liquid crystal material with positive dielectric anisotropy, the director will tend towards vertical alignment, and as the voltage is increased the proportion of the cell homeotropically aligned will increase, with the transition from homeotropic to homogeneous alignment occurring over an increasingly reduced distance through the cell, as shown in fig. 1.7. (This assumes that the anchoring at the homogeneous surface is very strong.) Conversely, if a material of negative dielectric anisotropy is used, the director will tend towards the homogeneous surface in a similar manner.

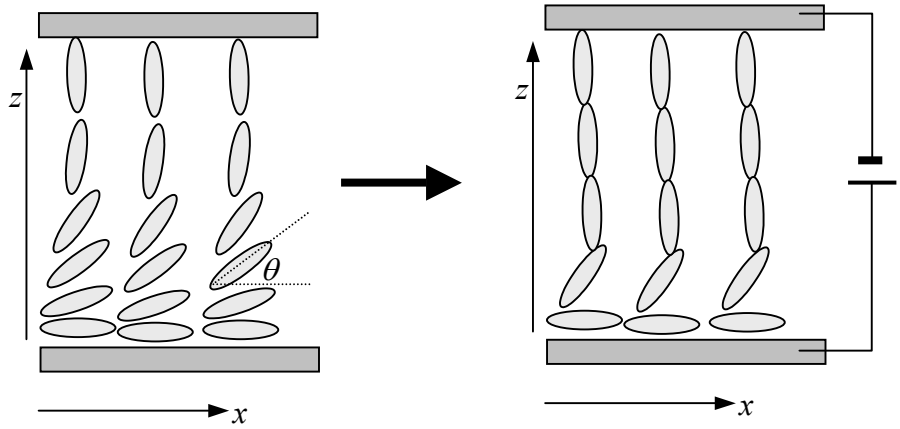

Fig. 1.7 Schematic diagram showing the response of the director in a HAN cell to the application of a high voltage.

This thresholdless response makes the HAN geometry ideal for investigating the physical properties of liquid crystalline materials such as characterising the elastic and dielectric constants of the material and measuring the surface anchoring energy at the liquid crystal/substrate interface.

1.9.2 Optical Properties

For a 1D HAN structure at 0V there is no twist and so polarisation-guiding, as discussed previously in the case of a twisted nematic device does not occur. If the cell is placed between crossed polarisers with the homogeneous alignment at an angle to the transmission axes of both polarisers, light will be transmitted though due to the birefringence of the liquid crystal.

If the cell is of thickness *d*, at 0V the director tilts through 90° from 0° (homogeneous alignment) on the lower surface to 90° (homeotropic alignment) on the upper (fig. 1.8 (a)).

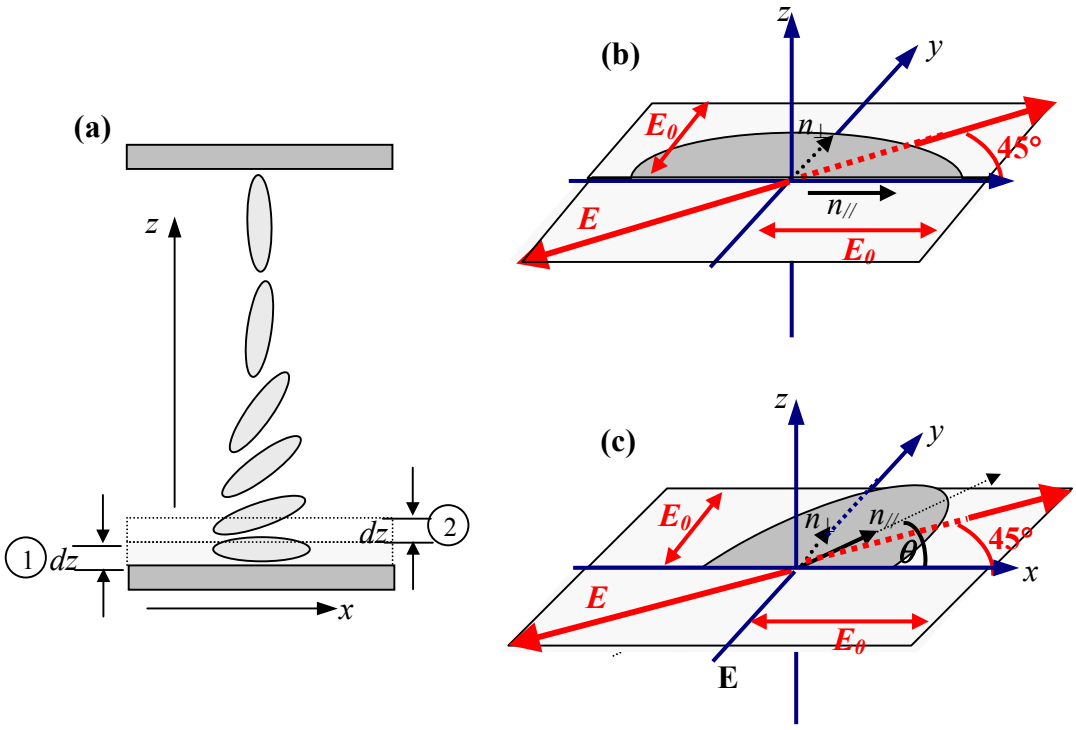

Fig. 1.8 **(a) Schematic diagram of a 1D HAN cell; (b) the relative orientations of $n_{//}$ and $n_\perp$ for the liquid crystal layer adjacent to the substrate and (c) the relative orientations of $n_{//}$ and $n_\perp$ when the director is at an angle θ to the *x*-axis.**

When the cell is placed between crossed polarisers (lying in the *x*-*y* plane) with the extra-ordinary axis (labelled *x* in fig. 1.8 (a)) at a 45° angle to the transmission axis of the lower polariser, the components along the *x*- and *y*-axes will be of an equal amplitude, and can be defined as:

$$E_x = E_0 \cos(\omega t) \qquad E_y = E_0 \cos(\omega t) \qquad \text{Eq. 1.11}$$

This light now passes through a layer of liquid crystal of thickness *dz* which is adjacent to the liquid crystal substrate with the extra-ordinary axis of the director lying parallel to the *x*-axis (fig. 1.8 (b)). Due to birefringence ($n_{//} \neq n_\perp$) the *x*- and *y*-

components of the light pass through the layer at different speeds and the emerging light is characterised as:

$$E_x(z,t) = E_0 \cos(n_\perp k_0 \delta z - \omega t) \quad \text{Eq. 1.12}$$

$$E_y(z,t) = E_0 \cos(n_{//} k_0 \delta z - \omega t) \quad \text{Eq. 1.13}$$

Hence there now exists a phase difference between the two components of the light given by $\Delta n k_0 \delta z$.

This light now passes through the second layer of liquid crystal indicated in fig. 1.8 (a), again of thickness *dz*. In this layer, the director is now tilted at an angle θ to the *x*-axis. The refractive indices are related to the optical permittivities of the material by the relations

$$n_{//} = \sqrt{\varepsilon_{//}} \qquad n_\perp = \sqrt{\varepsilon_\perp} \quad \text{Eq. 1.14}$$

For the *y*-component of the *E*-field, as there is no twist in the structure, the effective index "seen" by the light as it passes through the layer is simply:

$$n_y = n_\perp = \sqrt{\varepsilon_\perp} \quad \text{Eq. 1.15}$$

For the *x*-component of the *E*-field, the effective refractive index is more complex as the variation of the tilt angle through the cell must be considered. For a tilt angle of θ measured from the *x*-axis, the components of the displacement field **D** parallel and perpendicular to the director (fig. 1.9) are given by:

$$D_{//} = \varepsilon_{//} E_{//} \quad \text{Eq. 1.16}$$

$$D_\perp = \varepsilon_\perp E_\perp \quad \text{Eq. 1.17}$$

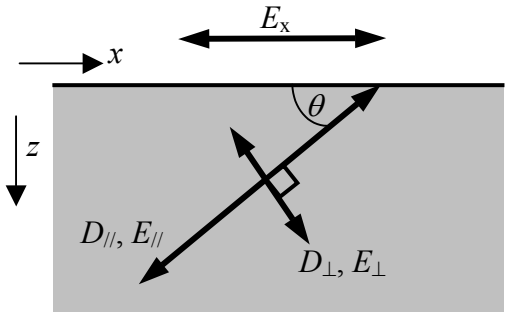

Fig. 1.9 **Diagram showing the relative directions of various components of the D and E fields in a uniaxial medium with the director at an angle θ to the *x*-axis.**

From Maxwell's boundary conditions, the component of **D** normal to the interface is conserved, and so $D_z = 0$. Therefore:

$$D_z = D_{\perp}\cos\theta - D_{//}\sin\theta = 0 \qquad \text{Eq. 1.18}$$

and as a result:

$$D_{\perp} = D_{//}\frac{\sin\theta}{\cos\theta} \qquad \text{Eq. 1.19}$$

Hence:

$$\varepsilon_{\perp}E_{\perp} = \varepsilon_{//}E_{//}\frac{\sin\theta}{\cos\theta} \qquad \text{Eq. 1.20}$$

The *x*-component of **D** is then given by:

$$\begin{aligned} D_x &= D_{//}\cos\theta + D_{\perp}\sin\theta \\ &= \varepsilon_{//}E_{//}\left[\cos\theta + \frac{\sin^2\theta}{\cos\theta}\right] \\ &= \frac{\varepsilon_{//}E_{//}}{\cos\theta} \end{aligned} \qquad \text{Eq. 1.21}$$

The boundary conditions require that the tangential component of **E** is conserved, and so E_x is constant through the medium, and is given by:

$$\begin{aligned} E_x &= E_{//}\cos\theta + E_{\perp}\sin\theta \\ &= E_{//}\cos\theta + E_{//}\frac{\varepsilon_{//}}{\varepsilon_{\perp}}\frac{\sin^2\theta}{\cos\theta} \\ &= \frac{E_{//}}{\cos\theta}\left[\cos^2\theta + \frac{\varepsilon_{//}}{\varepsilon_{\perp}}\sin^2\theta\right] \end{aligned} \qquad \text{Eq. 1.22}$$

The permittivity for the *x*-component of the light is therefore:

$$\varepsilon_x = \frac{D_x}{E_x} = \frac{\varepsilon_{\perp}\varepsilon_{//}}{\varepsilon_{\perp}\cos^2\theta + \varepsilon_{//}\sin^2\theta} \qquad \text{Eq. 1.23}$$

and so from eq. 1.14 the effective refractive index becomes:

$$n_x = \frac{n_{\perp}n_{//}}{\sqrt{n_{\perp}^2\cos^2\theta + n_{//}^2\sin^2\theta}} \qquad \text{Eq. 1.24}$$

As before, the phase difference produced due to passing through this second layer is:

$$\begin{aligned} d\varphi &= \Delta n\, k_0 dz \\ &= \left(n_x - n_y\right)k_0 dz \\ &= \left(\frac{n_{//}}{\sqrt{n_{\perp}^2\cos^2\theta + n_{//}^2\sin^2\theta}} - 1\right)n_{\perp}k_0 dz \end{aligned} \qquad \text{Eq. 1.25}$$

This retardation continues as the light passes through each successive layer of the cell, and the total retardation $\Delta\varphi$ produced due to travelling through a distance *d* can be calculated from:

$$\int_0^{\Delta\varphi} d\varphi = n_{\perp}\, k_0 \int_0^{d}\left(\frac{n_{//}}{\sqrt{n_{\perp}^2\cos^2\theta + n_{//}^2\sin^2\theta}} - 1\right)dz \qquad \text{Eq. 1.26}$$

For a HAN cell at 0V, the tilt profile can be approximated as being linear, varying from 0 to $\frac{\pi}{2}$ over a distance *d*. Therefore:

$$\frac{d\theta}{dz} = \frac{\pi}{2} \cdot \frac{1}{d}$$

$$\therefore \quad \theta = \frac{\pi z}{2d} \qquad \text{Eq. 1.27}$$

Hence

$$\Delta\varphi = \frac{2\pi n_{\perp}}{\lambda_0} \int_0^d \left(n_{//} \left(n_{\perp}^2 \cos^2\left(\frac{\pi z}{2d}\right) + n_{//}^2 \sin^2\left(\frac{\pi z}{2d}\right)\right)^{-\frac{1}{2}} - 1 \right) dz \qquad \text{Eq. 1.28}$$

where λ_0 is the wavelength of the incident light. This expression can be integrated numerically, and if the phase retardation is equal to $(2m\text{-}1)\pi$ where *m* is an integer, the result is that the plane of polarisation of the light entering at the lower surface is rotated through 90° and linearly polarised light is transmitted through the top polariser.

This derivation only applies to a HAN cell at 0V viewed normal to the substrate. When a voltage is applied, the director starts to align with the field and eq. 1.27 breaks down. At a very high voltage, most of the cell is homeotropically aligned and so the incident light effectively only encounters one refractive index ($n_{\perp}$). This apparent lack of birefringence results in the plane of polarisation not being rotated, and so the cell appears dark under crossed polarisers.

1.10 The Zenithal Bistable Device

A bistable liquid crystal device is one which has two stable director configurations at 0V. These two alignments, one usually allowing the transmission of light through crossed polarisers, and the other not, can be switched between by the application of a voltage pulse and they will remain in the new state until a second pulse is applied, causing it to switch to the other state.

The Zenithal Bistable Device (ZBD) is one such device which is produced commercially (Bryan-Brown et al, 1997). The advantage of such a display is that, unlike

in a standard twisted nematic liquid crystal display where a voltage must be held across the pixels to maintain an image, the bistable device only requires the application of a voltage to switch between the two states. The geometry of the cell holds the pixels in the light or dark state required until the display is updated with the application of a voltage pulse. This therefore drastically decreases the power consumption of such a device making them far more efficient.

The bistability of the ZBD is achieved by using a grating of a suitable amplitude and pitch as one aligning surface. This grating is treated with a homeotropic aligning layer to allow two different surface pre-tilts to be possible, as shown in fig. 1.10. The opposite surface of the cell is treated with an aligning layer which produces permanent alignment in the required orientation.

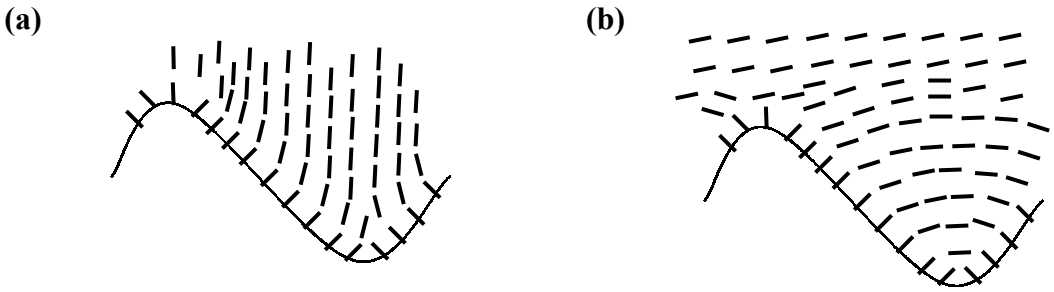

Fig. 1.10 Diagram showing (a) the high-tilt and (b) the low-tilt states in the region close to the bistable grating surface used in ZBD cells.

In the original ZBD structure, the opposite substrate was coated with a homeotropic aligning layer. The two stable states possible were the Vertical Aligned Nematic (VAN) (dark state) and the Hybrid Aligned Nematic (HAN) (light state), as shown in fig. 1.11 (a). (The mechanism the induces switching between these two states is discussed in detail in chapter 3.) This structure was found to be very insensitive to variations in cell thickness, but had a poor viewing angle range.

The second ZBD device produced, which is now being commercially developed, uses homogeneous alignment at the upper surface, with the bistable grating surface the same as before (Jones et al, 2000). The two stable states in this case are a Twisted Nematic (TN) (dark state) and the HAN (light state) (this time with the homogeneous alignment at the *upper* surface, and parallel to the grating grooves). This geometry is illustrated in fig. 1.11 (b).

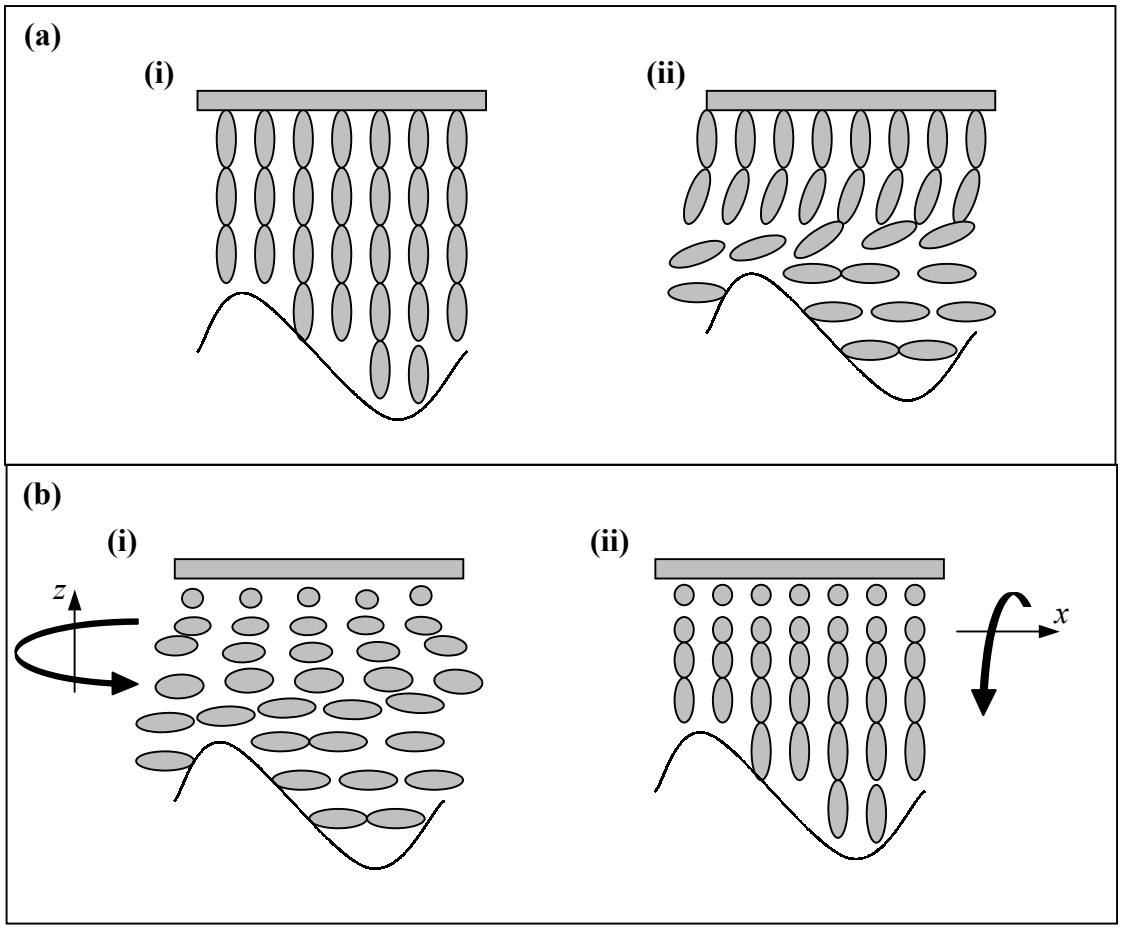

Fig. 1.11 Diagram showing (a) the original ZBD geometry with (i) the VAN and (ii) the HAN state, and (b) the new ZBD geometry with (i) the TN state and (ii) the HAN state.

Apart from the low power consumption associated with the ZBD display, it is also very rugged and has a good contrast ratio. This makes it an excellent device for use in many applications, from mobile phones to digital watches. This commercial application of the HAN geometry in conjunction with the information gained from studying the thresholdless response of a standard 1D HAN cell to the application of an applied voltage is the motivation behind studying it in detail in this thesis.

1.11 Thesis Outline

Chapter 2 gives an introduction to optical waveguides, and an overview of various waveguide techniques used over the past decade to study the director profile in liquid crystal cells is given. A detailed account of the fully-leaky guided-mode technique used to study the static director profile in liquid crystal cells is given, and the particular advantages of this method are discussed. Finally, the convergent beam technique, used to investigate liquid crystal director dynamics, is described in detail.

The remainder of the thesis can be conveniently divided into two sections. Chapters 3,4 and 5 discuss the properties of static liquid crystal profiles, where a voltage a voltage is maintained across a test cell. The dynamics of the liquid crystal director as the cell responds to changes in applied voltages is then considered in chapters 6,7 and 8.

Chapter 3 discusses the influence of flexoelectricity in liquid crystal structures – a phenomenon occurring in liquid crystals that is analogous to the piezoelectric effect in solids. A continuum theory is used to derive an expression for the static equilibrium structure of a hybrid aligned nematic cell at an applied voltage when the flexoelectric contribution to the free-energy is considered. This is then used as the basis for developing a program to model the director profile in a HAN cell at applied fields. The effect of varying the flexoelectric coefficients on the director profile and the internal fields produced within the cell are then modelled.

Chapter 4 describes a fully-leaky guided mode study performed to measure the director profile in HAN cells. The sum of the splay and bend flexoelectric coefficients of E7 is determined by applying forward and reverse bias DC voltages to the cell and measuring the director profile in each case. This study found that the resulting profiles were dependent not only on the flexoelectric coefficients, but also the presence of surface polarisation at the homeotropic aligning layer, and the origin of this is discussed.

Chapter 5 is a further experimental chapter investigating the static director profile in a HAN cell when high frequency AC voltages are applied. In this case a fully-leaky waveguide structure is used in conjunction with a polarimeter to measure the Stokes' parameters of light transmitted through the structure as a function of angle of

incidence. From this information, the director profiles were determined, and the anchoring energy at the homogeneous surface was calculated.

The theory behind the dynamical response of the director in a HAN cell to applied fields is introduced in chapter 6. Initially, the fluid mechanics associated with an isotropic fluid is considered, and the Leslie-Eriksen-Parodi theory of nematodynamics for anisotropic materials is then introduced, and the added degrees of complexity due to the use of five viscosity coefficients are highlighted. The nematodynamics equations specifically relating to a HAN geometry are derived, and their implementation in a modelling program is discussed. This program is then used to model the director profile on the millisecond time-scale when AC and DC voltages are applied to, and removed from, a HAN cell.

Chapters 7 and 8 contain details of convergent beam measurements performed to measure both the switch-on and switch-off dynamics of a ZLI-2293 filled HAN cell. These measurements were made with 0.3ms resolution, allowing a detailed study to be made of the form taken by the director during the switching process. In both cases, a phenomenon known as backflow is observed, where the director in one region of the cell initially rotates in the opposite direction to the rest of the cell. These measured profiles show good agreement with modelled profiles produced by the program discussed in chapter 6, and from these comparisons, the viscosity coefficients of ZLI-2293 are obtained. The influence of each of the viscosity coefficients on the switching is modelled, and comparisons are drawn between the switch-on and switch-off cell dynamics.

Chapter 2

Optical Waveguide Characterisation Techniques

2.1 Introduction

To enable progress to be made in the development of liquid crystal displays, it is vital to have a good understanding of the behaviour of the liquid crystal during the operation of the device. For this reason, techniques to probe and characterise the director structure in commercial style liquid crystal cells are required.

Optical methods such as polarising microscopy (Clark *et. al.*, 1990) allow information integrated across the cell to be obtained, but little information about the detailed director structure is available. With alternative techniques such as neutron scattering or X-ray diffraction measurements (Taylor, 1996), detailed information about layering in complex, periodic structures (e.g. the smectic phases) can be discovered, but the method is impractical for the study of commercial type devices, and does not yield the important optical director information.

The study of a cell structure using optical waveguide techniques solves many of these problems. The use of waveguides to transfer optical data in the communications industry is well established as a fast, efficient method of confining an electro-magnetic wave within a medium. The distribution of the electromagnetic field within the structure is well understood, and the influence of the optical properties of the medium can be accurately modelled. It is this property that makes waveguiding an ideal tool for probing the intricate structure of commercial style liquid crystal cells, and allows a wealth of information about the director structure in both static and dynamic situations to be obtained.

In this chapter, a brief introduction to the theory of waveguiding is given. Particular consideration is given to the distribution of electromagnetic fields within a waveguiding structure. An overview of optical waveguide techniques is then provided, followed by a detailed account of the fully-leaky guided-mode technique, used to study various properties of hybrid aligned nematic liquid crystal cells. Finally, the convergent beam technique, used to study the dynamic properties of HAN cells, is discussed.

2.2 Optical waveguide modes

The confinement of electromagnetic radiation within a waveguide is governed by Snell's law. The waveguiding condition can be illustrated by considering a tri-layer planar structure composed of three media, each with a different refractive index (Fig. 2.1). The lower layer is the substrate and has a refractive index n_s, the core media, referred to as the waveguide, has a refractive index n_f and the upper (cladding) layer has a refractive index of n_c. For true waveguiding to occur in the structure, it is required that $n_f > n_c$ and $n_f > n_s$. For the purpose of the following discussion, it is also assumed that $n_f > n_s > n_c$.

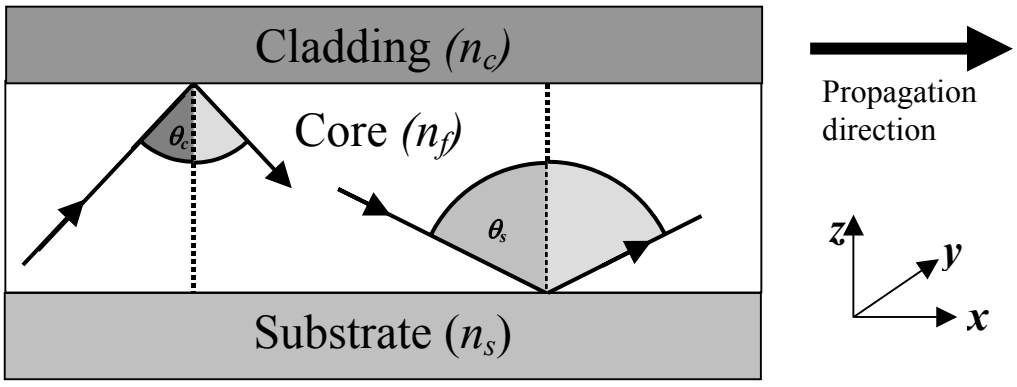

Fig. 2.1 **Schematic diagram of a typical waveguide structure, showing the critical angles for the cladding/core interface and the substrate/core interface.**

An electromagnetic wave within the core will be fully guided (i.e. propagate solely within the middle layer, being evanescent in the other two media) when the

internal angle of incidence θ is greater than both the critical angle at the waveguide/cladding interface (θ_c) and the critical angle at the waveguide/substrate interface (θ_s). From Snell's law (the conservation of longitudinal momentum), these critical angles are given by:

$$\theta_c = \sin^{-1}\left(\frac{n_c}{n_f}\right) \qquad \text{Eq. 2.1} \qquad\qquad \theta_s = \sin^{-1}\left(\frac{n_s}{n_f}\right) \qquad \text{Eq. 2.2}$$

For the situation where $n_s > n_c$, it follows that $\theta_s > \theta_c$, and so three different optical situations are possible.

2.2.1 Fully-guided mode

In the angle range $\theta_s < \theta < \pi/2$, light is fully guided through the waveguide. Evanescent decaying fields occur in the cladding and substrate layers, but in the absence of any imaginary part of the refractive index, the radiation has no real component of momentum, normal to the interfaces, in the outer layers.

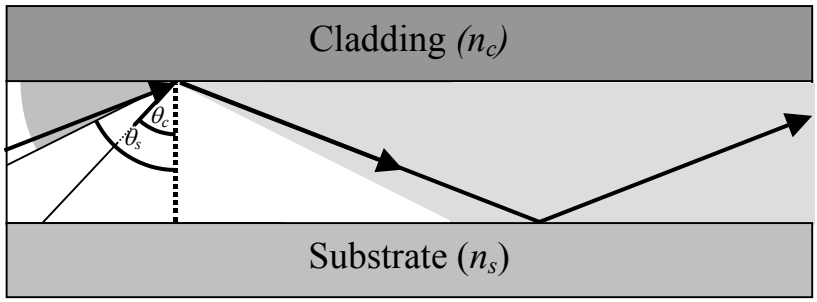

Fig. 2.2 Illustrative ray diagram for a fully-guided waveguide mode

2.2.2 Half-leaky guided mode

In the angle range $\theta_c < \theta < \theta_s$, total reflection of the incident electromagnetic radiation only occurs at the cladding/core interface. Light incident on the other interface is able to escape from the structure, and only partial reflection occurs.

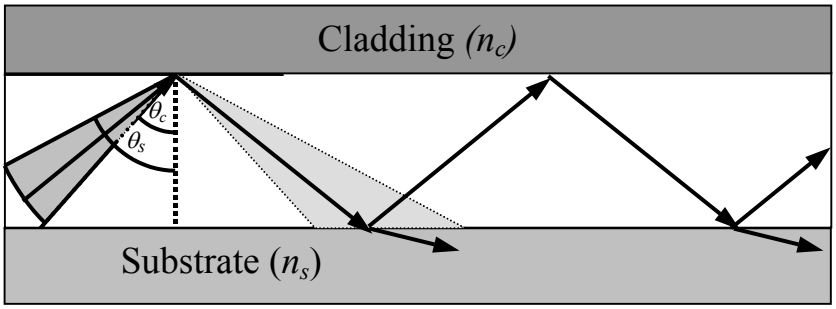

Fig. 2.3 Illustrative ray diagram for the half-leaky guided mode

2.2.3 Fully-leaky guided mode

In the region $\theta < \theta_c$, radiation can leak from both interfaces, producing a very weak propagating wave in the core region.

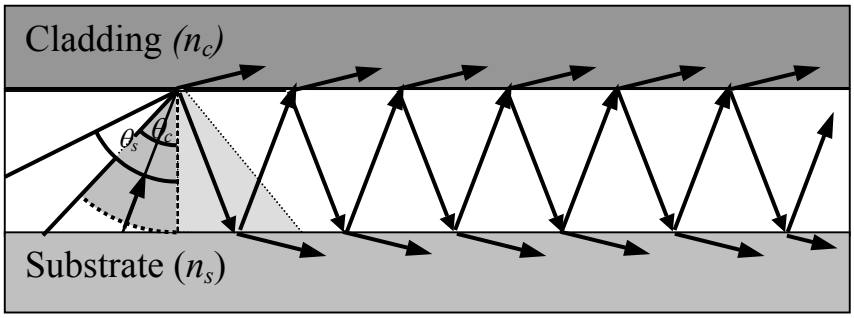

Fig. 2.4 Illustrative ray diagram for the fully-leaky waveguide mode

2.3 Discretisation of modes

The ray pictures described previously give a very basic description of the three types of guided modes possible in a tri-layer optical structure. In fact, angularly dependent phase-shifts occur at the interfaces, and a guided mode is only supported if

the ray constructively interferes with itself along the *z*-axis. This leads to an expression for the *z*-component of the momentum for constructive interference:

$$k_z = \frac{\Phi_{fs}(\theta) + \Phi_{fc}(\theta) + m\pi}{d} \qquad \text{Eq. 2.3}$$

where $\Phi_{fs}(\theta)$ and $\Phi_{fc}(\theta)$ are the angle-dependent phase shifts at the core/substrate and core/cladding interfaces respectively, d is the core thickness and m is an integer. This *z*-component of the momentum is also related to the wavevector of the radiation in free space, k_0, by:

$$k_z = k_0 n_f \cos\theta \qquad \text{Eq. 2.4}$$

As a result, for light of wavelength λ and hence wavevector k_0, only a discrete set of internal angles, θ, exist where fully-guided modes are able to propagate. For this situation, the allowed in-plane wavevectors are then given by:

$$k_x = \left[{k_0}^2 {n_f}^2 - \left(\frac{\Phi_{fs}(\theta) + \Phi_{fc}(\theta) + m\pi}{d} \right)^2 \right]^{1/2} \qquad \text{Eq. 2.5}$$

This expression can be generalised further by using Fresnel's equations for $\Phi_{fs}(\theta)$ and $\Phi_{fc}(\theta)$ (Born and Wolf, 1999), as shown in the next section, and as a result the phase-shifts are polarisation sensitive. There are therefore two different solutions for transverse magnetic (TM) and transverse electric (TE) radiation.

2.4 Field distribution within the structure

The variation of field intensity along the *z*-axis of the structure can be calculated to give an indication of how different modes are sensitive to the optical properties of different spatial regions (Elston and Sambles, 1998). The field distribution expression is derived by first considering Maxwell's equations for an isotropic non-magnetic lossless planar dielectric slab.

$$\nabla \wedge \mathbf{E}(\mathbf{r},t) = -\mu_0 \frac{\partial \mathbf{H}(\mathbf{r},t)}{\partial t} \quad \text{Eq. 2.6}$$

$$\nabla \wedge \mathbf{H}(\mathbf{r},t) = \varepsilon_0 n^2 \frac{\partial \mathbf{E}(\mathbf{r},t)}{\partial t} \quad \text{Eq. 2.7}$$

In these expressions, μ_0 is the magnetic permeability of free space, ε_0 is the electric permittivity of free space, and n is the refractive index of the dielectric at the frequency of the radiation. For a plane wave travelling along the z-axis with wavevector k_z the electromagnetic fields are given by:

$$\mathbf{E} = \mathbf{E}(x,y)\exp[i(\omega t - k_z z)] \quad \text{Eq. 2.8}$$

$$\mathbf{H} = \mathbf{H}(x,y)\exp[i(\omega t - k_z z)] \quad \text{Eq. 2.9}$$

For a 2D waveguide in the x-z plane, with no variation along the y-axis, two independent solutions are produced by using Maxwell's equations and the conditions $E_x = H_x = 0$, $\partial/\partial t = \mathbf{i}\omega$, $\partial/\partial x = -\mathbf{i}k_z$ and $\partial/\partial y = 0$. One equation is for TE polarised light:

$$\frac{\partial^2 E_y}{\partial z^2} + \left[k_0{}^2 n^2 - k_z{}^2\right] E_y = 0 \quad \text{Eq. 2.10}$$

and the other for TM polarised light:

$$\frac{\partial^2 H_y}{\partial z^2} + \left[k_0{}^2 n^2 - k_z{}^2\right] H_y = 0 \quad \text{Eq. 2.11}$$

These two equations are used in conjunction with boundary conditions to determine the field profile through the structure. For TE polarised light, E_y and $\partial E_y / \partial z$ are continuous across the interfaces, as are H_y and $\partial H_y / \partial z$ for TM polarised radiation. The phase-shifts produced by these conditions differ for the two polarisations and are given by:

Transverse Electric	Transverse Magnetic
$\Phi_{fs} = \tan^{-1}\left(\frac{\gamma_s}{k_z}\right)$ Eq. 2.12	$\Phi_{fs} = \tan^{-1}\left[\left(\frac{n_f}{n_s}\right)^2 \frac{\gamma_s}{k_z}\right]$ Eq. 2.14
$\Phi_{fc} = \tan^{-1}\left(\frac{\gamma_c}{k_z}\right)$ Eq. 2.13	$\Phi_{fc} = \tan^{-1}\left[\left(\frac{n_f}{n_c}\right)^2 \frac{\gamma_c}{k_z}\right]$ Eq. 2.15

The exponential decay constant for evanescent fields in the substrate is given by:

$$\gamma_s = \left[k_x^{\,2} - k_0^{\,2} n_s^{\,2}\right]^{1/2} \qquad \text{Eq. 2.16}$$

and for the cladding:

$$\gamma_c = \left[k_x^{\,2} - k_0^{\,2} n_c^{\,2}\right]^{1/2} \qquad \text{Eq. 2.17}$$

For angles of incidence close to grazing, $\sin\theta \rightarrow 1$ and so k_x and hence γ_s and γ_c are large. Combining this with the assumption that $n_f >> n_s$ and n_c, the phase-shifts at the interfaces approach $\pi/2$ and hence the z-component of the wavevector reduces to:

$$k_z = (m+1)\frac{\pi}{d} \qquad \text{Eq. 2.18}$$

i.e. standing waves across the waveguide with zero amplitude at the interfaces. Examples of the TE-field profiles produced for the situations where m = 0, 1 and 2 are shown in fig. 2.5. The diagrams show how the intensity of the field varies across the waveguide, with the m = 0 case being particularly sensitive to the refractive index at the central region of the core, whereas the m = 1 mode is more sensitive towards the edges.

From equations 2.16 and 2.17, as k_x decreases, γ_s and γ_c become imaginary and the field is able to 'leak' into the substrate, with k_z existing over a continuous spectrum of values, and the waveguide becomes first half-leaky, and then fully-leaky.

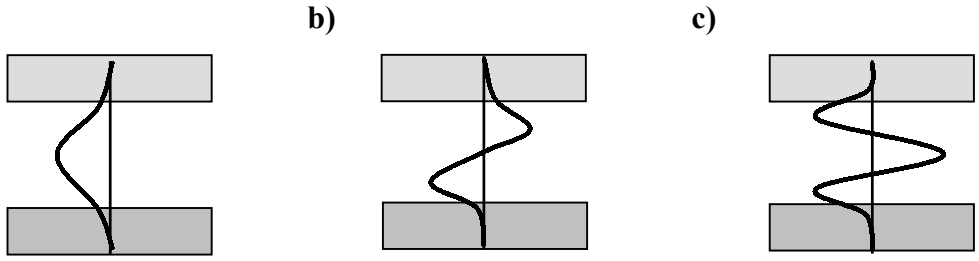

Fig. 2.5 **The field profiles across a fully-guiding waveguide structure for the first three modes for TE incident radiation, corresponding to (a) m = 0; (b) m = 1 and (c) m = 2, as calculated from eq. 2.18**

2.5 Coupling of incident EM radiation into a waveguide

To enable waveguide techniques to be used to explore the complex optical properties of a liquid crystal layer, light must first be coupled into the waveguide. For true guiding, the very nature of the guided mode within the structure means that it is not possible to access the waveguide modes by directly illuminating the material from outside the structure, and so a coupling procedure is required to allow light of suitable momentum to enter the structure. Methods used in the optical communications industry include end-coupling and internal fluorescence, but these are not suitable for optical characterisation studies due to their intrusive effect on the material under study.

The technique most suitable for probing a liquid crystal cell is the use of an external prism index-matched (e.g. by using a layer of matching fluid) to the cladding layer (Harris et. al., 1970). As discussed later in this chapter, it can also be advantageous to couple transmitted light out of the structure by index-matching a second prism to the lower substrate.

From Snell's law, it can be seen that the effect of the prism is to increase the in-plane momentum vector k_x by a factor n_p, where n_p is the refractive index of the prism and θ_p is the angle of incidence inside the prism.

$$k_x = n_p k_0 \sin\theta_p \qquad \text{Eq. 2.19}$$

The magnitude of the refractive index of the glass plates and hence the coupling prism(s) used in relation to those of the liquid crystal determine whether the guided mode is fully guided, half-leaky or fully-leaky. A brief description of these techniques is given later in this chapter.

2.6 Liquid crystal waveguiding structures

When the core material of a waveguide structure is an aligned liquid crystal, the field profile description outlined above takes on an added degree of complexity. All of the calculations have assumed that the waveguide material is isotropic, lossless and uniform. This is not the case for a uniaxial nematic liquid crystal. The real and imaginary parts of the ordinary and extra-ordinary refractive indices in most compounds differ. Therefore the optical properties of different spatial regions across the waveguide will vary, depending on the orientation of the liquid crystal director with respect to the plane of the incident light. Furthermore, the fields will also differ for TE and TM radiation. The transmission, reflection and field-profile properties of such structures can be modelled by using a rigorous multi-layer optics modelling procedure, such as a 4X4 Berreman matrix (the details of which are found in Azzam and Bashara (1996) or Barnes (1986), see also Ko and Sambles (1988)). Fig. 2.6 shows examples of the E_y component of the electric field across a typical liquid crystal cell composed of low-index substrates (n = 1.52), 100nm ITO layers on each surface, and a 3μm hybrid aligned nematic liquid crystal layer. The cell is orientated at a 60° azimuth, and the incident light is *p*-polarised. The components of both *p*- and *s*-polarised light within the structure have been modelled for a selection of angles of incidence. Note that for this case, because the two indices of the anisotropic liquid crystal are greater than that of the substrates, the structure is always fully-leaky. Also, as the incident light is purely *p*-polarised, there are no oscillations in the field strength of the *s*-polarised component in the incident glass layer.

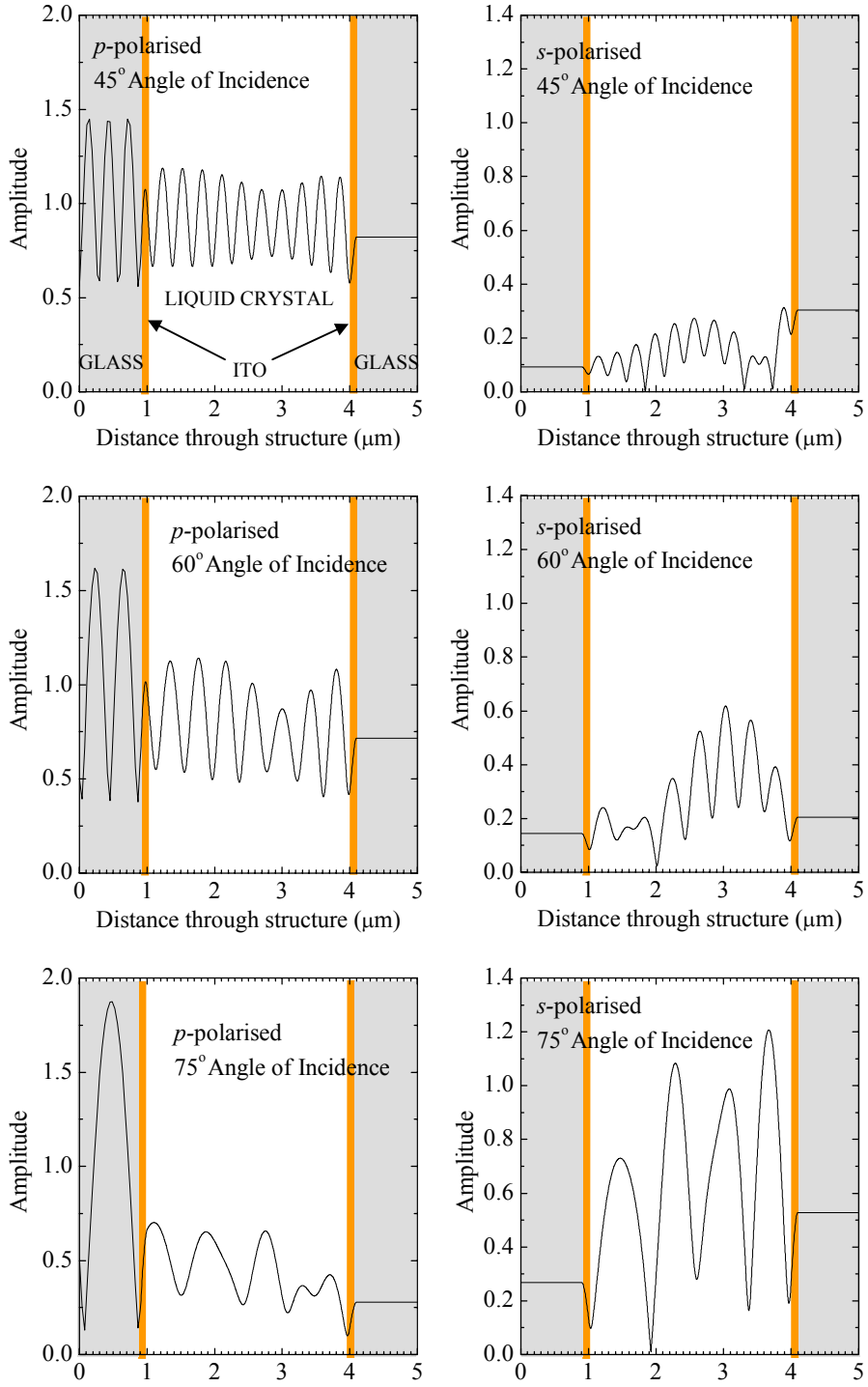

Fig. 2.6 **Modelled field profiles across a glass/ITO/HAN/ITO/Glass structure for *p*-polarised incident light at 45°, 60° and 75° angles of incidence. The amplitude of E_y for the *p*- (polarisation conserving) and *s*- (polarisation converting) components are shown.**

2.7 Optical Guided Mode Techniques – Static Measurements

Optical guided modes were first used to examine the director structure of a liquid crystal cell in detail by Welford and Sambles (1987). A fully-guided mode method was used where the liquid crystal layer was aligned between two metal-coated glass substrates, and high-index prisms were used to couple light in and out of the structure. This technique allowed a detailed study of the director structure in both the bulk and surface regions of the liquid crystal cell (Welford. *et. al.*, 1987, Elston *et. al.,* 1989). However, the presence of the metal layers meant that the technique was totally unsuitable for the study of cells produced commercially.

To allow commercial-style cells to be studied, a second optical waveguide technique was developed where the metal layers were replaced with transparent ITO electrodes on glass substrates of a refractive index higher than those of the liquid crystal. For light at angles of incidence below the critical angle between the prism and liquid crystal layer, the light enters the liquid crystal layer and is partially reflected at the lower substrate. A partially guided-mode is then supported when a constructive interference condition between the liquid crystal and glass interfaces is satisfied. Light is able to "leak" out of both substrates, and so transmitted and reflected optical intensity data can be collected, and the geometry is referred to as "fully-leaky". However, although this technique was successfully used to study the alignment in a surface-stabilised ferroelectric liquid crystal cell (Lavers et. al. 1990, 1991) the technique was abandoned as it had a low sensitivity to the director profile.

The third method developed was the half-leaky guided mode technique. The liquid crystal layer under investigation was sandwiched between a low-index glass substrate and a high index glass superstrate, which was then index matched to a high-index glass prism to allow light to be coupled into, and reflected light to be coupled out of the structure (Yang and Sambles, 1993). In the angle range between the two critical angles of the structure, the low index glass substrate acts as a perfect mirror (fig. 2.3). This technique proved highly successful for examining numerous cell geometries (Ruan and Sambles, 1995; Yang *et. al.,* 1999; Hodder *et. al.* 2001), but still had the disadvantage of requiring custom-made cells. The typical liquid crystal cells used in industry have low-index glass for both the substrate and superstrate, and hence only one critical angle exists, or perhaps, as is generally the case, none.

a)

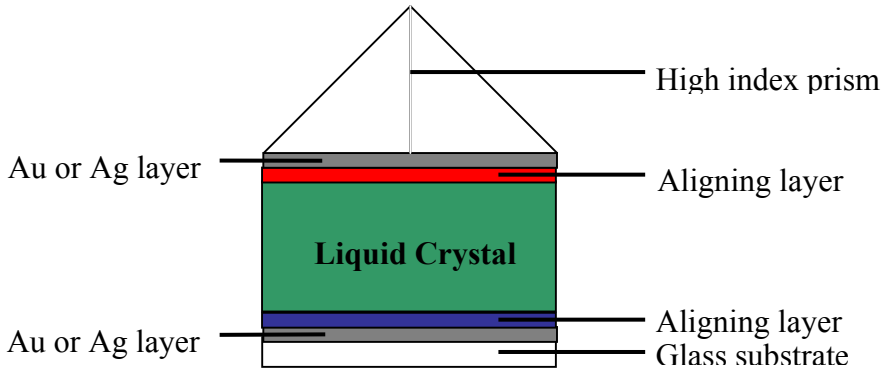

b)

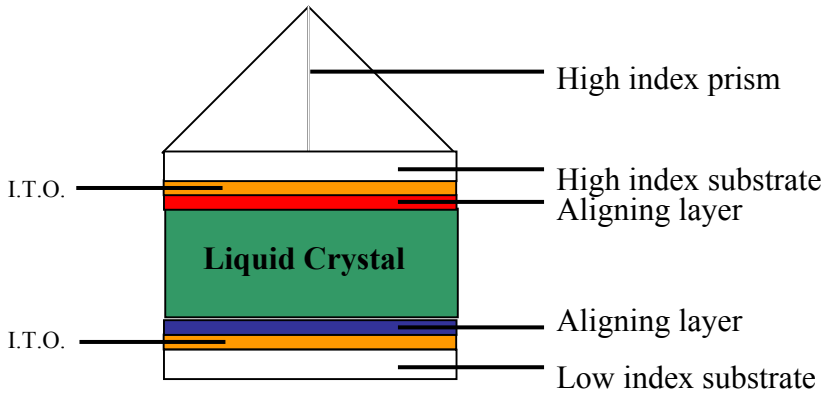

Fig. 2.7 Schematic diagram of the cell and prism layouts for a) Fully-guided mode technique, and b) The half-leaky guided mode technique.

2.8 Fully Leaky Guided Mode Technique (FLGM)

The extended fully-leaky guided mode technique (referred to in the remainder of this thesis as "the fully-leaky guided mode technique" or FLGM) is the most recently developed optical technique for measuring the static director profile within a liquid crystal cell (Yang and Sambles, 1999). The liquid crystal cell under investigation is a typical commercial-style cell with low-index glass substrates enclosing the aligned liquid crystal layer. The use of low-index prisms index-matched to the upper and lower substrates allows optical radiation to be coupled into and out of the structure. Unlike in the previous optical techniques, the difference in the critical angles at the two substrates is lost and so the guided modes become "fully-leaky". Weakly guided-modes are supported over a continuous range of angles of incidence, and so the variation of optical

intensity with angle of incidence shows very broad optical features. However, as the strong reflection from the lower substrate is now removed, light is transmitted through the cell. By recording the polarisation conversion signals (T_{ps} and T_{sp}) and polarisation conserving signals (T_{pp} and T_{ss}) for transmitted light, as well as that for the reflected light, a total of eight datasets can be obtained. Fitting to all eight datasets using a multilayer fitting routine still allows the director profile to be accurately determined.

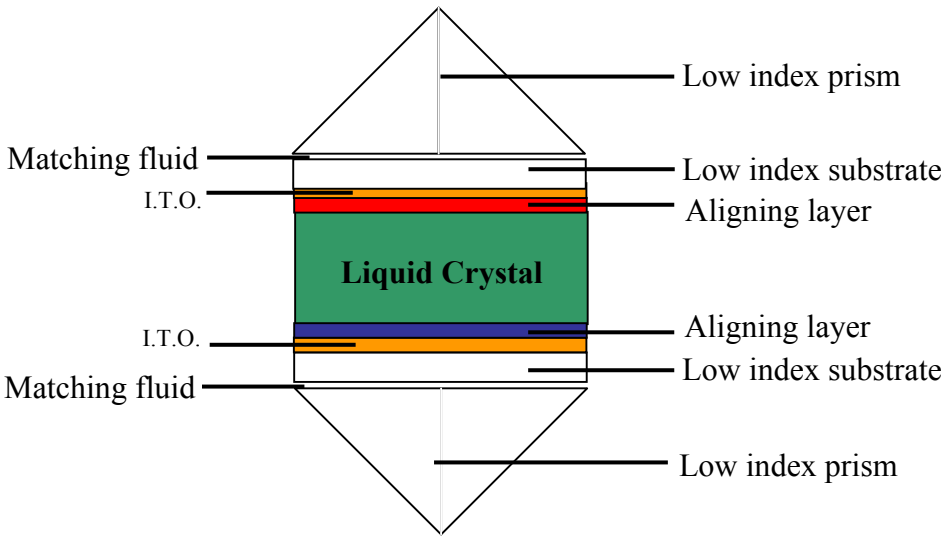

Fig. 2.8 Schematic diagram of the cell and prism arrangement for the fully-leaky guided mode technique

The most obvious advantage of this technique is that commercial cells can be examined in this way due to the equal refractive indices of the two substrates. (Hallam *et. al.* 1999; Yang *et. al.* 2000) This technique also has a second advantage as when the cell is mounted between the two low index prisms with matching fluid, it is possible to rotate the cell between the two prisms and data can be recorded for different azimuth angles. The cell can therefore be set to the azimuth angle which gives greatest sensitivity to the director twist and tilt. By fitting to two data-sets with different azimuths, any uncertainty in the deduced director profile can also be confidently removed.

2.8.1 Propagation length

For an incident wave propagating along the *x*-axis, of wavevector $k=k_r+ik_i$, the wavefunction Ψ of a wave of amplitude Ψ_0 is given by:

$$\Psi = \Psi_0 e^{i(kx-\omega t)} = \Psi_0 e^{i(k_r x-\omega t)} e^{-k_i x} \qquad \text{Eq. 2.20}$$

and the real and imaginary components of the wavevector in the guiding media are:

$$k_r = nk_0 \sin\theta \qquad \text{Eq. 2.21} \qquad k_i = nk_0 \cos\theta\,\Delta\theta \qquad \text{Eq. 2.22}$$

θ is the angle of incidence at the prism/liquid crystal interface, $\Delta\theta$ is the full-width half-maximum of a resonant mode centred at θ (fig. 2.9) and n is the refractive index of the coupling prism. The propagation distance L is defined as the distance at which the amplitude of the incident wave has decreased to Ψ_0/e. Therefore:

$$L = \frac{1}{k_i} = \frac{1}{nk_0 \cos\theta\,\Delta\theta} = \frac{\lambda_0}{2\pi n \cos\theta\,\Delta\theta} \qquad \text{Eq. 2.23}$$

where λ_0 is the wavelength of the incident light. Values for θ and $\Delta\theta$ can be obtained from the optical data collected from FLGM experiments (Fig. 2.9)

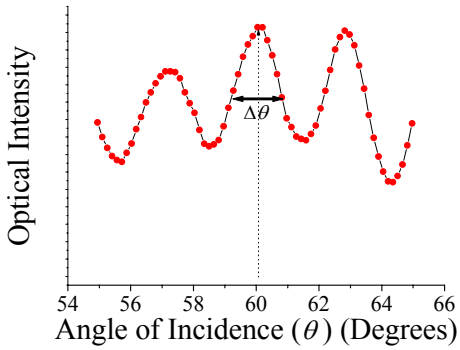

Fig. 2.9 Example of FLGM data showing typical values for the width of a resonance mode in a 5μm HAN cell

Typically, for a FLGM measurement using λ_0=632.8nm and a low-index prism of n=1.52, a resonance occurring at 60° has a width of $\Delta\theta \approx 1.4°$, and so ***L*=5μm**, which is significantly smaller than the bean spot size of approximately 200μm. In contrast, if the fully-guided method is used with n = 1.80, and $\Delta\theta \approx 0.004$rad, ***L*=28μm**.

2.8.2 Experiment layout

Data is collected by mounting the cell and prism arrangement in the centre of a computer-controlled rotating table. The table is set to rotate in steps of size $d\theta$, over a pre-defined angle range. Light from a 0.5mW Helium-Neon laser (λ = 632.8nm) passes through an optical chopper to allow signal detection by the use of a PSD. Polarisers are then used to select either TE or TM polarised light, and it is incident on the upper prism.

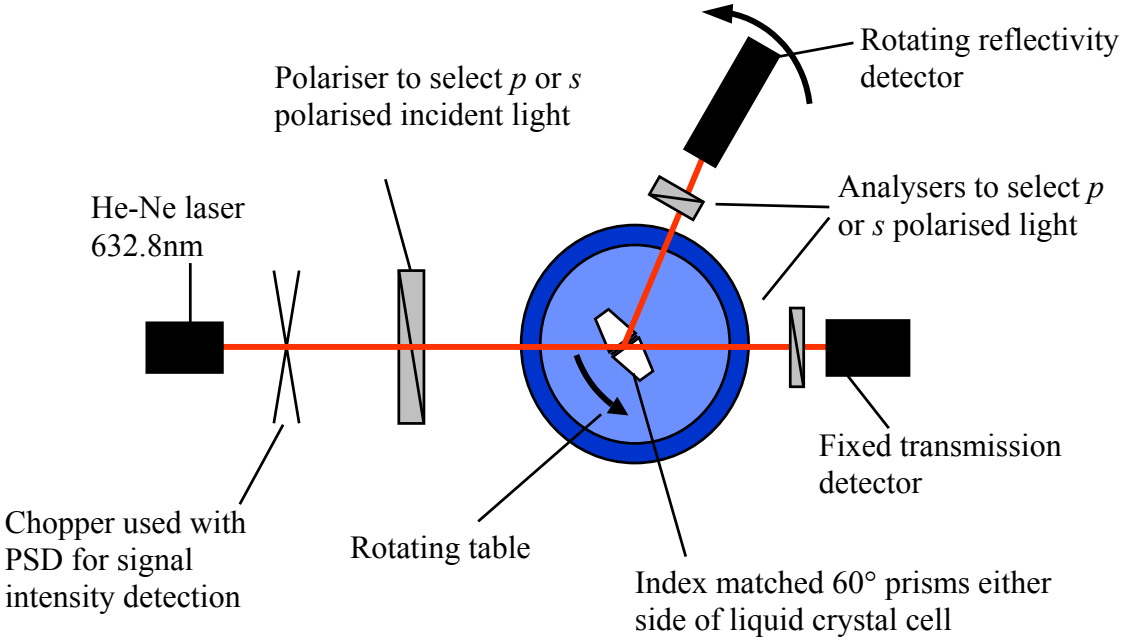

Fig. 2.10 Schematic diagram of the equipment used in the fully-leaky guided-mode technique

At each angle of incidence, fully-leaky guided-modes are set-up in the liquid crystal layer, for which the propagation distance along the layer is short ($\cong$ 5 μm). The intensity of light transmitted and reflected at this angle is recorded by two photo-diode detectors with polarisers on the front to select either TE or TM polarised light. For the transmitted beam, the detector is fixed at a point co-linear with the laser and the beam-spot at the liquid-crystal layer. A detector mounted on a rotating plate which, due to the geometry of the system, is required to step through $2d\theta$ for each angle of incidence, monitors the reflectivity. A reference beam is also monitored simultaneously for each point to allow any fluctuations in laser intensity to be removed. The set-up used allows

reflected and transmitted light to be collected simultaneously, and so to obtain all eight datasets required, the angle scan must be run four times, twice to collect polarisation converting signals (*p*- to *s*-, and *s*- to *p*-) and twice to collect the polarisation conserving data.

2.8.3 Fitting to data

For each dataset, the angle of incidence at the liquid crystal layer is calculated from the external angle of incidence (θ_{ext}). The intensity is then normalised to 1 with respect to the full intensity of a straight-through *p*- or *s*- polarised beam and Fresnel's equations are used to correct for partial reflections at the glass/air interfaces.

Model data is generated by using a multi-layer optics program (based on a 4X4 Berreman matrix), which uses the refractive index, absorption and thickness of all the optical layers in the cell as input parameters, as well as the director structure through the cell. The measured data is compared with theory and the sum-of-squares of the difference between the two is calculated. The parameters in the modelling program are then varied, a new set of model data is generated and the new sum-of-squares is calculated. This direct search process continues until the sum-of-squares cannot be improved by varying any of the parameters.

In the original fitting routine used to fit to the optical data, a 'piecewise' method was used to describe the director profile through the cell. The liquid crystal layer was divided up into *n* number of layers, and the tilt angle at the top and bottom of each layer was defined and allowed to vary linearly through each layer. In subsequent versions of the program, a continuous mathematical function was used to define the tilt profile through the entire liquid crystal slab. In the case of the HAN cells studied in this thesis, it was found that the profile could be accurately described by using a third order rational Bezier function (Eq. 2.20).

$$\theta = \frac{A_1 z^3 + 3A_2 z^2(z-1) + 3A_3 z(z-1)^2 + A_4(z-1)^3}{z^3 + 3A_5 z^2(z-1) + 3A_6 z(z-1)^2 + (z-1)^3} \qquad \text{Eq. 2.24}$$

In this expression, $0 < z < 1$ and is the fractional distance through the cell. The coefficients A_n are used as fitting parameters. A_1 is the tilt angle at the incident substrate,

and A_4 is the tilt angle on the other surface. A_2 and A_3 are intermediate angles and A_5 and A_6 are weighting coefficients.

2.8.4 Sensitivity to orientation

To highlight the sensitivity of the technique to the director structure, and its advantage over integrated techniques, fig. 2.11 shows model data for a HAN cell collected with either the homeotropic alignment (solid line) or the homogeneous alignment (dotted line) on the incident surface. The asymmetric nature of the EM field distribution across the waveguide results in dramatically different data being produced for the two cell orientations. For instance, in the region where the director is homeotropically aligned (or very close to it) the incident light is most sensitive to the ordinary refractive index of the material, and hence highly insensitive to the azimuthal orientation (assuming that the material is uniaxial). Conversely, in the homogeneous region, the extra-ordinary refractive index dominates the data produced, and the azimuth at which the cell is oriented is highly significant.

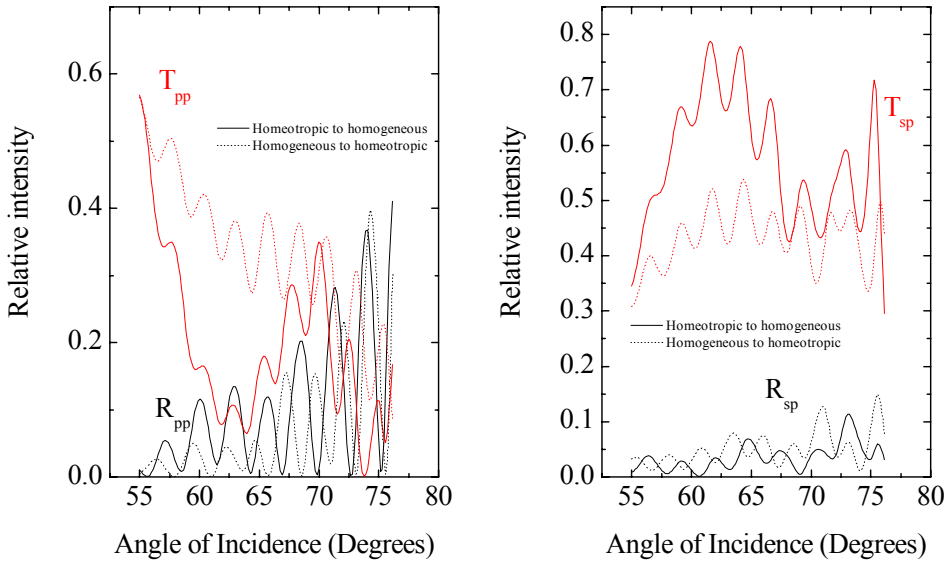

Fig. 2.11 Modelled optical intensity vs. angle-of-incidence data for a HAN cell orientated at 60° with either the homeotropic or homogeneous alignment as the incident surface. a) *p*-polarisation conserving and b) *s*- to *p*-polarisation converting signals are shown for reflected and transmitted light.

A second issue that must be considered in the collection of optical data from a HAN cell is the direction of the tilt through the cell, i.e. whether the cell is tilting through +90° or -90°, as illustrated in Fig. 2.12.

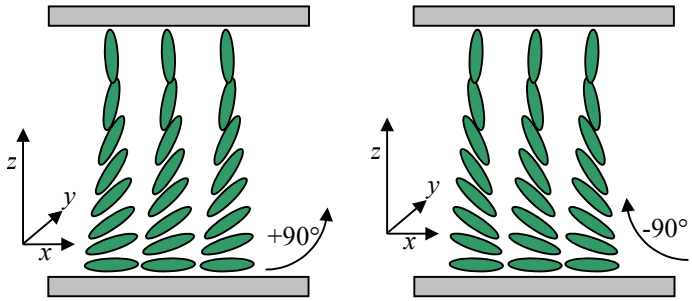

Fig.2 12 Demonstration of the two tilt orientations possible in a HAN cell.

In essence, orientation (b) is simply a 180° rotation of profile (a) about the *z*-axis. However, when the optical intensity vs. angle-of incidence data is modelled for the two cases, the results are very different (Fig. 2.13). The consideration of tilt direction is particularly important when pretilt-free alignment techniques, such as SiO_x deposition is used. The absence of surface memory allows either orientation to form on cooling from the isotropic phase in small domains across the cell, and hence two different regions can produce different optical data.

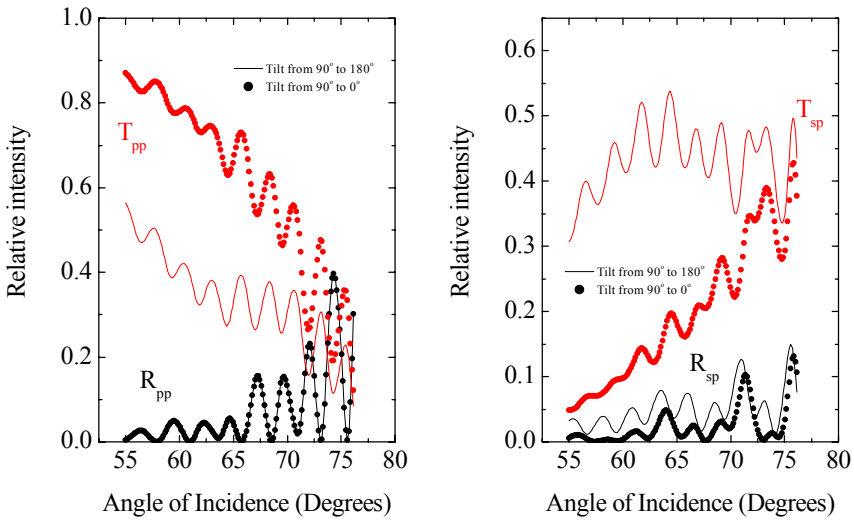

Fig. 2.13 Modelled optical data for a HAN cell oriented with tilt either from 90° to 180° or 90° to 0° orientation at a 60° azimuthal angle.

2.9 The Convergent Beam Technique – Dynamic measurements

The convergent beam technique is a relatively new method developed by Smith and Sambles (2000) to allow optical guided mode studies of liquid crystal dynamics. The waveguide arrangement used is fully-leaky, with the cell constructed from low-index substrates. However, the cell is now index matched between two low-index glass hemispheres, as shown in Fig. 2.14. The fully-leaky guided modes are then excited simultaneously over a range of angles by expanding a beam from a HeNe laser, and focussing it down to a point on the cell to be studied.

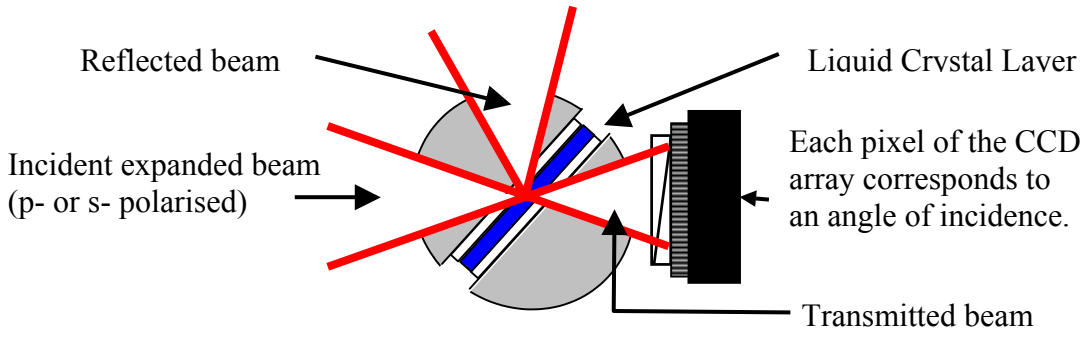

Fig. 2.14 Schematic diagram of the cell and hemisphere arrangement used in the convergent beam technique.

The optical intensity for the reflected and transmitted light is collected using a CCD (charge coupled device) camera with a 1 X 2048 pixel array, with each pixel corresponding to light incident at a particular angle. By using a suitable capture time for the CCD array (i.e. <1ms) the optical intensity at each pixel can be recorded over a period of time, and hence optical data corresponding to a change in director profile with time (e.g. due to a change in applied voltage) can be recorded.

As in the static case, 8 datasets are recorded in total (4 reflected and four transmitted). For each time-slice, the 8 datasets of optical intensity vs. angle of incidence data are fitted to theory using the same fitting routine as used in the static case.

2.9.1 Experiment layout

The experimental layout for the convergent beam technique is shown in Fig. 2.15. The light source used is a high power (35mW) HeNe laser. The power of the beam is an important consideration, as a high intensity is required to allow a suitable intensity of optical data to be collected during the short capture time of the data. However, the process of focussing the beam to a 100μm spot size means that local heating of the liquid crystal can occur.

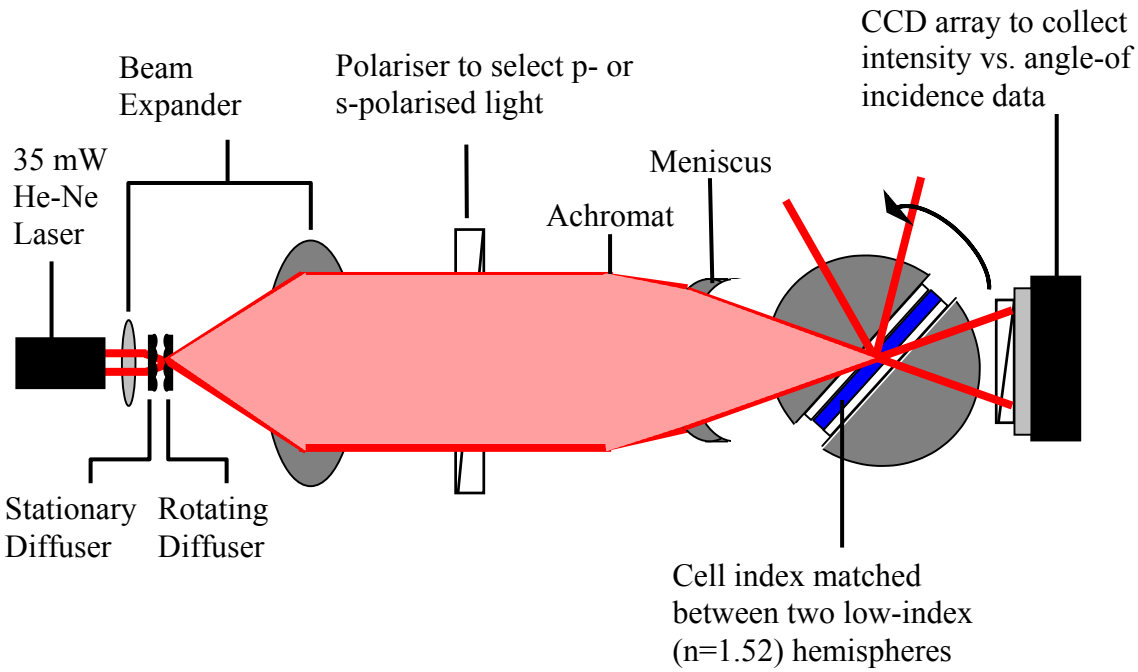

Fig. 2.15 Schematic diagram of the layout of the convergent beam technique

The narrow, collimated beam passes through a lens of focal length 9.5mm to expand the beam. At the focal point of this lens is a stationary diffuser (i.e. a piece of diffuse glass). The purpose of this is to break up the spatial coherence of the beam and to prevent constructive interference occurring. In the absence of this diffuser, a systematic interference pattern is seen across the beam profile when the data is collected by the CCD array. This static diffuser also ensures that the intensity of the beam is more uniform across the expanded beam diameter, removing the strong gaussian intensity profile, which would otherwise exist. The rotating diffuser is required to break up the

temporal coherence of the beam, as systematic variations in the intensity of the beam over the duration of the data collection period manifests themselves as bands of high and low intensity in the data collected. It is the speed of this rotating diffuser that determines the minimum capture time that the CCD can be operated at i.e. the higher the speed of the diffuser, the faster the data can be captured. The turbine used for the diffuser in this case is a dental drill, powered by compressed air. The diffuser attached to the spindle is a piece of tracing paper, chosen due to its light weight and isotropic nature.

After the expanding lens, a collimating lens of focal length 205mm is used to maintain a beam diameter of around 40mm along the bench. The collimated beam passes through a polariser to select *p*- or *s*- polarised light, and the beam is then focussed down to a point using an achromat and meniscus arrangement. The achromat is virtually free from spherical and chromatic aberration, providing a focal length independent of aperture size. The meniscus is then used to shorten the focal length of the achromat. The position of these lenses is adjusted to ensure that the beam is focussed onto the central axis of a circular plinth onto which the cell and hemispheres are mounted. Finally, the beam enters the CCD array, which is at the beam height, but tilted downwards by ~20° to prevent interference at the face of the detector.

2.9.2 Cell orientation

To ensure that the data collected are accurate, the cell has to be oriented correctly in all three planes. Prior to inserting the hemisphere arrangement, a prism of angle equal to the required central angle of incidence is mounted normal to the beam at the focus of the system, and the position of the reflected principal ray is marked on the wall. The prism is removed, and the position of the 'straight through' principal ray is also marked. The hemispheres are replaced, and with the use of the beam from a low-power diode laser, also passing through the focus, but at 90° to the principal ray, the position of the hemispheres is adjusted so that the two beams are coincident at the point on the cell under test, and all the beams are incident and reflected in the same plane.

2.9.3 Critical edge measurement

The distance of the CCD array from the focus of the convergent beam is required to allow the angle corresponding to each pixel to be determined. This distance is measured by using the CCD array to take a critical-edge scan of a single hemisphere. The hemisphere is arranged so that the principal ray is reflected at a 45° angle (Fig. 2.16(a)) and the CCD camera is centred on the principal ray. A line of optical intensity vs. angle-of-incidence data is collected (fig. 2.16(b)) in the same way as for the dynamic data. From the value of the critical angle and the pixel number at which it occurs, the distance from the CCD array to the focal point can be calculated from the simple geometry.

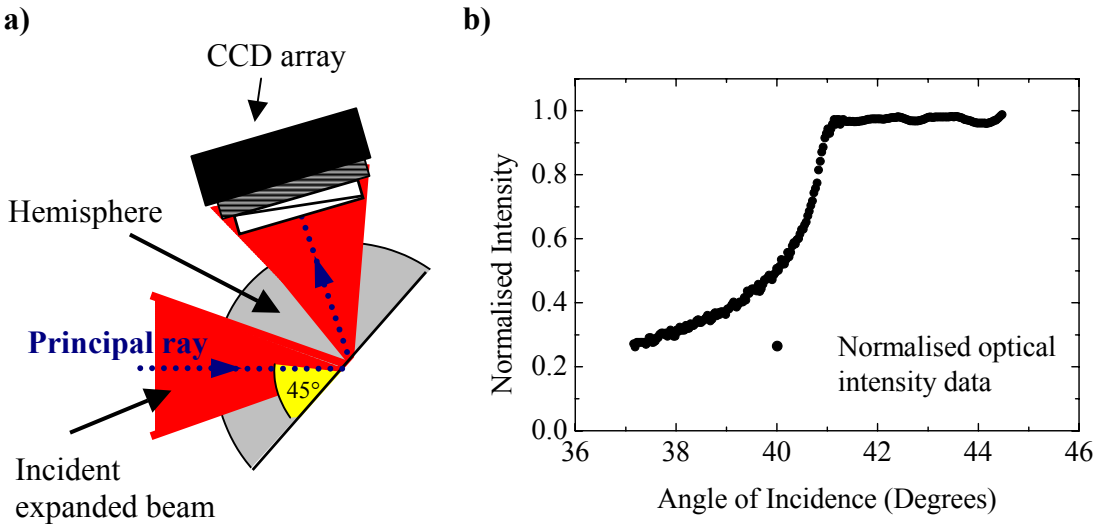

Fig. 2.16 **a) Hemisphere arrangement used to measure the position of the critical edge of a low-index prism on the CCD array and b) Typical critical edge optical intensity vs. angle-of-incidence data collected.**

2.9.4 Dynamic data collection

The operation of the CCD camera is controlled by a PC, which is interfaced with the voltage supply connected to the cell under test. This makes the dynamic data collection process relatively straightforward as a single trigger button can be pressed to change the applied voltage and trigger the data-collection feature of the camera

simultaneously. In theory, the minimum data capture period achievable by the CCD array is 0.075ms, however, in practise, due to the restrictions imposed by light intensity and diffuser speed, a capture time of ≈ 0.2ms is used. In the current set-up for the convergent beam kit, only one CCD camera is used, so the process must be performed 8 times to collect all the required data, 4 with the camera centred on the transmitted principal ray, and four with it centred on the reflected one.

To allow the data collected to be normalised, and to correct for any variations in pixel sensitivity, once all of the required data-sets have been collected the cell is removed and 'straight through' scans are taken. In the case of the transmitted light, this scan is taken using two pieces of low index glass index-matched between the two prisms, and several lines of data are taken using the CCD camera set at the same capture time as for the data collection process. For the reflected intensity, one hemisphere is mounted at the focus, at an angle of incidence above that of the critical angle, and the reflected intensity is recorded as before. Finally, the angle of incidence corresponding to each pixel is calculated, to correct for the radial distribution of the detected beams and the flat face of the CCD detector. A more detailed explanation of the normalisation process and the specifications of the system is given by Smith (2001).

Once normalised, the data is in the form of a matrix, composed of lines of data showing the intensity of light at each pixel for each time-step after the voltage is either applied or removed, and each line is fitted-to individually

This measurement technique has proved extremely successful, and has enabled the dynamics of liquid crystal cells to be studied in the sub-millisecond timescale. The change in director profile with time has allowed such phenomena as backflow to be quantified in the relaxation process of a twisted nematic cell and the measurement of the viscosity coefficients of a liquid crystal (Smith *et. al.*, 2002).

2.10 Conclusions

A concise introduction to the basic properties of fully guided, half-leaky and fully-leaky waveguides has been given for planar, isotropic tri-layer structures. The discussion has then been extended to waveguides containing an aligned, uniaxial liquid crystal layer. Maxwell's equations have been solved for this situation to show the variation in intensity of the electro-magnetic field across the waveguide.

Several different optical techniques used for characterising the static director profile in a liquid crystal cell have been introduced, and the advantages and disadvantages associated with each have been commented on. The fully-leaky guided-mode technique, currently used to study the static director profile in commercial style liquid crystal cells has been discussed in detail, and specific considerations required when using the method to study hybrid aligned nematic cells have been highlighted.

Finally, the convergent-beam technique, used to explore the dynamics of the director profile of a liquid crystal cell due to a change in voltage has been discussed. A detailed description of the optics and operation of the experiment has been given, and examples of measurements already made have been given to highlight typical measurements achievable with this arrangement.

Chapter 3

The Flexoelectric Effect in a Hybrid Aligned Nematic Cell

3.1 Introduction

When certain solids, generally those composed of dipolar molecules, are distorted by an external force e.g. a physical strain or compression, a net macroscopic polarisation is set up within the material. This effect is known as piezoelectricity. The reverse situation is also possible, where the application of an external electric field can induce a physical distortion in the material.

An analogous effect in liquid crystals was proposed by Meyer (1968) to account for field effects occurring in liquid crystal structures that, until then, could not be accounted for by the dielectric anisotropy of the material alone. He suggested that by distorting the alignment of the molecules, a net macroscopic polarisation could be induced. Due to the incompressibility (other than bulk compression) of a liquid crystalline material, this distortion cannot be produced by a pure compressive or extensive force, but can instead be caused by dictating the alignment of the director within a liquid crystal cell. The inverse effect can also be produced by applying an electric field across the material.

Despite the key differences with the solid-state case, Meyer referred to this phenomena as the “piezoelectric effect”, and this term was used in literature until De Gennes (1974) coined the term “Flexoelectric effect” to remove any ambiguity.

3.2 Flexoelectric Theory - Dipolar Model

Meyer attributed the flexoelectric effect to the liquid crystal molecules possessing a permanent dipole moment and a shape asymmetry. The molecules may either have a dipole along the long axis, resulting in it being "pear" shaped, or alternatively, the dipole may be along the transverse axis, producing a banana shape.

In the isotropic phase, the random orientation of the molecules causes the dipoles to cancel on a macroscopic scale (fig. 3.1(a) and (c)). However, if a system of pear shaped molecules is constrained to a splay geometry ($\hat{\mathbf{n}}(\nabla \cdot \hat{\mathbf{n}}) \neq 0$) the asymmetry of the distribution produces a net polarisation across the cell (fig. 3.1(b)). The magnitude and direction of the field is determined by the splay flexoelectric constant e_1. The same situation is true for a system of banana shaped molecules constrained to a bend geometry ($\hat{\mathbf{n}} \times (\nabla \times \hat{\mathbf{n}}) \neq 0$) (fig. 3.1(d)). In this case, it is the bend flexoelectric constant, e_3, which determines the magnitude and direction of the field. Due to symmetry, a pure twist deformation *does not* result in a net polarisation (Rudquist and Lagerwall, 1997), and so only the two flexoelectric coefficients mentioned exist. The total flexoelectric polarisation, $\mathbf{P}_f$ is therefore given by the sum of the splay and bend contributions to the flexoelectric field.

$$\mathbf{P}_f = e_1 \hat{\mathbf{n}}(\nabla \cdot \hat{\mathbf{n}}) + e_3 \hat{\mathbf{n}} \times (\nabla \times \hat{\mathbf{n}}) \qquad \text{Eq. 3.1}$$

These splay and bend distortions can be produced by confining the director to a non-twisted hybrid-aligned nematic geometry, where the director tilts through 90° from the homogeneous to the homeotropic substrate. When a DC voltage is applied across the cell, the resulting distortion in the director profile cause a change in the bend and splay distribution, and hence alters the induced polarisation. Depending on the polarity of the applied field, the internal flexoelectric field either enhances or suppresses the dielectric response of the director, and so forward and reverse bias DC voltages produce differing director profiles. In both cases, the equilibrium director configuration is where the sum of the elastic, dielectric and flexoelectric distortion energies are minimised.

This theory has been verified theoretically in a study by Billeter and Pelcoutis (2000) involving the Monte-Carlo simulation of a series of asymmetrically shaped

molecules, and the calculation of the corresponding flexoelectric coefficients. Experiments have further confirmed the dipolar model (Murthy et. al., 1993), by the measurement of the flexoelectric coefficients for a number of liquid crystal molecules of differing shape and dipole moment.

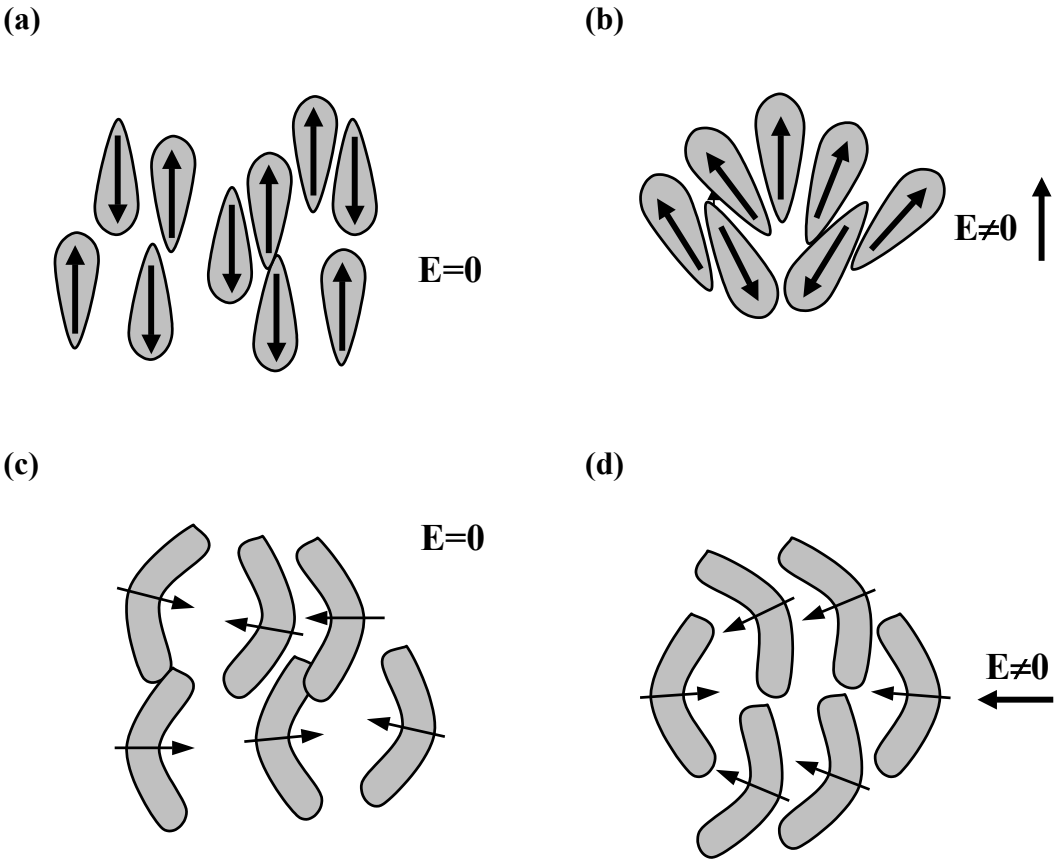

Fig. 3.1 Schematic diagram of a) Isotropic configuration and splay deformation of pear shaped liquid crystal molecules, and b) isotropic configuration and bend deformation of banana shaped liquid crystal molecules

3.3 Flexoelectric Theory – Quadrupolar Model

The dipolar, asymmetric shape theory of flexoelectricity proposed by Meyer produces a simple and intuitive argument for the presence of an internal field when a director is constrained to a splay and bend geometry. However, Marcerou and Prost (1977) proposed that an internal, flexoelectric field could also be produced by symmetrically shaped quadrupolar molecules.

When the cigar-shaped molecules are in the isotropic phase, and close packing is assumed, the net field produced by the quadrupoles is zero (fig. 3.2(a)). However, when they are confined to a splay structure, the charge distribution becomes uneven. As highlighted in fig. 3.2 (b), imposing a splay deformation results in an excess of positive charge in the upper region of the central layer, whilst effectively excluding charge from the lower region. This results in a macroscopic polarisation, and hence an internal flexoelectric field.

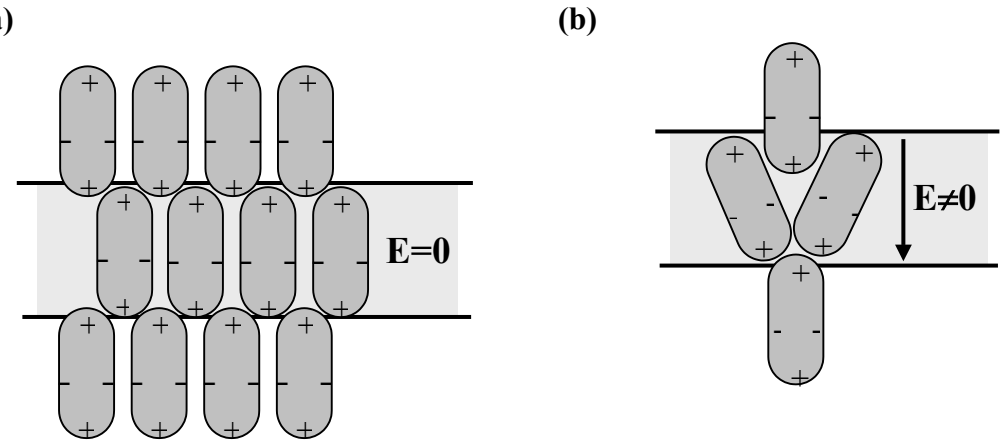

Fig. 3.2 Modelled quadrupolar molecules (a) in the isotropic phase and (b) under a splay distortion resulting in a macroscopic polarisation

This theory was first verified experimentally (Prost and Marcerou, 1980) by the measurement of the flexoelectric constant of the symmetric liquid crystal compound p,p'-dihexyloxytolan ("symmetric tolan"), using a light scattering technique to measure the distortion to the optic axis of a homeotropically aligned sample when a modulated DC voltage was applied.

In both models, the flexoelectric field is present in the HAN cell, even when the cell is shorted. As discussed later in this chapter, in the absence of ionic contaminants and surface polarisation, this permanent field is valid provided the integral of the field across the cell is zero.

3.4 Flexoelectric Free-Energy Calculation.

For a HAN cell with no twist (i.e. containing no chiral dopaant), the director is constrained to a pure splay and bend geometry. The director tilts through the cell (i.e. along the *z*-axis) from $\theta \approx 0°$ (homogeneous alignment) to $\theta \approx 90°$ (homeotropic alignment), the exact surface tilts depending on the pre-tilt produced by the aligning medium. The azimuthal twist angle ϕ is assumed to be of a constant value throughout the cell.

For a HAN cell of thickness *d*, with a static director profile **n** due to a displacement field **D** and an applied electric field **E**, the total free-energy density of the system is given by the sum of the elastic and electrostatic contributions (De Gennes, 1974):

$$G = \int_0^d \left[\frac{1}{2}\left(K_{11}\left(\mathbf{n}(\nabla \cdot \mathbf{n})\right)^2 + K_{22}\left(\mathbf{n} \cdot (\nabla \times \mathbf{n})\right)^2 + K_{33}\left(\mathbf{n} \times (\nabla \times \mathbf{n})\right)^2 \right) + \frac{1}{2}\mathbf{D} \cdot \mathbf{E} \right] dz \qquad \text{Eq. 3.2}$$

where K_{11}, K_{22} and K_{33} are the splay, twist and bend elastic constants respectively. The displacement field **D** has contributions due to the applied field **E** and the flexoelectric polarisation **P**, and is given by:

$$\mathbf{D} = \varepsilon_0 \underline{\underline{\varepsilon}}\, \mathbf{E} + \mathbf{P} \qquad \text{Eq. 3.3}$$

Where $\underline{\underline{\varepsilon}}$ is the dielectric tensor of the liquid crystal, from which the extra-ordinary and ordinary dielectric constants for the material are denoted by $\varepsilon_\perp$ and ε_{ll}. In the absence of twist, only the splay and bend elastic energies contribute to the total elastic free-energy. As shown in fig. 3.3, the HAN cell geometry can be considered invariant along the *x*- and *y*- axes, and hence $\partial/\partial x = \partial/\partial y = 0$. The unit director is therefore given by:

$$\mathbf{n} = \cos\theta\, \hat{\mathbf{x}} + \sin\theta\, \hat{\mathbf{z}} \qquad \text{Eq. 3.4}$$

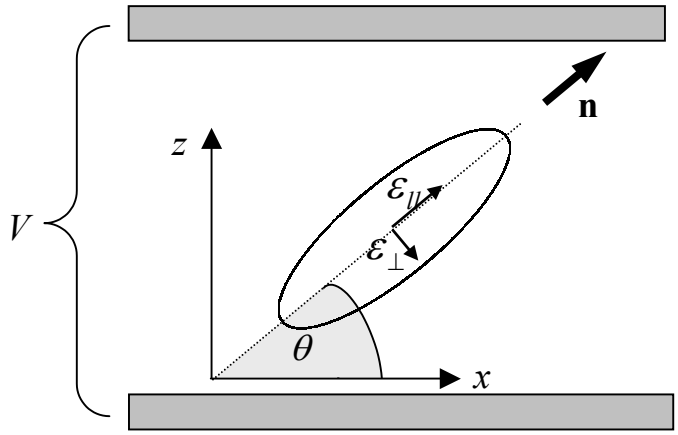

Fig. 3.3 Schematic diagram to show the orientation of the director, n, in a HAN cell relative to the substrate and applied voltage.

The elastic contribution to the free-energy density, $G_{elastic}$ simplifies to:

$$G_{elastic} = \int_0^d \left[\frac{1}{2}\left(K_{11}\cos^2\theta + K_{33}\sin^2\theta\right)\left(\frac{d\theta}{dz}\right)^2 \right] dz \qquad \text{Eq. 3.5}$$

In the case of the electrostatic contribution, only electric fields applied along the z-axis (perpendicular to the substrate) will be considered, as this is the geometry used in all of the studies contained within this thesis. Therefore, E_x=E_y=0 and so $\mathbf{E} = E_z\hat{\mathbf{z}}$

The flexoelectric polarisation **P** is given by the sum of the splay and bend contributions, with e_1 and e_3 being the splay and bend flexoelectric coefficients respectively.

$$\mathbf{P} = e_1\mathbf{n}\left(\nabla\cdot\mathbf{n}\right) + e_3\mathbf{n}\times\left(\nabla\times\mathbf{n}\right) \qquad \text{Eq. 3.6}$$

In the HAN geometry, this becomes:

$$\mathbf{P} = \left(e_1\cos^2\theta + e_3\sin^2\theta\right)\frac{d\theta}{dz}\hat{\mathbf{x}} + \sin 2\theta\,\frac{\left(e_1+e_3\right)}{2}\frac{d\theta}{dz}\hat{\mathbf{z}} \qquad \text{Eq. 3.7}$$

From the electrostatic contribution to the free-energy density in eq. 3.2 it is clear that as **E** = $E_z(z)$, only the z-component of the **D**·**E** term is non-zero.

$$D_z = \varepsilon_0\left(\varepsilon_{//}\sin^2\theta + \varepsilon_\perp\cos^2\theta\right)E_z(z) + \sin 2\theta\frac{\left(e_1+e_3\right)}{2}\left(\frac{d\theta}{dz}\right) \qquad \text{Eq. 3.8}$$

The boundary conditions for this structure are such that the component of **D** normal to the substrate (D_z) is continuous through the cell and hence the same at every point in the structure. However, $E_z(z)$ may vary from point to point, provided that the integral of the field across the cell is equal to the applied voltage. It is therefore preferable when considering the electrostatic situation to work in terms of D_z instead of $E_z(z)$. By rearranging eq. 3.8, an expression for $E_z(z)$ can be obtained, and so the electrostatic contribution to the total free-energy density, G_{elec}, is given as a function of the director profile and the gradient of the director profile:

$$G_{elec} = \frac{1}{2}\int_0^d\left[\frac{{D_z}^2}{\varepsilon_0\left(\varepsilon_{//}\sin^2\theta + \varepsilon_\perp\cos^2\theta\right)} - \frac{D_z\sin 2\theta\left(e_1+e_3\right)}{2\varepsilon_0\left(\varepsilon_{//}\sin^2\theta + \varepsilon_\perp\cos^2\theta\right)}\left(\frac{d\theta}{dz}\right)\right]dz \qquad \text{Eq. 3.9}$$

It is clear from this expression that for a given HAN cell geometry with $d\theta/dz > 0$, the application of a positive field (resulting in a positive value of D_z) will lower the total free-energy. Conversely, for the same sign of the director gradient, the application of a *negative* field will have the effect of *increasing* the free energy. In both cases, the equilibrium profiles in the bulk will remain stable for the duration of the applied fields, but for the positive and negative fields different director profiles are required to minimise the free energy.

3.5 Role of flexoelectricity in liquid crystal devices

Although the flexoelectric effect in HAN cells containing commercial liquid crystal compounds appears to be a subtle effect on the director profile, the presence of a permanent dipole and the influence of this on the free-energy of the system can be exploited, as described below in two brief descriptions of possible applications of the HAN cell geometry.

3.5.1 Zenithal Bistable Devices

In chapter 1, the use of the HAN state as one of the two stable states in a Zenithal Bistable Device (ZBD) was discussed. Recent work by Davidson and Mottram (2002) and Denniston and Yeomans (2001) has highlighted how the influence of the flexoelectric field at the bistable surface of a ZBD results in the switching between the two stable states, (which are of similar energy).

When concerned only with surface effects, the applied electric field $E_z(z)$ can be approximated as being constant through the cell, hence $E_z(z)=E_z$. By replacing D_z in eq. 3.9 with eq. 3.8, an expression for the free-energy in terms of E_z can be obtained.

$$G_{elec} = \frac{1}{2}\int_0^d \left[2{E_z}^2 \varepsilon_0 \left(\varepsilon_{//} \sin^2\theta + \varepsilon_\perp \cos^2\theta\right) + \frac{\sin^2 2\theta \left(e_1+e_3\right)^2}{\varepsilon_0\left(\varepsilon_{//} \sin^2\theta + \varepsilon_\perp \cos^2\theta\right)}\left(\frac{d\theta}{dz}\right)^2 - \frac{3E_z \sin 2\theta\left(e_1+e_3\right)}{4}\left(\frac{d\theta}{dz}\right)\right] dz \qquad \text{Eq. 3.10}$$

The third term in this expression is independent of the dielectric anisotropy, and can be converted into an integral between θ_0 (the angle at the bistable surface) and θ_d (the angle at the homeotropic surface, assumed to be 90°) and integrated out as a surface term:

$$G = G_{bulk} + G_{flexo\,surface} = G_{bulk} - \frac{3E_z \cos 2\theta_0 \left(e_1+e_3\right)}{4} \qquad \text{Eq. 3.11}$$

When the device is in the HAN state (θ_0 = 0°), the application of a negative electric field will make the flexoelectric surface free-energy positive, raising the total free-energy of the HAN state (fig. 3.4 (a)). Consequently, the value of $G_{flexo\ surface}$ of the vertical state (θ_0 = 90°) will be of a lower value (fig. 3.4 (b)) making the vertical state more energetically desirable, and so the cell will switch to the vertical state. When the field is removed (E_z = 0), both states once again have the same energy and so the cell remains in the vertical state. The device will stay in this state indefinitely unless a *positive* electric field is applied to the device. In this situation the surface energy of the HAN state is lower than that of the vertical (fig. 3.4 (c)), and so the cell will switch back to the HAN state.

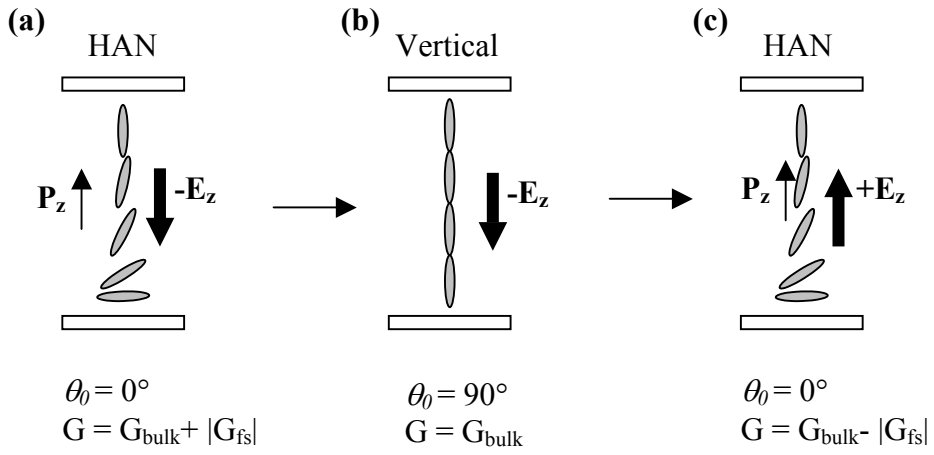

Fig. 3.4 **Schematic diagram showing the energies associated with the two stable states of a ZBD devices when (a) a negative voltage is applied to the stable HAN state; (b) a negative voltage is applied to the stable vertical state and (c) appositive voltage is applied to the HAN state.**

3.5.2 Optical Plane of Polarisation Rotator

A novel use of a HAN cell as a rotator of the plane of polarised light was suggested by Dozov et. al. (1982). By constructing a HAN cell as before, but using in-plane electrodes to apply a field along the *y*-axis (i.e. perpendicular to the plane of the director (fig. 3.5)), an azimuthal twist can be induced due to the torque exerted by the applied field, E_y on the dipoles. As the field is perpendicular to the *z*-axis, the tilt profile remains unchanged on the application of the field, maintaining a near-linear variation through the cell from 0° to 90°.

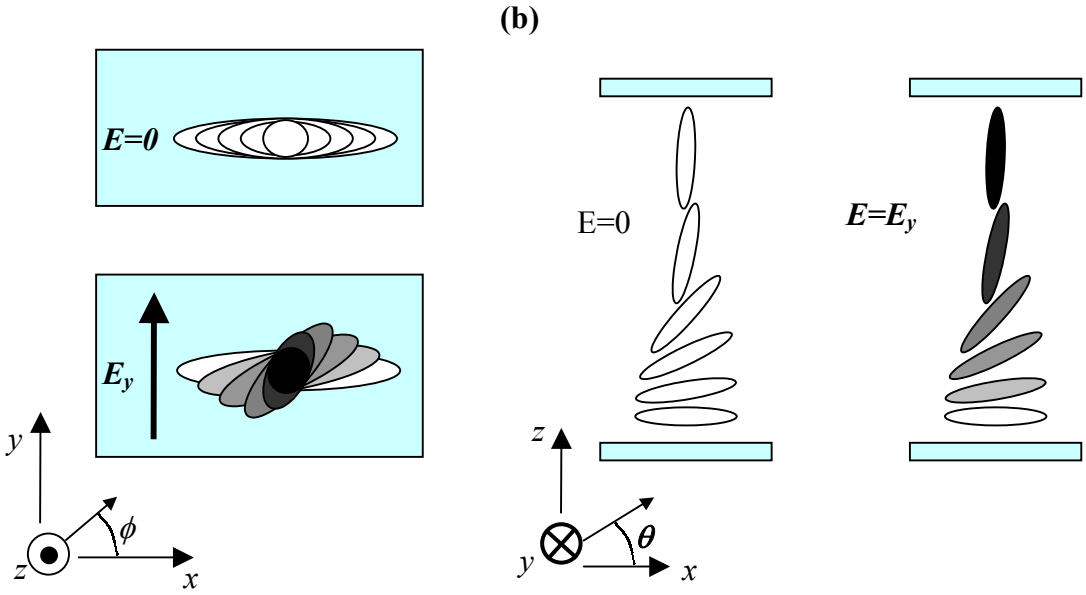

Fig. 3.5 Schematic diagram showing the general director orientation for a HAN cell with and without an applied in-plane field E_y when viewed (a) from above (in the *x*-*y* plane) and (b) from the side (in the *z*-*x* plane). (The shading indicates the amount of deviation of the twist from $\phi = 0°$.)

The electrostatic free-energy is due to the coupling between the in-plane flexoelectric polarisation and the applied field, (assuming that the dielectric anisotropy is negligible) and in this case it is given by:

$$G_{electrostatic} = -\mathbf{P} \cdot \mathbf{E} = -E_y (e_1 - e_3) \sin^2 \theta \sin \phi \frac{d\theta}{dz} \qquad \text{Eq. 3.12}$$

By minimising the sum of the elastic and electrostatic free energy the total azimuthal twist through the cell (ϕ) can be determined. Using a one elastic constant approximation $K_{11} = K_{33} = K$, and assuming that the tilt profile through the cell is approximately linear and the applied DC field is small, the induced twist across a cell of thickness d can be shown to be proportional to the applied field:

$$\phi = \frac{(e_1 - e_3) E_y d}{\pi K} \qquad \text{Eq. 3.13}$$

As a result, light entering the cell through the homogeneously aligned surface and polarised parallel to the x-axis will exit the cell with its plane of polarisation rotated through an angle ϕ. In practice, Dozov et al found that a rotation of up to ± 20° could be obtained by the application of a field of ± 40 Vmm^{-1} across a MBBA-filled cell of thickness 40μm.

Although this technique has not been used commercially, it has the potential for use as a device to control the plane of polarisation of incident light.

3.6 Development of a Static Flexoelectric Modelling Program

The expression for the total free-energy of a HAN cell is a function of θ and $d\theta/dz$ only, and can be used to calculate the static director profile for any combination of elastic, dielectric and flexoelectric constants. This premise has been used to develop a modelling program, based on original work by Welford and Sambles (1987), to allow the subtle distortions to the equilibrium director profile produced by the presence of a flexoelectric field to be investigated. The equilibrium profile at an applied voltage V can be calculated by minimising the total free-energy using the Euler-Lagrange variational principal (Thurston and Berreman, 1981; Ponti et. al., 1999). The Euler-Lagrange equation in this case is:

$$\frac{d}{d\theta}\left(G_{elastic}+G_{electro}\right)-\frac{d}{dz}\left(\frac{d}{d\theta'}\left(G_{elastic}+G_{electro}\right)\right)=0 \qquad \text{Eq. 3.14}$$

The resulting expression from this is:

$$0=\underbrace{\left(K_{11}\cos^2\theta+K_{33}\sin^2\theta\right)\left(\frac{d\theta}{dz}\right)\left(\frac{d^2\theta}{dz^2}\right)-\frac{1}{2}\left(K_{33}-K_{11}\right)\sin 2\theta\left(\frac{d\theta}{dz}\right)^2}_{(i)}$$

$$+\underbrace{\frac{D_z{}^2\left(\varepsilon_{//}-\varepsilon_{\perp}\right)\sin 2\theta}{2\varepsilon_0\left(\varepsilon_{//}\sin^2\theta+\varepsilon_{\perp}\cos^2\theta\right)^2}}_{(ii)}-\underbrace{\frac{3\left(\varepsilon_{//}-\varepsilon_{\perp}\right)\left(e_1+e_3\right)^2\sin^3 2\theta\left(\frac{d\theta}{dz}\right)^2}{8\varepsilon_0\left(\varepsilon_{//}\sin^2\theta+\varepsilon_{\perp}\cos^2\theta\right)^2}}_{(iii)} \qquad \text{Eq. 3.15}$$

$$+\underbrace{\frac{3\left(e_1+e_3\right)^2\sin^2 2\theta}{4\varepsilon_0\left(\varepsilon_{//}\sin^2\theta+\varepsilon_{\perp}\cos^2\theta\right)}\left(\frac{d\theta}{dz}\right)\left(\frac{d^2\theta}{dz^2}\right)+\frac{3\left(e_1+e_3\right)^2\sin 4\theta}{4\varepsilon_0\left(\varepsilon_{//}\sin^2\theta+\varepsilon_{\perp}\cos^2\theta\right)}\left(\frac{d\theta}{dz}\right)^2}_{(iv)}$$

The electrostatic components in eq. 3.15 can be considered as the energy due to: (i) the elastic distortion; (ii) the dielectric anisotropy; (iii) the coupling between the applied field and the flexoelectric field and (iv) the interaction of the flexoelectric field with itself. This expression can be re-written in the following form:

$$0 = \frac{d}{dz}\left[\left(K_{11}\cos^2\theta + K_{33}\sin^2\theta\right)\left(\frac{d\theta}{dz}\right)^2 - \left(\frac{4D_z{}^2 + 3(e_1+e_3)^2\sin^2 2\theta\left(\frac{d\theta}{dz}\right)^2}{4\varepsilon_0\left(\varepsilon_{//}\sin^2\theta + \varepsilon_\perp\cos^2\theta\right)^2}\right)\right] \quad \text{Eq. 3.16}$$

and so it follows that the integral of eq. 3.16 must be equal to a constant, *C*. Rearranging this gives an expression for D_z as a function of θ and $\frac{d\theta}{dz}$:

$$D_z = \frac{d\theta}{dz}\left[\varepsilon_0\left(C + \left(K_{11}\cos^2\theta + K_{33}\sin^2\theta\right)\right)\left(\varepsilon_{//}\sin^2\theta + \varepsilon_\perp\cos^2\theta\right)^2 - 3(e_1+e_3)^2\sin^2\theta\cos^2\theta\right]^{1/2} \quad \text{Eq. 3.17}$$

Equation 3.8 can be rearranged to give an expression for the electric field in the cell, as a function of θ and $d\theta/dz$. The field $E_z(z)$ at each point in the cell is equal to the voltage gradient at that point, and as the liquid crystal cell itself is electrically neutral, the integral of the field between the two substrates must be equal to the applied external voltage, i.e.:

$$V = -\int_0^d E_z(z)dz = -\int_0^d \frac{2D_z - \sin 2\theta(e_1+e_3)\frac{d\theta}{dz}}{2\varepsilon_0\left(\varepsilon_{//}\sin^2\theta + \varepsilon_\perp\cos^2\theta\right)}dz \quad \text{Eq. 3.18}$$

Combining this with eq. 3.17 produces an expression that is a function of θ alone. Transforming the limits $z = 0$ and $z = d$ to the equivalent surface tilts $\theta = \theta_0$ and $\theta = \theta_d$, gives an equation that can be used to determine the unknown constant C:

$$V = -\int_{\theta_0}^{\theta_d} \frac{(e_{11}+e_{33})\sin 2\theta}{2\varepsilon_0\left(\varepsilon_{//}\sin^2\theta+\varepsilon_\perp\cos^2\theta\right)}d\theta - \int_{\theta_0}^{\theta_d}\left[\frac{\left(K_{11}\cos^2\theta+K_{33}\sin^2\theta\right)+\frac{(e_{11}+e_{33})^2\sin^2 2\theta}{4\varepsilon_0\left(\varepsilon_{//}\sin^2\theta+\varepsilon_\perp\cos^2\theta\right)}}{C\left[\varepsilon_0\left(\varepsilon_{//}\sin^2\theta+\varepsilon_\perp\cos^2\theta\right)+1\right]}\right]^{\frac{1}{2}}d\theta \quad \text{Eq. 3.19}$$

In the modelling program, an initial value for the constant C is guessed, and an iterative process is used to integrate $dV/d\theta$ with respect to θ between θ_0 and θ_d. The value of V calculated is compared with the actual external voltage applied to the cell. If the two values are not within a pre-defined error margin, the value of C is adjusted, the integration is repeated, and a new value of V is found. This process continues until the two values for the voltage agree.

Once C has been determined for that voltage, the tilt profile through the cell is calculated. The angle range between θ_0 and θ_d is divided up into equally spaced tilt angles. Eq. 3.17 can be used to give an expression for dz as a function of θ, and so the position Z of an angle Θ is given by:

$$\frac{\int_0^Z dz}{\int_0^d dz} = \frac{Z}{d} = \frac{\int_{\theta_0}^{\Theta} f(\theta)d\theta}{\int_{\theta_0}^{\theta_D} f(\theta)d\theta} \quad \text{Eq. 3.20}$$

Where:

$$f(\theta) = \sqrt{\frac{\varepsilon_e\sin^2\theta+\varepsilon_o\cos^2\theta}{\left(1+C\left(\varepsilon_e\sin^2\theta+\varepsilon_o\cos^2\theta\right)\right)}\left(\left(K_{11}\cos^2\theta+K_{33}\sin^2\theta\right)-\frac{3(e_{11}+e_{33})^2\sin^2 2\theta}{4\varepsilon_0\left(\varepsilon_e\sin^2\theta+\varepsilon_o\cos^2\theta\right)}\right)}$$

The integration is performed iteratively between θ_0 and Θ, resulting in a value for the position in the cell where Θ occurs. Using points through the cell equally spaced in the angle range θ_0 to θ_d, rather than equally spaced on the z-axis is particularly suited to HAN cell studies, as at high voltage, a substantial portion of the cell is at the same tilt angle. Therefore this process allows a greater sensitivity in the region where there is a sharp change in the director, whilst maintaining a minimal calculation time.

3.6.1 Applied AC Static Profiles

As discussed later in the dynamics section of this thesis, in the case where an AC field is applied to a HAN cell at a frequency >1kHz, the influence of the flexoelectric effect is negligible. This is due to the inability of the dipoles to respond rapidly enough to the constantly varying sign of the field. The flexoelectric constant is therefore effectively zero, and so by setting $(e_1+e_3)=0$, the high frequency AC case can be modelled, using the rms value of the voltage as the applied external voltage in the calculation.

3.6.2 Modelled Director Profiles

The flexoelectric modelling program uses the dielectric permittivities, splay and bend elastic constants, cell thickness, applied voltage and the sum of the splay and bend flexoelectric coefficients to calculate the static equilibrium director profile. It is apparent from eq. 3.9 that the flexoelectric component of the electrostatic free energy is dependent on the sign of both D_z and the director gradient. Therefore, for a given flexoelectric coefficient, the static profile will vary depending on whether the applied voltage is positive or negative. The polarity of the flexoelectric coefficient must also be taken into account, as these can also be defined as either positive or negative, and have been shown to change sign with a change in temperature (Rudquist, 1997). In comparison, the "pure" dielectric component is dependent on D_z^2, and hence sign independent,

Fig. 3.6 shows some examples of modelled director profiles for a 5μm HAN cell, using the standard physical parameters for E7. (K_{11} = 11.5pN, K_{33} = 17.9 pN, $\varepsilon_{//}$ = 19.1, $\varepsilon_{\perp}$ = 5.1 and $(e_{11}+e_{33}) = 1.5\times10^{-11}\mathrm{Cm}^{-1}$). The static director profiles have been modelled for 0V (cell shorted) and positive dc, negative dc and high frequency rms AC at voltages of 0.5V, 1V, 2V and 4V.

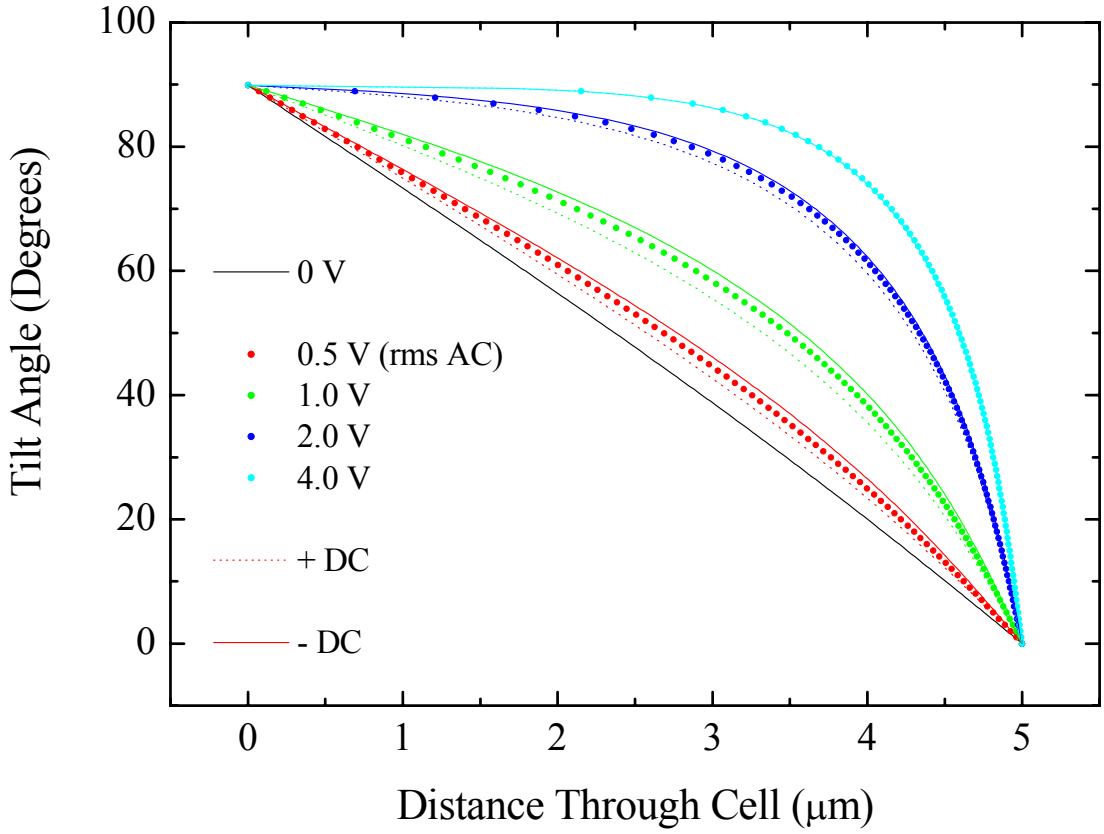

Fig. 3.6 **Modelled tilt profiles for a 5μm E7-filled HAN cell with positive DC, negative DC and 10kHz AC rms voltages applied.**

The influence of the magnitude of the sum of the splay and bend flexoelectric coefficients can be seen in fig. 3.7 (a). The elastic and dielectric anisotropy parameters for E7 have been used to model the tilt profiles for a 5μm HAN cell at 0V using flexoelectric coefficients of $(e_{11}+e_{33})$ = 0, 2×10^{-11}, 4×10^{-11}, 8×10^{-11}, 16×10^{-11} and 32×10^{-11} Cm^{-1}. To enable the distortions to be seen more clearly, in fig. 3.7 (b) the results have been plotted as the difference between the modelled tilt profile and a linear variation in tilt angle through the cell modelled as:

$$\theta_{linear} = 90° - \left(90° \times \frac{z(\mu m)}{5\mu m}\right) \qquad \text{Eq. 3.21}$$

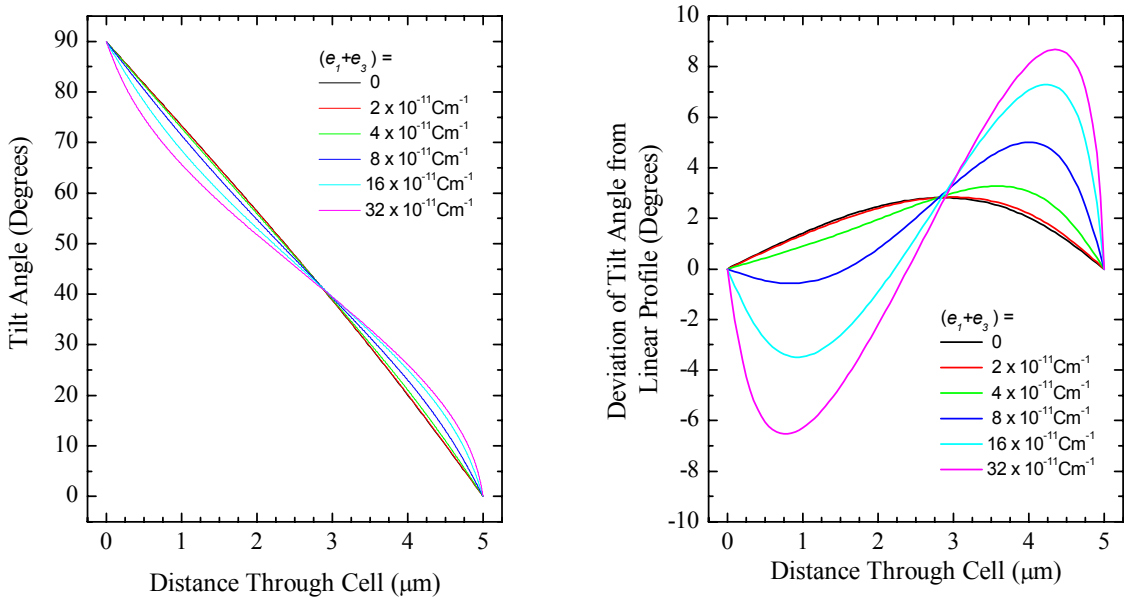

Fig. 3.7 Modelled tilt profiles at 0V for a range of values for the sum of the splay and bend flexoelectric coefficients plotted as (a) tilt angle and (b) deviation from a linear tilt profile (eq. 3.21), versus position through cell.

These plots indicate that the areas of maximum distortion occur close to the cell walls, which coincides with the regions of maximum splay and bend (see section 3.6.3). In practice, the magnitude of $(e_{11}+e_{33})$ for standard nematic liquid crystals developed for display applications is $\approx 2\times10^{-11}\mathrm{Cm}^{-1}$, although the synthesis of materials of higher flexoelectric constants is possible e.g. for use in fast-switching chiral devices (Musgrave et. al, 1999).

3.6.3 Modelled Field Distribution in a HAN Cell

For the non-twisted HAN cell geometry, the modulus of the splay distortion as a function of θ is given by:

$$|Splay| = |\mathbf{n}(\nabla \cdot \mathbf{n})| = \left|\cos^2\theta \frac{d\theta}{dz}\hat{\mathbf{x}} - \sin\theta\cos\theta\frac{d\theta}{dz}\hat{\mathbf{z}}\right| = \left|\cos^2\theta\frac{d\theta}{dz}\right| \qquad \text{Eq. 3.21}$$

Similarly, the modulus of the bend distortion is given by:

$$|Bend| = |\mathbf{n}\times(\nabla\times\mathbf{n})| = \left|\sin^2\theta \frac{d\theta}{dz}\hat{\mathbf{x}} - \sin\theta\cos\theta\frac{d\theta}{dz}\hat{\mathbf{z}}\right| = \left|\sin^2\theta\frac{d\theta}{dz}\right| \qquad \text{Eq. 3.22}$$

The modulus of the splay and bend deformations in a HAN cell at applied AC voltages of 0, 0.5, 1, and 2V rms (i.e. $(e_1 + e_3) = 0$) are shown in fig, 3.8.

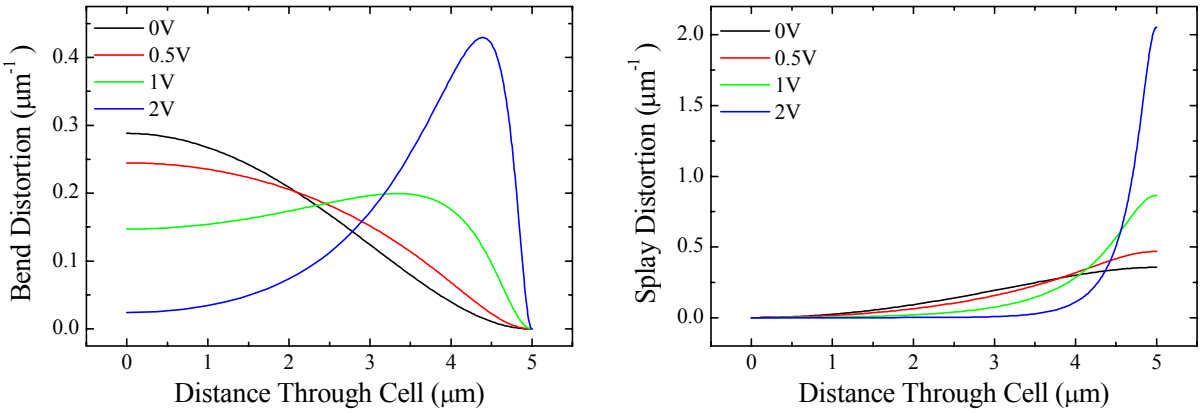

Fig. 3.8 Modelled magnitude of (a) splay and (b) bend distortion profiles in an E7 filled 5μm HAN cell with 10kHz rms AC voltages of 0, 0.5, 1 and 2V are applied.

These plots highlight the fact that at the homeotropic surface of the cell, the distortion is pure bend, and at the homogeneous surface, pure splay. From equation 3.18 it is clear that, due to the dielectric anisotropy of the liquid crystal and the dependence of the flexoelectric field on the splay and bend deformation of the director, the electric

field is non-uniform through a HAN cell. However, from Gauss' law, the integral of $E_z(z)$ between the two substrates must be equal to the applied voltage. (The influence of surface polarisation and free-ions within the cell has been assumed to be negligible).

The effect of the flexoelectric coefficients on the field profile within the cell is highlighted when eq. 3.18 is used to plot the field distribution through a 5μm E7 filled HAN cell with $(e_1 + e_3) = +1.5 \times 10^{-11}$ Cm^{-1} (fig. 3.9). At 0V, eq. 3.8 shows that if the flexoelectric coefficients are neglected, $D_z = 0$ and hence $E_z(z) = 0$ at all points through the cell. However, for a finite value of $(e_1 + e_3)$, D_z must also be finite, and $E_z(z)$ must vary as a function of θ. Integrating the field profile shown for the flexoelectric field in a HAN cell in fig. 3.9(a) confirms that the total voltage across the cell is equal to 0V.

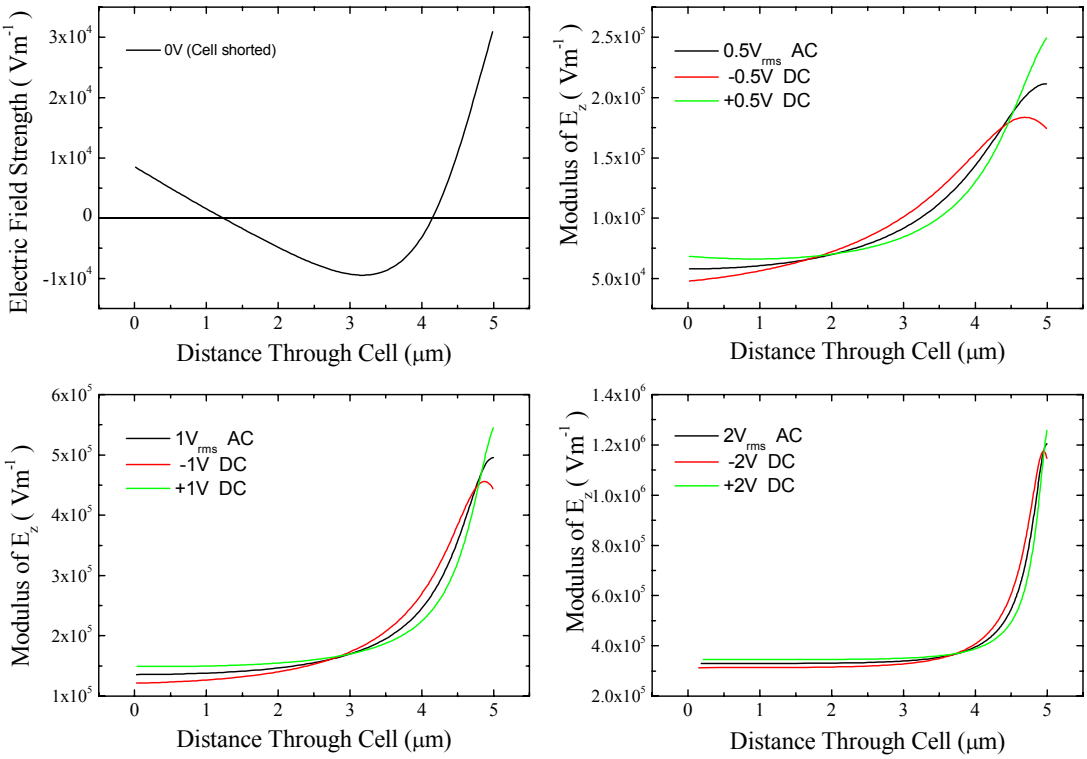

Fig. 3.9 **Modelled electric field profiles in an E7 filled HAN cell with positive and negative dc and 10kHz rms AC voltages of (a) 0V; (b) 0.5V; (c) 1.0V and (d) 2.0V**

When external voltages are applied to the cell, the distorted tilt profile results in a change in field distribution. Fig. 3.9 (b), (c) and (d) show the results of applying 0.5V,

1.0V and 2.0V respectively to the HAN cell in forward and reverse DC bias, as well as for a 10kHz AC voltage. As highlighted previously, the difference in director profile for forward and reverse bias DC results in field profiles for the opposite DC voltages differing not only in sign, but in the field profile as well. The result of this is that it is possible to generate relatively high, localised fields inside a HAN cell whilst applying low or even no external field to the cell.

3.7 Conclusion

The origin of flexoelectricity in liquid crystalline structures has been discussed qualitatively. Particular emphasis has been placed on the flexoelectric effect arising in a HAN cell, due to the high splay and bend distortion arising in the structure. The importance of this phenomena has been highlighted by introducing two device applications of the HAN cell structure, and the importance of the flexoelectric effect in their operation has been discussed.

A mathematical model has been developed which involves minimising the sum of the elastic, dielectric and flexoelectric free energies of a HAN cell using the Euler-Lagrange variational principle. The condition that the integral of the electric field within the cell must be equal to the external voltage applied perpendicular to the substrate, together with the fact that the displacement field perpendicular to the substrate is continuous has been used to determine the director profile within the cell, using an iterative computational technique. The program developed from this has then been used to model the director profiles for a HAN cell using a variety of flexoelectric constants. The electric field distribution in each case has also been modelled.

In the next chapter, this model is used to determine the flexoelectric constants of a liquid crystal by measuring the director profile at applied positive and negative DC fields, and comparing it to the free-energy minimisation model profiles generated.

Chapter 4

Measurement of (e_{11} + e_{33}) and Surface Polarisation in E7 filled HAN Cells

The fully-leaky guided-mode optical-waveguide technique has been used to characterise the tilt profiles in two E7-filled Hybrid-Aligned Nematic cells. A preliminary study was performed to assess the origin and influence of free ions in a HAN cell to prevent shielding of the internal fields in the cell. Rubbed polyimide was found to be a major source of ion contamination, and so the homogeneous alignment method chosen was SiOx evaporated at a 60° angle.

The director distortion was measured with AC and DC voltages applied perpendicular to the substrates. By comparing the tilt profiles with model profiles produced using a free-energy minimisation program, the sum of the splay and bend flexoelectric coefficients (e_{11}+e_{33}) of E7 at 20°C has been measured as $+1.5\pm0.2\times10^{-11}Cm^{-1}$. The effect of surface polarisation in the cells has also been observed. This surface polarisation is attributed to the influence of the homeotropic surface. The dipole alignment imbalance of the liquid crystal at the homeotropic surface has then been estimated.

4.1 Introduction

The flexoelectric effect in liquid crystal cells is analogous to the piezoelectric effect in solid-state physics. A distortion in the arrangement of the polar liquid crystal molecules e.g. by aligning them, can produce a net electric field across the cell, which in turn produces an electrostatic distortion in the director profile. The magnitude and sign of the field is determined by the flexoelectric constants of the material.

The Hybrid-Aligned Nematic (HAN) cell geometry is an ideal configuration for measuring the flexoelectric constant of a nematic liquid crystal. The director profile through the cell tilts through approximately 90° and has a high degree of bend and splay distortion. This produces a flexoelectric field within the cell, the size of which is dependent on the sum of the splay and bend flexoelectric coefficients (e_{11}+e_{33}). By applying DC voltages across the cell, the tilt profile and flexoelectric field can be altered. The polarity of the voltage is important as in one case the flexoelectric field reduces the applied field across the cell, and in the other it enhances it. If a high frequency (>1kHz) AC sinusoidal voltage is applied, the flexoelectric contribution is negligible due to its comparatively long response time, and only the dielectric and elastic distortion is observed.

A recent study (Mazulla et al., 2001) has proposed that surface polarisation on a silicon monoxide coated substrate influences the director profile in a HAN cell. We show here that it is necessary to include surface polarisation when modelling the response of a liquid crystal HAN cell to applied DC fields. The fully-leaky guided mode optical-waveguide technique has proved to be highly sensitive to subtle changes in the director profile under applied voltages and has therefore been used for this study

To enable the flexoelectric distortion to be measured accurately, it is important that the cell does not contain any free-ions which could cancel any distortion produced by the flexoelectric field. Therefore, prior to any measurements being taken, the samples under test must be checked to ensure that when a DC field is applied, they maintain the distortion due to the applied field over a timescale suitable for the collection of the optical data (≈500ms).

4.2 Sample Preparation

The presence of flexoelectric polarisation in a HAN cell causes a subtle change in the static director profile. By modelling the situation using a free energy minimisation program (chapter 3) it is clear that the most noticeable distortions to the director profile occur when low voltages (< 2V for a 5μm cell) are applied. In this situation it is imperative that the samples under test are free from any ionic contaminants which could potentially migrate through the cell, distorting the field distribution within the structure, and hence the response of the director itself.

The presence of any free ions can be readily observed using the static fully-leaky kit by mounting the cell between two low-index prisms and setting the rotating arrangement at an arbitrary angle of incidence. The optical response of the cell to an applied DC voltage can then be monitored by simply connecting the output of the photodiode detector to an oscilloscope. In the absence of free-ions, the cell should respond to the applied field, over a period of a few ms, and then remain at this level indefinitely. The output of the detector should therefore react in the same way. Conversely, if free ions are present in the cell, the director will still respond to the initial applied dc voltage, but whilst the applied voltage is maintained, the free ions in the material will diffuse through the cell, forming charge layers at the two surfaces and therefore reducing the DC voltage present.

An estimate for the timescale of this diffusion can be made by taking a typical drift mobility value for a positive ion in the liquid crystal layer as 3.5×10^{-10} $cm^2 V^{-1} s^{-1}$ (Murakami et al, 1995). By assuming a cell thickness of 3×10^{-6} m and an applied voltage of 1V, producing a uniform field, the time scale for the drift to occur is of the order of a few tens of milliseconds, which would be readily observed.

4.3 Sources of contamination

During sample preparation, there are three main areas where these impurities can enter the cell, and these will now be discussed in turn, along with the techniques used to minimise their effects.

4.3.1 Ionic impurities in the liquid crystal material

In each of the samples tested, the liquid crystalline material used was the Merck compound E7 (also known as BL001). This material was chosen as its physical parameters (elastic constants, dielectric permittivities and refractive indices) are well documented. The sample used was stored in a clean, dry environment to prevent contamination from the environment, and contact with other surfaces was minimised during the filling stage

4.3.2 Contamination during sealing

During the cell construction process, two types of glue are used to seal the cell. Initially, the cell is spaced by using spacer beads dispersed in a glue which sets when exposed to UV light. To prevent the generation of free ions in the aligning layers during the annealing process, the central area of the cell was masked with black card during the UV exposure.

The second glue used in the sample preparation procedure was an epoxy resin, used to seal the open edges of the cell after filling. In this case, the glue was allowed to set to a thickened consistency before its application to the cell edges, minimising the mobility of any material in the glue to prevent it leaking into the cell.

4.3.3 Homeotropic aligner

The homeotropic alignment used in the HAN cell construction is a monolayer of octadecyltrimethoxysilane. This organo-silane forms a strong, permanent bond with the ITO layer on the substrate, and any excess compound is removed prior to the cell assembly. The risk of free-ion contamination due to the OTMS is therefore minimal.

4.3.4 Rubbed polyimide alignment layer

Homogeneous alignment by rubbed polyimide has been found to be a major source of ion-contamination. In the substrate preparation process, a ≈30nm layer of polymer is spun down onto the ITO layer and then baked. This layer is then rubbed by

passing the layer under a rotating velvet-coated drum. It is believed that this "contact" method for producing the microgrooves required to induce the homogeneous alignment can result in ionic contamination in the cell in two ways.

Firstly, the static charging can arise due to the rubbing of the cloth across the polymer surface. This is unavoidable, although this factor is taken into account when the polymers are produced to reduce this method of contamination.

The second method of contamination can come from the transfer of ions from dirt and dust that may have become embedded in the rubbing cloth, as is believed to have happened in the case of an initial batch of cells produced for this study. To minimise contamination from the rubbing process, the influence of washing the polymer with either water or isopropanol was examined, but this was found to have negligible effects.

The result of mounting the cell between the prisms and monitoring the output of the photodiode detector, as described above, is shown in Fig. 4.1(a). The image is of the oscilloscope trace showing the output of the transmission detector when a pulsed DC voltage of ±1V is applied to a 3μm HAN cell. The cell is fixed at a 60° angle of incidence, and the form of the pulse is shown in fig. 4.1(b).

The pulsed DC field is used to prevent electrolytic decomposition of the liquid crystal material, and the pulse duration is of several tens of ms. This is far higher than the timescale over which backflow occurs, which is the region of a few milliseconds after a change in voltage (see chapters 7 and 8). A difference in levels of the optical intensity are expected due to the difference in director profile at these two applied voltages. However, it is clear to see that after the initial negative voltage is applied, the output from the transmission detector reaches a peak after around 15ms, and then begins to decline.

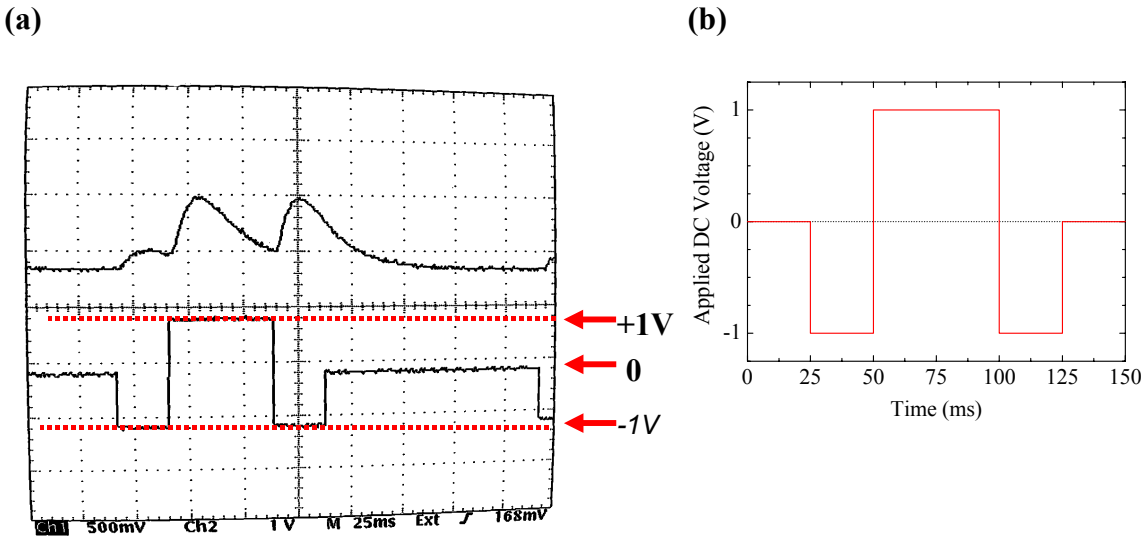

Fig. 4.1 **(a) Image of the oscilloscope trace showing the output of the transmission detector (upper trace) when a pulsed DC voltage of ±1V (lower trace) is applied across the asymmetric HAN cell at a 60° angle of incidence and a 45° azimuthal angle. The decay of intensity due to ion drift can be clearly seen; (b) Pulsed DC voltage waveform applied to the HAN cell during ion-drift observations.**

The application of a subsequent positive pulse drives the output voltage up to a new peak, which then drops steadily over the following 50ms. This suggests that during this time, free ions are migrating through the cell, cancelling the applied DC field and creating an effective internal voltage of -ΔV, counteracting the applied voltage of +1V. The timescale for this change in intensity is consistent with ionic drift through the cell.

Finally, the application of a second negative pulse causes the optical intensity to rise rapidly, overshooting the original –1V intensity over a time scale which is again greater than the backflow regime. This implies that the field at the point of switching is greater than the applied –1V, which could be accounted for by the presence of the internal offset field of -ΔV set up by the free ions during the preceding positive pulse. Again, there is a steady decrease in intensity after the peak has been reached and this continues smoothly when the voltage is removed, until the 0V intensity level is again reached.

4.3.5 Silicon Oxide alignment layer

An alternative method of producing homogeneous alignment is the deposition of silicon oxide at an angle of 60°, as discussed in chapter 1. In this situation no physical contact is made with the substrate, minimising the risk of contamination by ionic material. The silicon monoxide itself is non-ionic and once evaporated onto the substrate forms a stable layer which will not dissolve into the liquid crystal material.

Construction of a HAN cell using this as the homogeneous aligner was found to produce a cell which gave a stable output from the transmission detector (fig. 4.2(a)) when the same DC pulse sequence as before was applied (fig. 4.2(b)). After an initial few milliseconds where the director is responding to the change in the applied voltage, the optical intensity trace remains at a constant level. This therefore suggests that the cell was free of mobile-ions. The SiO_x alignment was chosen as the most suitable substrate treatment for the study of the flexoelectric effect, and the oscilloscope trace suggests that the optical intensity versus angle of incidence data at each point should be taken at least 20ms after the pulse has been applied.

(a) **(b)**

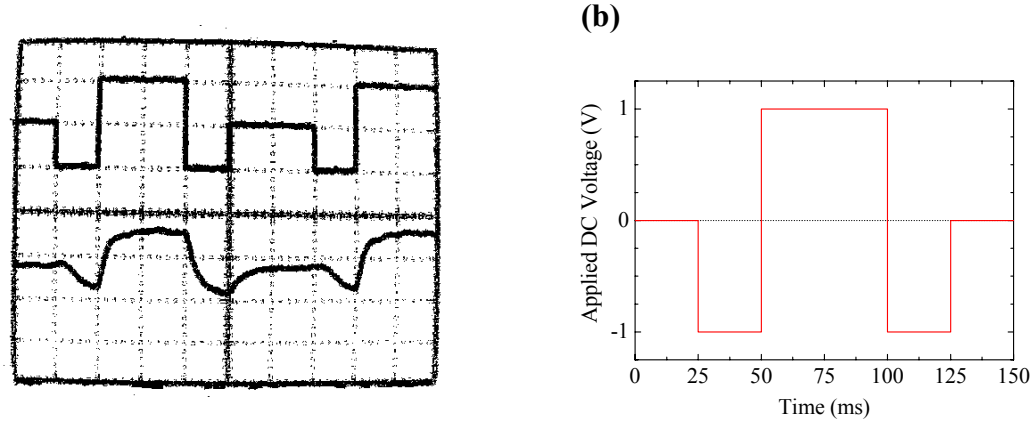

Fig. 4.2 **(a) Image of the oscilloscope trace showing the output of the transmission detector (upper trace) when a pulsed DC voltage of ±1V (lower trace) is applied across the asymmetric HAN cell at a 60° angle of incidence and a 45° azimuthal angle. The intensity of the output of the detector reaches a stable state after an initial dynamic response due to a change in voltage; (b) The pulsed DC voltage waveform applied to the HAN cell during ion-drift observations.**

4.4 Static Director Profile Measurement – Experimental Procedure

Two HAN cells containing E7 (Merck BL001) were constructed for this study. Both cells used ITO-coated low-index (n = 1.52) glass substrates and were spaced using 3μm beads dispersed in UV-setting glue along two edges of the cell. For the first cell ≈ 31 nm SiO_x was evaporated onto one ITO surface at a 60° angle to produce homogeneous alignment. A monolayer treatment of octadecyltrimethoxysilane (OTMS) was applied directly onto the ITO surface of the opposite substrate to produce homeotropic alignment. This cell is referred to as the asymmetric HAN cell (fig. 4.3(a)). For the second cell, a similar thickness of SiO_x was again deposited at 60° onto the upper ITO substrate to produce homogeneous alignment, but it was also deposited onto the lower substrate before treating it with OTMS as before. This arrangement is referred to as the symmetric cell (figure 4.3(b)).

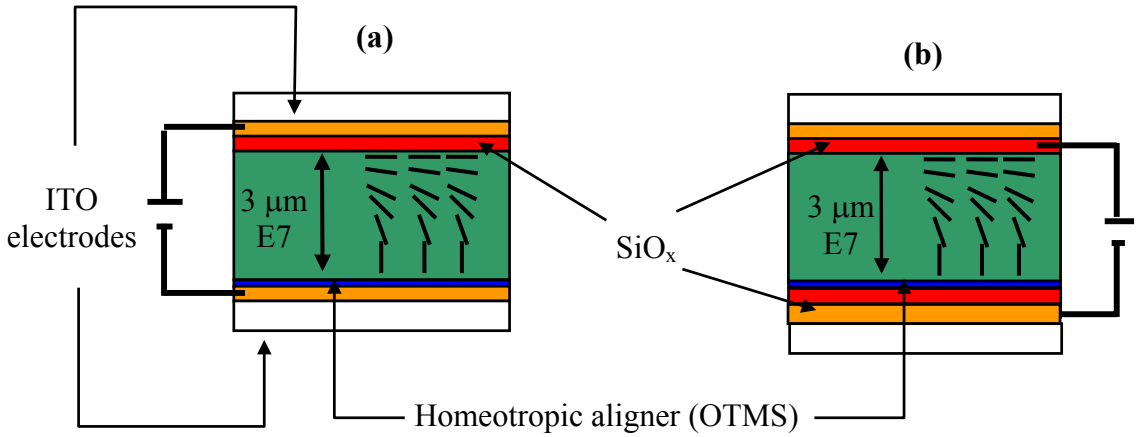

Fig. 4.3 Schematic diagram of a HAN cell with (a) asymmetric SiO_x geometry and (b) symmetric SiO_x geometry.

The fully-leaky guided mode geometry used for this investigation is discussed in chapter 2, with the same experimental method being used for both cells. The cell under investigation was index-matched at a 45° azimuthal angle between two low-index (n = 1.52) prisms with the homogeneous-aligned surface as the incident face. The cell was first shorted, and optical intensity vs. angle-of-incidence data was collected for transmitted and reflected polarisation conserving and converting beams. The scan was then repeated with 10kHz rms AC voltages of 0.5V, 1.0V and 1.5V applied across the

cell, perpendicular to the substrates. These measurements were then repeated with DC fields of ±0.5V, ±1.0V and ±1.5V. To prevent electrolytic decomposition of the liquid crystal and to minimise any effect of ion flow, a pulsed DC method was used (fig. 4.4). At each angle of incidence, the optical intensity was collected 200ms after the start of the pulse to allow the director to reach equilibrium following the initial dynamic response of the cell.

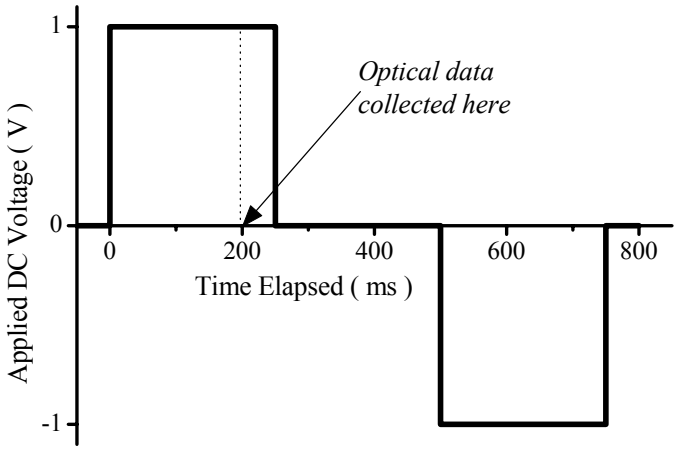

Fig. 4.4 **Diagram of the applied DC pulse and synchronised data-collection point for forward and reverse bias DC measurements.**

The optical data collected for each voltage was compared to model data produced by a multi-layer optics modelling routine. The optical parameters (optical permittivity, absorption and thickness) of the ITO, SiO_x and liquid crystal layers, and the director profile through the cell were used as fitting parameters. (The OTMS layer was not included in the model as it was only one monolayer thick and did not contribute to the optical properties of the cell.) All 8 data-sets (polarisation conserving and converting for reflectivity and transmission of p- and s- polarised light) were fitted simultaneously for each voltage to remove any degeneracy in the director profile which fits the results.

In order to obtain the physical constants of the liquid crystal material, the measured tilt profiles were compared to model tilt profiles produced using the free-energy minimisation routine introduced in chapter 3. In the AC case, the rms applied voltage, ordinary and extra-ordinary permittivities and splay and bend elastic constants

of E7 were used as variables. In the DC case these parameters plus the sum of the splay and bend flexoelectric constants (e_{11}+e_{33}) were used in the model.

4.5 Results and discussion

The optical intensity vs. angle-of-incidence data for both the symmetric and asymmetric cells are shown in fig. 4.5, along with the model data fit produced by the multi-layer optics-modelling program. For all voltages, the director profile through the cell was modelled as a third-order rational bezier function, and the twist was held at a constant value. The optical parameters for the layers used in the cell are shown in table 4.1 .

Optical Layer	ε_r	ε_i	Thickness (nm)
ITO	3.46 ± 0.01	0.068 ± 0.008	32 ± 2
SiO_x (upper)	2.41 ± 0.01	0.021 ± 0.005	31 ± 2
E7 ($\varepsilon_\perp$)	2.311 ± 0.002	$0.4 \pm 0.2\times10^{-5}$	
E7 ($\varepsilon_{\parallel}$)	3.014 ± 0.006	0.004 ± 0.002	
SiO_x (lower)	2.41 ± 0.01	0.021 ± 0.005	36 ± 2

Table 4.1 Summary of the optical parameters of the liquid crystal cells. The values were obtained from the multi-layer optics modelling program.

The tilt profiles (tilt angles versus distance through the cell) produced for the forward and reverse bias cases are shown in fig.4.6.

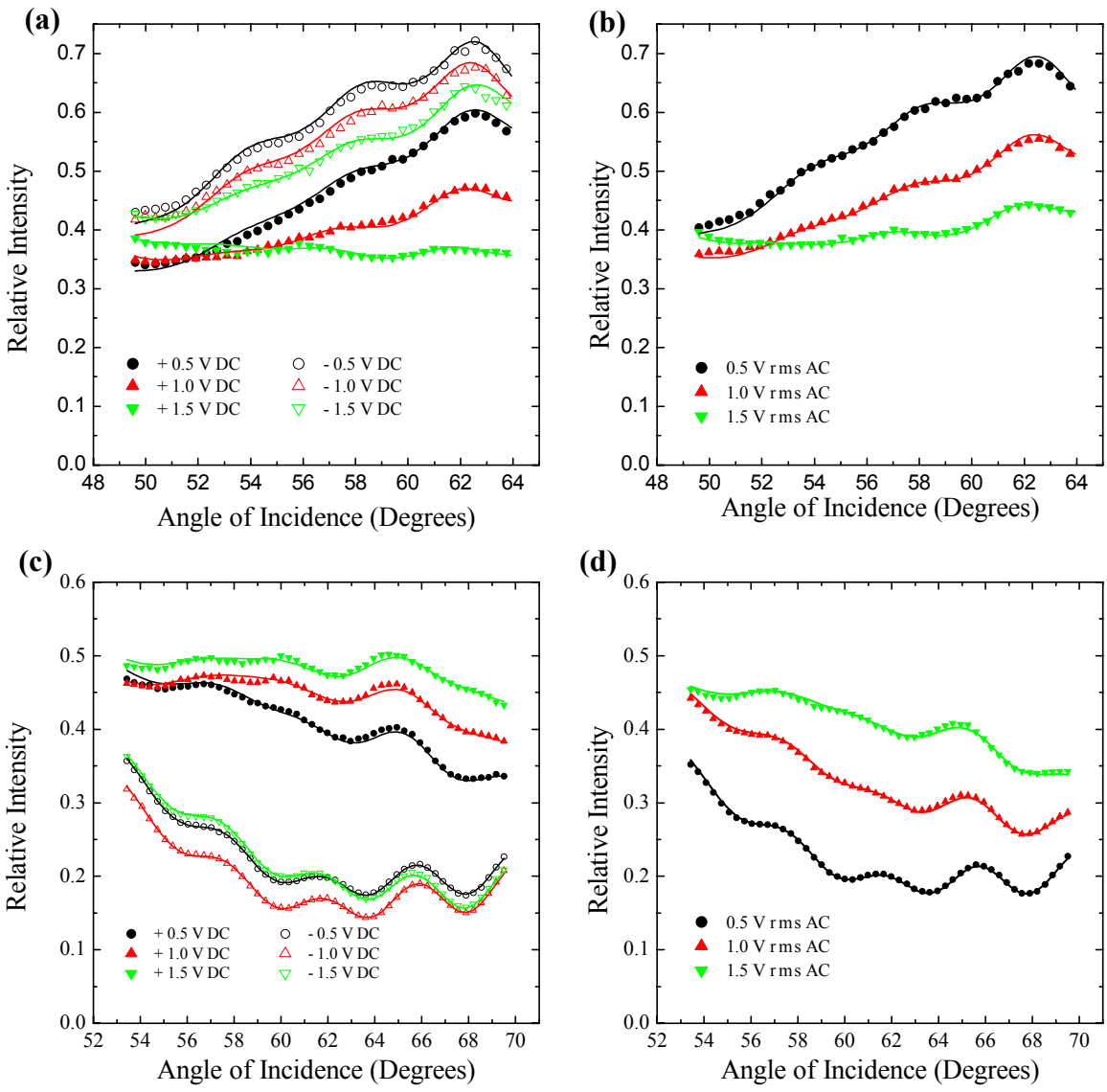

Fig. 4.5 **Comparison between measured and model optical relative-intensity (normalised to input of 1) vs. angle-of-incidence data. Transmitted p-polarised conserving signal with (a) Applied DC voltage, and (b) Applied rms AC voltage, in an asymmetric SiO_x cell; Transmitted s-p polarisation converting signal with (c) Applied DC voltage, and (d) applied rms AC voltage, in the symmetric cell.**

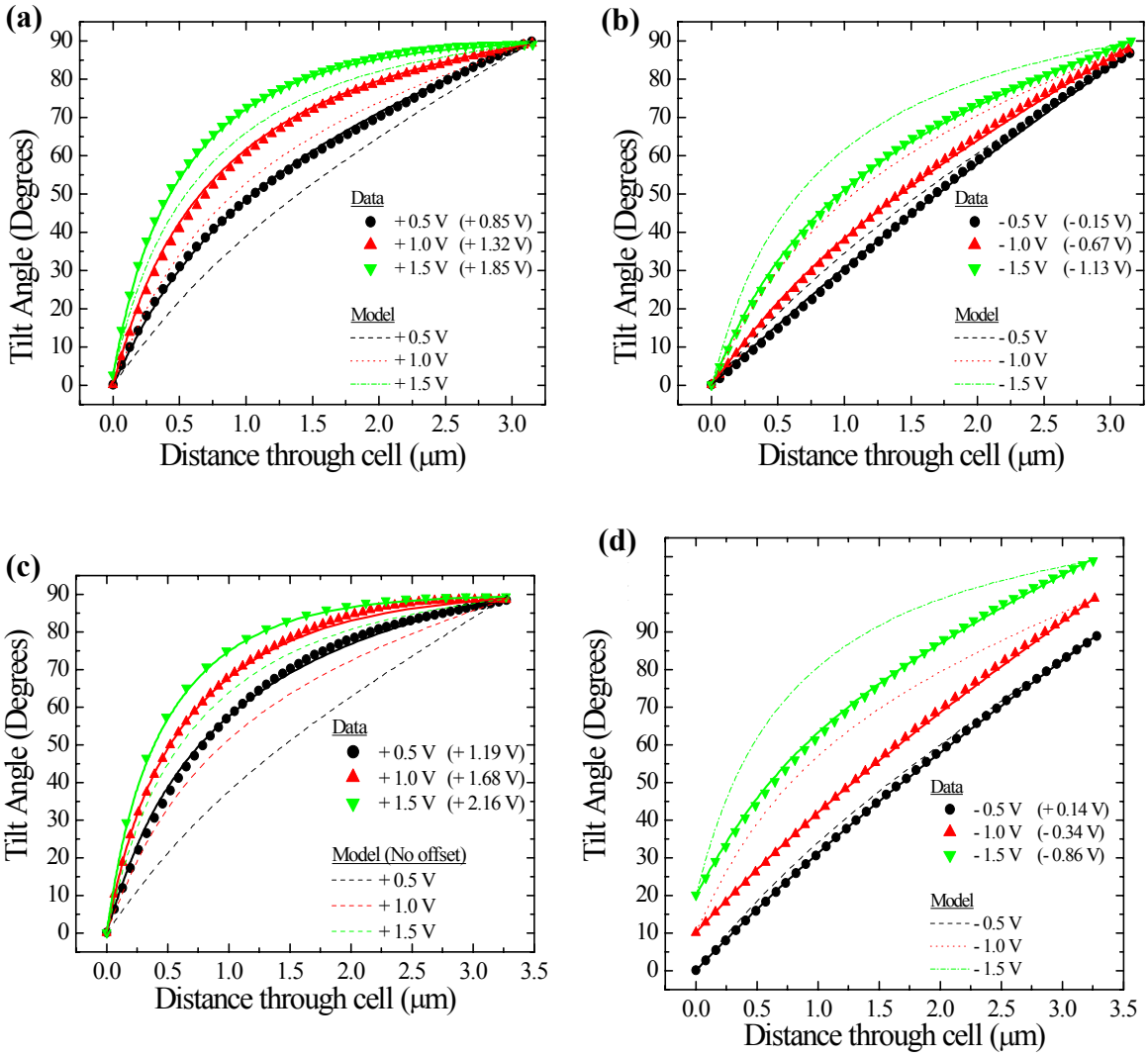

Fig. 4.6 Measured tilt profiles (symbols), modelled tilt profiles (broken lines) and fitted tilt profiles (solid lines) for ((a) and (b)) symmetric SiO_x cell and ((c) and (d)) asymmetric SiO_x cell. For clarity in (d) the data-set at 1.0V is shifted by 10° and that at 1.5V, by 20°. The actual applied DC voltages required to fit the tilt profiles are shown in brackets.

4.5.1 Applied DC voltage analysis

For both cell structures, no agreement between measured and modelled applied DC tilt profiles could be found by simply holding the elastic and dielectric constants at values within reasonable bounds of those specified in the Merck data-sheet for E7 (K_{11} = 11.5pN, K_{33} = 18.5pN, ε_e = 19.0 and ε_o = 5.2), and then varying the flexoelectric coefficient. In all cases, when the flexoelectric coefficient was increased above

5×10^{-11}Cm^{-1}, the form of the model tilt profile distorted into an "s-bend" type shape. However, good agreement could be found by increasing the forward bias voltage in the model and reducing the reverse bias voltage by the same amount. It was therefore concluded that there is an additional distortion due to the presence of a permanent internal DC bias in the cell. For the asymmetric cell, the offset bias was found to be +0.66±0.02V (taking the homeotropic substrate as the positive plate) and for the symmetric cell, +0.34±0.01V. For both cases, a good fit was obtained by including a flexoelectric coefficient of $+1.5\pm0.2\times10^{-11}$ Cm^{-1}. This is in agreement with values published for similar materials (Mazulla et al, 2002; Blinov et al, 1999).

4.5.2 Applied AC voltage analysis

For the applied AC rms voltages, the measured tilt profiles showed a higher distortion than the model predicted. The voltage increase required to fit the model to the data was always ≈ 0.1V but varied with the AC voltage applied. This is consistent with a sinusoidal voltage of amplitude A and rms value V being shifted by a DC bias of V_0. The new rms voltage across the cell, V', is given by:

$$V' = \left[\left\langle \left(V_0 + A\sin(\omega t)\right)^2 \right\rangle\right]^{\frac{1}{2}} = \left(V_0^{\,2} + \frac{A^2}{2}\right)^{\frac{1}{2}} = \left(V_0^{\,2} + V^2\right)^{\frac{1}{2}} \qquad \text{Eq. 4.1}$$

A comparison between the AC rms voltages required in the free energy minimisation model to fit to the AC tilt profiles and the "corrected" applied AC voltage when the DC offset is taken into account are shown in table 4.2. For the symmetric SiO_x cell where the DC offset voltage is lower, there is excellent agreement between the two values. However, for the asymmetric cell, where the DC offset is higher, there is very poor agreement for the lower voltages. This is most likely due to the shifted sinusoidal model being too simple. The presence of the permanent DC bias will produce a flexoelectric contribution, even with applied AC voltages. For the lower DC offset this appears to be negligible, but for the asymmetric case where the amplitude of the applied AC voltage is comparable to the DC offset it has a noticeable effect. A more complex free-energy model is required for this situation.

Applied rms AC	Measured V_{rms} (from tilt profile)	Predicted V_{rms} with DC offset
Symmetric cell (DC offset = 0.34 ± 0.01 V)		
0.50 V	0.61 ± 0.01V	0.60 ± 0.01V
1.00 V	1.06 ± 0.01V	1.06 ± 0.01V
1.50 V	1.54 ± 0.01V	1.54 ± 0.01V
Asymmetric cell (DC offset = 0.66 ± 0.02 V)		
0.50 V	0.62 ± 0.01V	0.82 ± 0.02 V
1.00 V	1.12 ± 0.01V	1.19 ± 0.02 V
1.50 V	1.63 ± 0.01V	1.64 ± 0.01 V

Table 4.2 Comparison between applied, measured and predicted AC rms voltages for the symmetric and asymmetric HAN cells.

4.6 Calculation of surface charge

Although the offset voltages in the two cell structures differ, they are both of the same polarity and similar magnitude. It can therefore be concluded that the source of the offset is not due to the presence of charges at the SiO_x surface, as in this situation the presence of the two SiO_x layers in the symmetric sample would cancel out any DC contribution. The DC bias must then be attributed to polarisation at the homeotropic surface. The homeotropic dipole moment of OTMS (Sugimura, 2001) is 1.43×10^{-30} Cm and this is far too small to produce a DC offset having the values measured. However, if the actual alignment at the substrate results in a preferential orientation of the dipoles of the liquid crystal molecules this would result in a permanent DC bias voltage in the cell.

The ratio of molecules aligned in the two possible directions required to produced the measured offsets can be calculated approximately using the physical parameters of a 5CB molecule as this is the main constituent of the compound E7. The

surface polarisation, P_s, produced by a layer of molecules with molecular moment μ and surface density N_0 is given by:

$$\mathbf{P}_s = \mu N_0 \Delta \mathbf{n} \qquad \text{Eq 4.2}$$

where $\Delta = n_+ - n_-$, is the difference between the fraction of molecules orientated in the two possible homeotropic alignments. If the molecules are approximated as being perfectly homeotropically aligned (i.e. order parameter = 1 and $\theta = 0°$ at the surface), equation 4.2 can be written as:

$$\Delta = \frac{P_s}{\mu N_0} \qquad \text{Eq 4.3}$$

and the offset voltage, V_0, can be defined as:

$$V_0 = \frac{P_s}{\varepsilon_0 \varepsilon_{//}} \qquad \text{Eq 4.4}$$

N_0 can be approximated as the reciprocal of the ordinary cross sectional area of the molecule, (radius of r_o), and so by combining equations 4.3 and 4.4,

$$\Delta = \frac{V_0 \varepsilon_0 \varepsilon_{//} \pi r_o^{\,2}}{\mu} \qquad \text{Eq 4.5}$$

As $n_+ + n_- = 1$, the fraction of molecules orientated one way is given by:

$$n_+ = \frac{1+\Delta}{2} = \frac{\mu + V_0 \varepsilon_0 \varepsilon_{//} \pi r_o^{\,2}}{2\mu} \qquad \text{Eq 4.6}$$

With the physical constants for 5CB (Kuhnau, 1999; Adam, 1997), $\mu = 21.6\times10^{-30}$ Cm, $r_o \approx 2\times10^{-10}$m and $\varepsilon_{//} = 1.69\times10^{-10}$Fm^{-1}, for the symmetric case (V_0 = 0.34V), we find n_+ = 67% and for the asymmetric case (V_0 = 0.66V), n_+ = 82%.

In both these estimates, the results suggest a preferential orientation for the molecules at the octadecyltrimethoxysilane surface. As little is known about the surface

chemistry and alignment mechanism of this particular treatment, it is difficult to determine whether this preference is due to ionic or chemical interactions at the surface. The influence of the ITO and SiO_x layers on the coverage of the OTMS, and hence the effectiveness of the homeotropic treatment, is likely to have an effect. The ITO surface should be significantly more uniform than the SiO_x layer which, when un-treated, produces homogeneous alignment. It can also be seen from the tilt profile measurements that in the asymmetric case, the alignment is more homeotropic at 0V (0.6°) than in the symmetric case (2.2°).

4.7 Conclusions

This study has suggested that surface polarisation influences the distortion produced when a DC voltage is applied to a HAN cell. This proposed DC offset bias in two different HAN cells has been evaluated and the source of this polarisation is thought to be the alignment at the homeotropic surface. The magnitude of the polarisation is consistent with an imbalance of as much as 82:18 in the alignment of the dipolar molecules at the homeotropic surface. The influence of this DC offset field on the director when a 10kHz AC rms voltage is applied has been observed. Approximate agreement is found with a simple model of this situation. The flexoelectric coefficient of E7 has also been measured as $+1.5 \pm 0.2\times10^{-11}$ Cm^{-1}, agreeing well with the values documented for similar materials.

Chapter 5

Polarimetry Measurements of Static Tilt Profiles in a ZLI-4788 Filled HAN Cell

5.1 Introduction

Polarimetry (also known as ellipsometry) is defined as "*the measurement of the state of polarisation of a polarised vector wave*" (Azzam and Bashara, 1997). A wealth of information about the optical properties and thickness of thin films can be obtained by measuring the effect that interaction with the surface has on the polarisation state of the electromagnetic wave. For this reason, optical polarimetry measurements of thin films have been used for many years to study processes ranging from the growth of thin oxide films, to the adsorption of gases onto surfaces. The study of liquid crystal cells is therefore ideally suited to polarimetric measurements as the information contained in the change of the polarisation state of light resulting from transmission through a liquid crystal cell allows the director structure in the cell to be determined.

In this study the director structure in a HAN cell mounted in a fully-leaky type cell-and-prism geometry has been studied by measuring the Stokes' parameters of transmitted light as a function of angle-of-incidence. The liquid crystal used in the cell is ZLI-4788 (Merck) which is a nematic material with negative dielectric anisotropy. Recently, there has been increasing commercial interest in these negative materials, and they have been demonstrated as highly suitable for use in commercial displays, such as

in the production of a bistable liquid crystal display aligned by an array of microscopic posts (Kitson and Geisow, 2002).

By measuring the director profile in a liquid crystal cell with various high frequency AC voltages applied, the elastic constants and dielectric permittivities of the material have been determined, and the anchoring energy at the liquid crystal/ homogeneous aligning layer interface has been calculated. This information is of particular interest commercially as it allows the suitability of the surface treatment used to be assessed.

5.2 The Stokes' Parameters

The Stokes' parameters are used to describe the polarisation state of elliptically polarised light. The advantage of using the Stokes description is that the parameters are functions only of the intensity and phase of an electromagnetic wave – physical properties which can be measured relatively easily. Four parameters are required in total, one to describe the total intensity (S_0) and three to describe the polarisation states (S_1 , S_2 , and S_3).

A full mathematical derivation of these parameters is given by Huard (1997). However, a more physical description of the nature of these parameters is given by Hecht (1987), and it is this explanation that is followed here.

The theory behind the Stokes' parameters can be illustrated by independently considering the transmission of elliptically polarized light through four different filters. Each filter is considered to transmit half of the incident light when illuminated with unpolarised light. The first filter is isotropic, and lets through all polarisations, and the transmitted intensity is I_0. The second and third filters are linear polarisers, one with the transmission axis horizontal, and the other with the transmission axis at 45° to the horizontal. The intensity in these two cases are I_1 and I_2. Finally, the fourth filter considered is a circular polariser which transmits only left-handed circularly polarised light, and the transmitted intensity is I_3.

The Stokes' parameters are defined by the following relations between the four intensities discussed:

$$S_0 = 2I_0 \quad \text{Eq. 5.1}$$

$$S_1 = 2I_1 - 2I_0 \quad \text{Eq. 5.2}$$

$$S_2 = 2I_2 - 2I_0 \quad \text{Eq. 5.3}$$

$$S_3 = 2I_3 - 2I_0 \quad \text{Eq. 5.4}$$

Rewriting these expressions in terms of the electric field vectors:

$$\mathbf{E}_{\mathbf{x}}(t) = \hat{\mathbf{x}} E_{0x}(t)\cos\left[(kz - \omega t) + \phi_x(t)\right] \quad \text{Eq. 5.5}$$

and

$$\mathbf{E}_{y}(t) = \hat{\mathbf{y}} E_{0y}(t)\cos\left[(kz - \omega t) + \phi_y(t)\right] \quad \text{Eq. 5.6}$$

where

$$\mathbf{E}(t) = \mathbf{E}_{\mathbf{x}}(t) + \mathbf{E}_{y}(t) \quad \text{Eq. 5.7}$$

and the phase difference, ϕ given by:

$$\phi = \phi_{\mathbf{x}} - \phi_y \quad \text{Eq. 5.8}$$

gives the Stokes' parameters as:

$$S_0 = \left\langle E_{0x}^2 \right\rangle + \left\langle E_{0y}^2 \right\rangle \quad \text{Eq. 5.9}$$

$$S_1 = \left\langle E_{0x}^2 \right\rangle - \left\langle E_{0y}^2 \right\rangle \quad \text{Eq. 5.10}$$

$$S_2 = \left\langle 2E_{0x}E_{0y}\cos\phi \right\rangle \quad \text{Eq. 5.11}$$

$$S_3 = \left\langle 2E_{0x}E_{0y}\sin\phi \right\rangle \quad \text{Eq. 5.12}$$

It is common to normalise these coefficients further by dividing each of them by S_0, equivalent to assuming an incident intensity of 1. Qualitative analysis of the parameters then shows that S_0 is simply the total (unit) incident intensity. S_1 is a measure of the degree of horizontal polarisation, with $S_1 = +1$ being totally *s*-polarised

(in this case, *s*-polarised is defined arbitrarily as horizontal relative to the plane of incidence), $S_1 = -1$ being totally *p*-polarised (i.e. vertically polarised) and $S_1 = 0$ being a polarisation at 45°. Similarly, S_2 is a measure of the degree to which the light is polarised at a 45° angle to the two axes, with $S_2 = +1$ corresponding to +45° and $S_2 = -1$ corresponding to -45°. Finally, S_3 is a measure of whether the beam is circularly polarised in the right-handed direction ($S_3 = +1$), the left-handed direction ($S_3 = -1$) or neither ($S_3 = 0$). In the case of *elliptically* polarised light, one or more of these four parameters will have a non-integer value between –1 and +1, depending on the ellipticity present. The polarisation state of the light can therefore be completely described by quantifying S_0, S_1, S_2 and S_3.

A waveguide technique analogous to the fully-leaky guided-mode technique can be used to determine the director profile in a liquid crystal cell. This involves measuring the Stokes' parameters of polarised light transmitted through a cell (index-matched between two hemi-cylinders) as a function of angle-of-incidence. The four parameters can be easily measured by using a polarimeter. (In contrast, the standard fully-leaky guided mode technique used in all the other experiments discussed in this thesis measures the absolute intensity for incident and transmitted *p*- and *s*-polarised light.)

Modelling the influence of the optical properties of the liquid crystal (and hence the director profile) on the Stokes' parameters of the transmitted light as a function of angle-of-incidence allows the director profile to be determined from the data collected. As in the fully-leaky guided-mode case, the modelling is produced by a multi-layer optics model, incorporating the optical parameters of both the isotropic and liquid crystal layers.

5.3 Experiment

A HAN cell spaced with 5μm beads and filled with the nematic liquid crystal ZLI-4788 (having negative dielectric anisotropy), was constructed from two ITO-coated glass substrates (fig. 5.1). Homeotropic alignment was produced by a 32nm layer of homeotropic aligning polymer (Nissan 1215) spun onto the ITO surface and then baked. Homogeneous alignment was produced by spinning down a 73nm layer of homogeneous-alignment inducing polymer (JSR AL-1254) onto the other ITO surface which was then baked and rubbed using a rubbing machine. The cell was filled and sealed and wires were attached to the electrodes using indium solder.

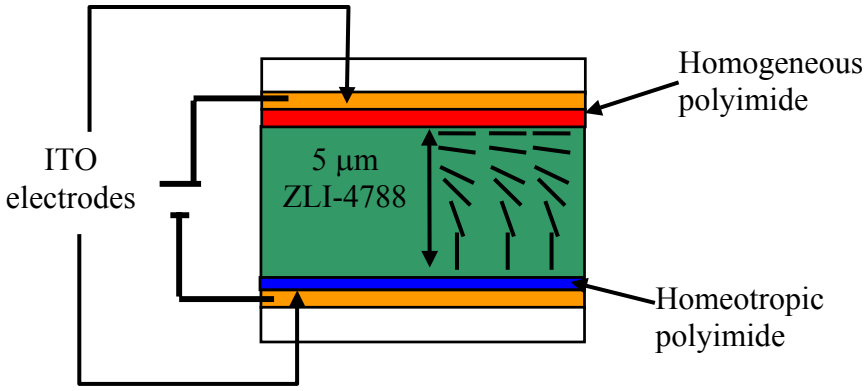

Fig. 5.1 Schematic diagram of the ZLI-4788 filled HAN cell used in this polarimetry study.

The experimental arrangement used to collect the Stokes' parameters data from the cell is shown in fig. 5.2. Light of wavelength 632.8nm from a 0.5mW He-Ne laser was passed through a polariser to select the required input polarisation angle, and then through a half-wave plate to produce circularly polarised light to ensure that the maximum intensity of the light was the same for all polarimeter readings. The cell under test was index-matched at a 0° azimuthal angle between two hemi-cylinders of refractive index n = 1.52, equal to that of the glass substrates of the cell. Due to slight lensing effects of the hemi-cylinders, an aperture was required to collimate the beam, which then entered the polarimeter.

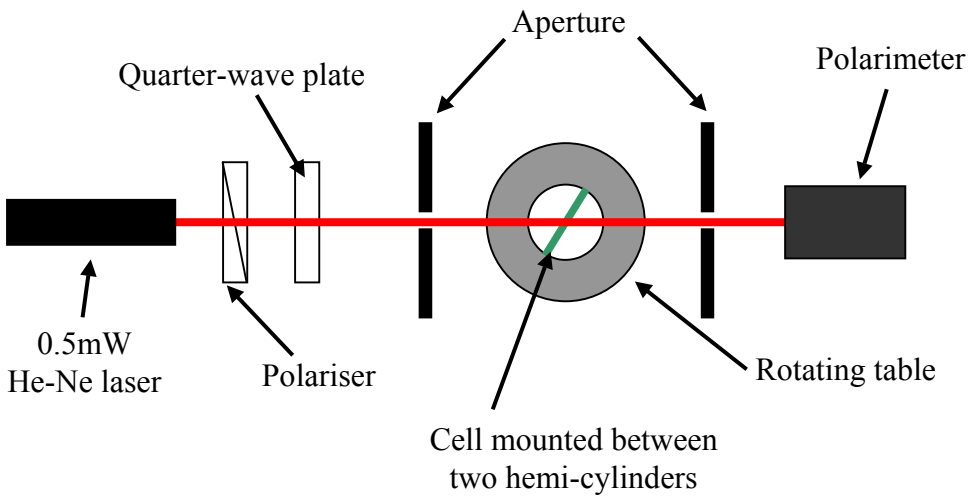

Fig. 5.2 Schematic diagram to show the layout of the equipment used to collect the Stokes' parameter data from a HAN cell.

The polarimeter used was a ThorLabs rotating quarter-wave plate polarimeter. Light entering the device passes through the quarter-wave plate (which rotates at a frequency of 10Hz) and then through a stationary polariser. A photodector then records the intensity of the transmitted light, which is modulated at a frequency which is a multiple of the rotational frequency of the quarter-wave plate. The use of an electronic device to analyse the harmonics of the light intensity signal recorded allows the Stokes' parameters to be determined (Dlugunovich et al, 2001). (It should be noted that due to the very low rotational frequency of the quarter-wave plate, this technique is only suitable for studying static director profiles.)

To collect the data, an automated system was used where the cell was set to an initial angle-of-incidence of 35°, measured from the normal to the cell substrate. The input polariser was set to the first required input polarisation angle of 45°, and the Stokes' parameters (S_1, S_2 and S_3) and the intensity of the light were recorded over a 35° range of angles-of-incidence in steps of 0.35°. The input polarisation angle was then changed to 135°, and the scan was repeated. These scans were then repeated with AC 10kHz AC voltages from 0.25V rms to 4V rms applied across the cell, in 0.25V steps.

5.4 Results

A selection of the fitted Stokes' parameters versus angle-of-incidence data collected is shown in fig. 5.3. For each voltage the S_1, S_2 and S_3 data for both input polarisations was fitted to simultaneously using the multi-layer optics model. In each case, the real and imaginary refractive indices and thickness of the isotropic and liquid crystal layers were used as fitting parameters, along with the director profile.

In the fitting routine, the tilt angle, $\theta(z)$ at a distance z through the cell of thickness d was modelled using a mathematical function. In the case of the 0V and 0.5V data, a third-order polynomial (eq. 5.13) was chosen, as the tilt profiles were close to linear. The coefficients B_0, B_1, B_2 and B_3 were used as fitting parameters.

$$\theta(z) = B_0 + B_1 \frac{z}{d} + B_2 \left(\frac{z}{d}\right)^2 + B_3 \left(\frac{z}{d}\right)^3 \qquad \text{Eq. 5.13}$$

For voltages of 1.0V and above a hyperbolic sine function (eq. 5.14) was used to model the tilt profile (Newton and Spiller, 2001). The coefficients A_1, A_2 and A_3 were used as fitting parameters.

$$\theta(z) = \frac{A_1 \sinh\left[\frac{(d-z)}{A_2}\right]}{\sinh\left[\frac{d}{A_2}\right]} + A_3 \qquad \text{Eq. 5.14}$$

This expression was chosen as it was found to produce curves which closely resembled those of modelled HAN cell tilt profiles. The coefficients required also varied over a range suitable for use in a fitting procedure, and as sinh(0) = 0, the coefficient A_3 is equal to the tilt angle at $z=d$ (i.e. the homogeneous surface of the cell). In all cases, the azimuth was set to a constant value through the cell of 0°.

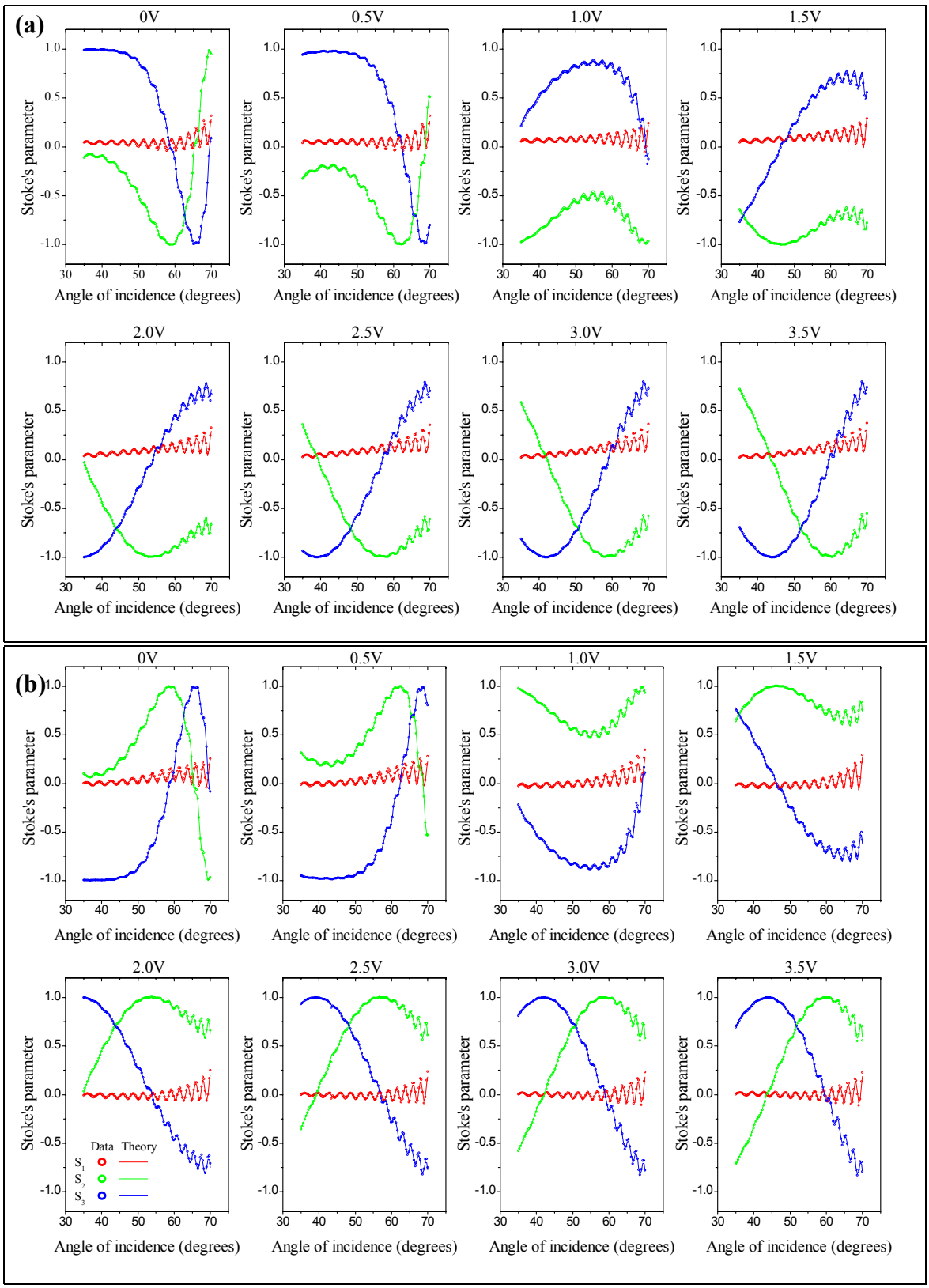

Fig. 5.3 **Fitted Stokes' parameter versus angle-of-incidence data collected for input polarised light at (a) 45° and (b) 135° with various 10kHz AC rms voltages applied perpendicular to the cell substrates.**

The multi-layer optics modelling program used implemented the Berreman method, using a LabVIEW front-end to facilitate the fitting process. Once the optical parameters had been determined by using data from a couple of voltages, they were held constant, and the tilt profile coefficients were adjusted for each voltage until good agreement was achieved between the model and measured Stokes' parameters data. The parameters for each of the optical layers obtained from the fitting routine are shown in table 5.1. These values show good agreement with previously measured values

Optical Layer	n_r	k_i	Thickness
ITO	1.82 ± 0.01	$(-8 \pm 1) \times 10^{-3}$	30 ± 2 nm
Rubbed polyimide	1.52 ± 0.01	$(-0.1 \pm 0.05) \times 10^{-3}$	73 ± 2 nm
ZLI-4788 ($n_\perp$)	1.643 ± 0.002	$(-0.1 \pm 0.2) \times 10^{-3}$	5.107 μm
ZLI-4788 ($n_{||}$)	1.485 ± 0.006	0.00 ± 0.002	
Homeotropic polymer	1.56 ± 0.01	0.00 ± 0.005	32 ± 2 nm

Table 5.1 Values for the real and imaginary refractive indices and thickness for the layers used in the multi-layer optics fitting routine

5.4.1 Calculation of physical constants

The resulting tilt profiles for each voltage are shown as circles in fig. 5.4. As the material under study is of a negative dielectric anisotropy, the application of a voltage causes the director to align *perpendicular* to the applied field (i.e. parallel to the substrate).

To obtain elastic constants and dielectric permittivities of the liquid crystal, the measured tilt profiles were compared with model tilt profiles generated by the Autronic-Melchers DIMOS liquid crystal modelling package. The modelling code uses the cell thickness, elastic constants and dielectric constants of the liquid crystal to calculate the static tilt profile when a voltage V is applied across the cell. By generating profiles for several different voltages for a particular combination of the coefficients and comparing them with the measured profiles, the liquid crystal parameters can be determined.

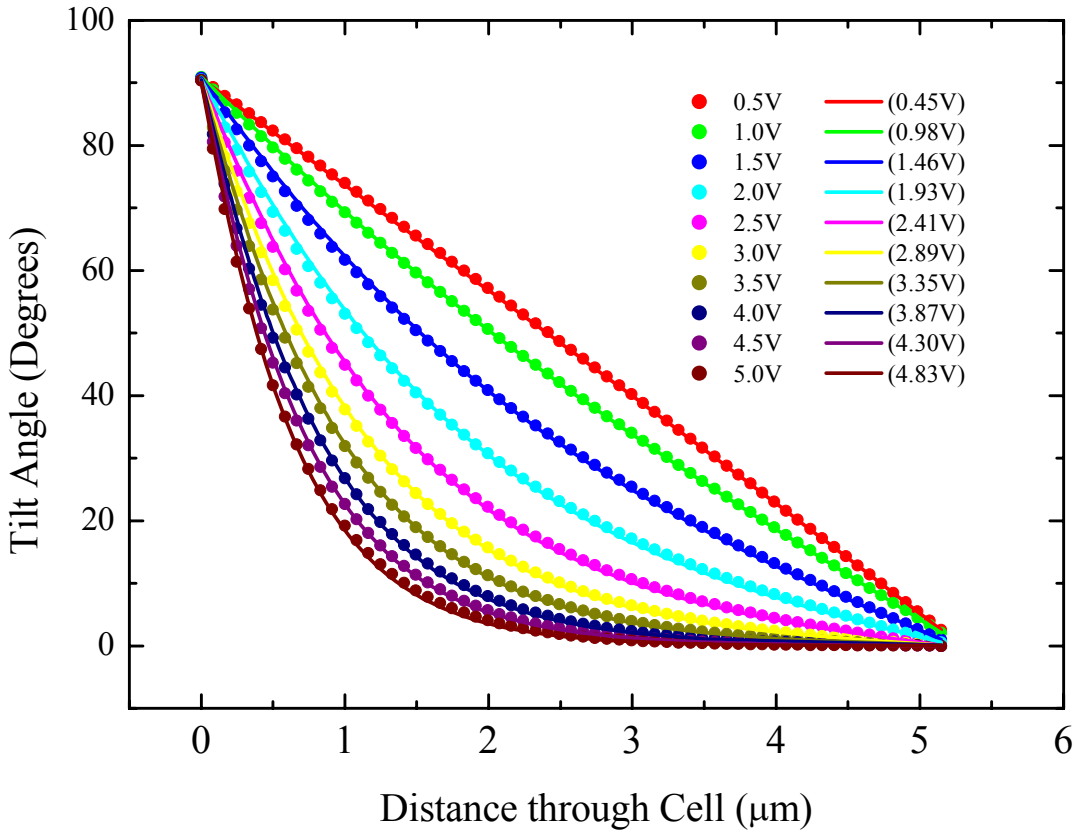

Fig. 5.4 **Measured tilt profiles (circles) for various applied 10kHz AC voltages applied to a 5.11μm ZLI-4788 filled HAN cell. The results of modelling the cell using the DIMOS modelling package and parameters given in table 5.2 are shown as solid lines, with the fitted voltages shown in brackets.**

In practise, it was found that it was not possible to fit to the measured profiles by simply varying K_{11}, K_{33}, $\varepsilon_{\perp}$ and $\varepsilon_{//}$ within sensible bounds either side of the values published by the liquid crystal manufacturer (Merck) using the voltage applied. However, it was found that for every voltage (except 0V) it was possible to produce a reasonable comparison by setting the voltage applied in the model to a value slightly lower than the actual applied voltage, whilst maintaining the coefficients at a value consistent with the published values (Table 5.2).

Parameter	Value
K_{11}	13.70 ± 0.02 pN
K_{33}	18.90 ± 0.02 pN
$\varepsilon_{\perp}$	10.20 ± 0.05
$\varepsilon_{//}$	4.5 ± 0.05

Table 5.2 Values for the elastic constants and dielectric coefficients produced from modelling using the DIMOS modelling program.

When the "model" voltage was plotted against the actual voltage, a clear linear trend emerged (fig. 5.5). The gradient of the best-fit line shown is 0.963 ± 0.004 and the intercept is at 0.00 ± 0.01 V. This result suggests that for each voltage, 96.3 ± 0.4 % of the voltage is dropped across the cell, implying that the remainder is dropped across the polymer layers that lie between the ITO and liquid crystal at both surfaces. This explanation can be verified to a first approximation by considering the ratio of the liquid crystal layer thickness to the total distance between the two ITO layers. Using the layer thickness data given in table 5.1, 98 ± 0.2 % of the material between the electrodes is liquid crystal, and so the assumption that the discrepancy in the two voltages is due to a voltage drop across the polymer layers is not quite valid, but in the correct direction. Voltage drops across the ITO layers may also contribute to the discrepancy.

The applied voltage may also be reduced by finite currents in the cell due to ionic contaminants in the liquid crystal material. It was shown in chapter 4 that the use of rubbed polyimide can produce free-ions, resulting in an effective drop in the voltage across the cell, hence reducing the distortion of the director profile.

The voltage-drop explanation for the discrepancy between measured and modelled tilt-profiles is further justified due to the intercept of the best-fit line passing through the origin. This suggests that the voltage change is not due to an internal voltage in the cell (e.g. flexoelectricity) and must instead be due to some dielectric or reactive property of the cell. This effect was not observed in the cells measured in chapter 4 due to the relatively thin layers of SiO_x used as homogeneous alignment layers, and the use of a monolayer of OTMS as a homeotropic aligner. These cells were also known to have an extremely low conductance.

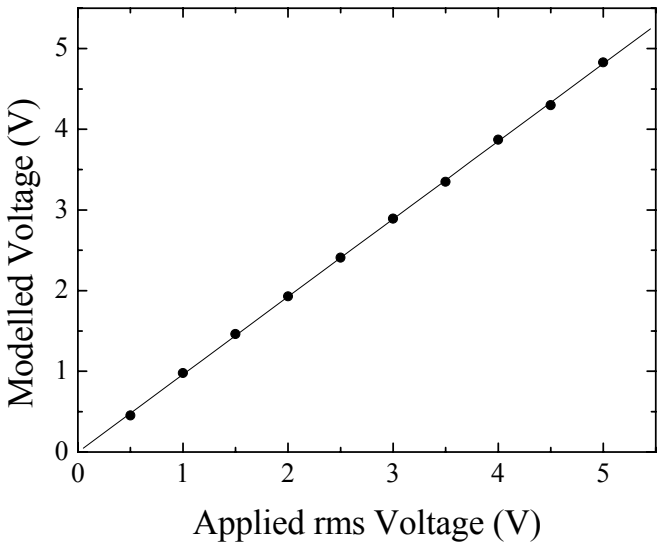

Fig. 5.5 Voltage used in the DIMOS modelling program plotted against the actual voltage applied, with the best linear fit shown.

5.4.2 Calculation of homogeneous anchoring energy

In theory, as the voltage increases, the tilt angle at the homeotropic surface should decrease as the director is pulled away from the homeotropic surface. However, the measured tilt profiles show no noticeable variation in the tilt angle at the homeotropic surface as the applied voltage increases. This suggests very strong anchoring at the liquid crystal/homeotropic polymer interface.

In contrast, at the homogeneous surface the director profile at 0V shows a surface pre-tilt of 2.43°. As successive voltages are applied, this pretilt decreases until at 2.5V, the surface tilt angle reaches 0°, and thereafter no change is seen as the voltage is increased (fig. 5.6).

From the pretilt and the gradient of the tilt profile at the homogeneous surface it is possible to calculate the anchoring energy, W_θ, at the rubbed-polyimide/liquid crystal interface by using the Rapini-Papoular equation (Rapini and Papoular, 1969). In the case of a non-twisted HAN cell the surface torque balance equation is:

$$\left(K_{11}\cos^2\theta_d + K_{33}\sin^2\theta_d\right)\theta_d' = 0.5W_\theta \sin 2\left(\theta_d - \theta_0\right) \qquad \text{Eq. 5.15}$$

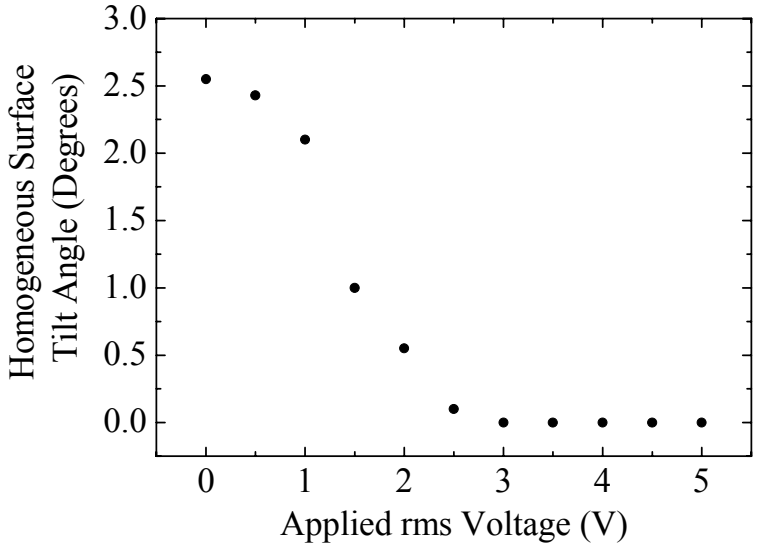

Fig. 5.6 Homogeneous surface tilt angle (at $z = d$) plotted against the 10kHz AC rms voltage applied across the cell.

where, K_{11} and K_{33} are the splay and bend elastic constants, θ_d and $\theta'_d = \left.\frac{\partial\theta}{\partial z}\right|_{z=d}$ are the tilt angle and tilt gradient at the homogeneous surface respectively, and θ_0 is the tilt angle of the easy-axis (i.e. the surface tilt for an infinitely thick cell). In the case of a HAN cell with small deviations (< ~5°) from the easy axis, the homogeneous anchoring energy is given by:

$$W_\theta = \frac{K_{11}\theta'_d}{(\theta_d - \theta_0)} \qquad \text{Eq. 5.16}$$

Using this expression with the tilt angles and gradients shown in fig. 5.4 for voltages up to 2.5V and then averaging the results gives the homogeneous anchoring energy as **1.2 ± 0.3 Jm^{-2}**. This result compares favourably with homogeneous anchoring energy measurements made for other nematic materials (Welford and Sambles, 1987; Yang et al, 2001))

5.5 Conclusions

This study has used a polarimetry technique to measure the static tilt-profiles when a series of high frequency AC fields were applied perpendicular to the substrates of a 5.11μm HAN cell filled with a material of negative dielectric permittivity. The profiles were determined by collecting the Stokes' parameter values versus angles-of-incidence for polarised light transmitted through the cell, and then comparing to theoretical data produced by a multi-layer optics model.

From these profiles, the elastic constants and dielectric permittivities of the material were determined. It was found that for each different voltage value of the 10kHz AC voltage applied, the voltage across the liquid crystal was 96.3 ± 0.4 % of the voltage supplied from the signal generator. Two reasons for this discrepancy were suggested:

i) Part of the voltage may have been dropped across the aligning polymer layers, resulting in a reduced voltage across the liquid crystal material.

ii) Finite currents in the cell due to ionic contamination from the rubbed polyimide aligning layer may have reduced the effective voltage across the cell due to voltage drops across the ITO electrodes, discussed previously in chapter 4.

Finally, the anchoring energy at the homogeneously aligned surface was determined from the change in surface tilt angle with applied voltage, and was measured as 1.2 ± 0.3 Jm^{-2}. This result compared well with values published for similar materials.

Chapter 6

Development of a Nematodynamics Modelling Routine for HAN Cells

6.1 Introduction

Over the past 20 years the images displayed on liquid crystal devices have changed from the generally static, such as in digital watches and calculators, to full colour motion pictures, as produced by televisions and projectors. The "smoothness" of these moving images is determined by the time that it takes for the liquid crystal director to respond to the change in applied voltage. The human eye detects "flicker" in a moving image at a frame rate below 25 frames per second, and hence the response of the pixels in a liquid crystal display must be faster than 40 ms.

To enable the production of liquid crystal devices with the ability to display moving images of a quality that rivals or even surpasses that of the conventional cathode-ray tube (CRT) display, a good understanding of the dynamics of the liquid crystal director is vital. In this chapter, the complex fluid dynamics associated with liquid crystals is discussed, and the key equations governing the dynamic response of the director specifically for a HAN cell are derived. These equations are then used to produce a program to model the dynamic response of a HAN cell to various changes in applied electric fields, revealing how a phenomena known as "backflow", originally associated with twisted nematic cells (Berreman (1975)), can also be observed in non-twisted HAN cells.

6.2 Isotropic fluid dynamics

When considering the dynamics of a fluid in motion, the equations derived refer to a volume element at a point **r**(*x, y, z*) at time *t*, rather than to individual particles. These volume elements contain a vast number of fluid particles, which are considered to be infinitely small. The fluid dynamics at a point in space **r**(*x, y, z*) can be described from the fluid velocity at that point, **v**(**r,t**) along with the two thermodynamic properties, the hydrostatic pressure, p(**r**,t) and the fluid density ρ (**r**,t).

For an isotropic fluid, three fundamental equations enable the basic properties of fluid flow to be understood. A brief description of each is given here as an introduction to fluid dynamics, and they will be developed further in the section of this chapter concerned with anisotropic fluids. A full account of the derivation of these equations is given in Landau and Lifshitz (1959).

6.2.1 Conservation of Mass

For a point in space **r**(*x, y, z*) the mass flow per unit time across a unit area is the component of ρ**v**(*x, y, z*) normal to the surface. By considering conservation of mass, the rate of decrease in the density per unit time is linked to the variation of the mass element ρ**v** over the surface of a small volume:

$$\nabla \cdot (\rho \mathbf{v}) = -\frac{\partial \rho}{\partial t} \qquad \text{Eq. 6.1}$$

Further derivation is restricted to incompressible fluids. Therefore, the density is considered as a constant and is invariant in time and space giving:

$$\nabla \cdot [\mathbf{v}(\mathbf{r},t)] = \nabla \cdot [\rho(\mathbf{r},t)] = 0 \qquad \text{Eq. 6.2}$$

This incompressibility condition is considered true for both isotropic and anisotropic fluids.

6.2.2 Euler's Equation

For an ideal, incompressible, non-viscous fluid Newtonian mechanics gives the force **F** experienced by a volume of fluid with momentum **P** as equal to the rate of change of momentum of the fluid volume. This force is equal to the pressure acting on the surface of the volume element.

$$\mathbf{F} = \frac{d\mathbf{P}}{dt} = -\int p \, d\mathbf{s} \qquad \text{Eq. 6.3}$$

Converting this surface integral to a volume integral gives an expression for the net force exerted on a unit volume of the fluid by pressure p in terms of the acceleration of the fluid element:

$$\rho \frac{d\mathbf{v}}{dt} = -\nabla p \qquad \text{Eq. 6.4}$$

This equation can be re-written to describe the acceleration of the fluid at a fixed point in space and is known as Euler's equation:

$$\rho\left[\frac{\partial \mathbf{v}}{\partial t} + (\mathbf{v}\cdot\nabla)\mathbf{v}\right] = -\nabla p \qquad \text{Eq. 6.5}$$

6.2.3 The Navier-Stokes Equation

The two equations derived so far in this section have considered only ideal, non-viscous fluids. However, a true description of the dynamics of a fluid system must also consider the dissipation of energy in a moving fluid due to internal friction. This effect can be accounted for by the inclusion of a viscosity term in the momentum flux density tensor, as described in detail later in this chapter. The result of this is the addition of a term (known as the viscous stress tensor) to the right hand side of Euler's equation. For an isotropic liquid, the viscosity is described by just one viscosity coefficient η_{iso} and the result is the Navier-Stokes equation:

$$\rho\left[\frac{\partial \mathbf{v}}{\partial t}+(\mathbf{v}\cdot\nabla)\mathbf{v}\right]=-\nabla p+\eta_{iso}\nabla^{2}\mathbf{v} \qquad \text{Eq. 6.6}$$

6.3 The Leslie-Eriksen-Parodi Theory

The hydrodynamic equations discussed so far describe an isotropic system where variations in the *x, y* and *z* directions of the fluid body are equivalent. However, for an anisotropic fluid, such as a liquid crystal, this symmetry is lost. The coupling between the director and the fluid motion adds an increased level of complexity to the hydrodynamic equations.

A first attempt at formulating a hydrodynamic theory for liquid crystals was made as long ago as 1933 [Anzelius, 1933]. However, it was not until the publication of Frank's elastic theory (1958) and the development of the modern theory of rational mechanics in the 1950's that any significant progress was made. These tools have enabled the development of the modern theory of "nematodynamics" by Eriksen (1961, 1962), Leslie (1966, 1968) and Parodi (1970). The resulting complete dynamics theory is commonly referred to as the Leslie-Eriksen-Parodi (LEP) theory.

In the case of an anisotropic fluid, the variation in director orientation with time has to be considered when describing the dynamics of the system. This leads to a total of five independent viscosity coefficients, known as the Leslie coefficients (α_1, α_2, .. α_5), being required to describe the dynamical properties of a liquid crystal system[1]. These coefficients can be combined in different ways to produce the five Miesowicz coefficients (η_1, η_2, η_3, η_{12} and γ_1) which are used to define the viscosities associated with the physical shear flow and rotational situations outlined below. The relationships between the Miesowicz and Leslie Coefficients is given in Appendix 1.

[1] Originally, it was believed that there were six independent Leslie coefficients, but it was shown by Parodi (1971) that $\alpha_6 = \alpha_2 + \alpha_3 + \alpha_5$

6.3.1 Shear Viscosity Coefficients

The first four Miesowicz coefficients describe the translational motion (shear flow) of the fluid relative to certain planes of interest. These are shown in fig 6.1 and are summarised as:

η_1 Director is parallel to the velocity gradient (Fig. 6.1(a))

η_2 Director is parallel to the flow direction (Fig. 6.1(b))

η_3 Director is normal to the shear plane (Fig. 6.1(c))

η_{12} Viscosity due to a stretch deformation around the director (Fig. 6.1(d))

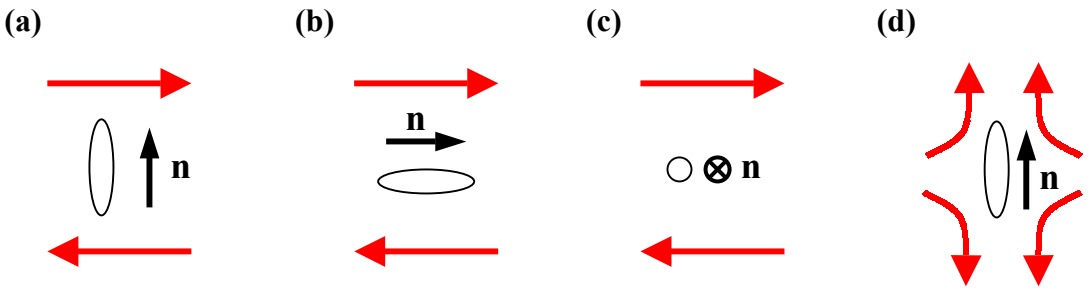

Fig. 6.1 Diagram to show the direction of the shear flow (red arrows) relative to the director orientation for the four shear viscosity coefficients (a) η_1 ; (b) η_2 ; (c) η_3 and (d) η_{12}.

6.3.2 Rotational Viscosity Coefficient

The fifth viscosity coefficient in the LEP theory is the rotational viscosity coefficient, γ_1. This governs the motion of the director when fluid flow is not involved, but rather, the director is rotated due to a viscous torque. This coefficient has been found to be particularly important in determining the dynamic response time of homogeneously aligned nematic cells (Smith, 2001).

6.4 Nematodynamics in 1D

The three equations which govern the hydrodynamics of an isotropic fluid each have an equivalent form in the LEP theory. In the following derivations, the general cases for the Navier-Stokes equation, the equation of motion and the continuity equation are derived for a general Euler co-ordinate system and then simplified to the 1D HAN cell geometry ($d/dx = d/dy = 0$) with no twist. In this case, the unit director **n** is described in the *x*-*y*-*z* co-ordinate system as:

$$n_x = \cos\theta \qquad n_y = 0 \qquad n_z = \sin\theta \qquad \text{Eq. 6.7}$$

6.4.1 Conservation of Mass

As in the case of an isotropic fluid, the anisotropic fluid is assumed to be incompressible, and so the incompressibility condition $\nabla \cdot \mathbf{v} = 0$ holds true as in the case of an isotropic fluid.

6.4.2 The Euler-Lagrange Equation of Motion

The equation of motion for the director within a nematic liquid crystal cell is a balance between the generalised elastic, electromagnetic and viscous forces of the system. The elastic and electromagnetic forces are conservative forces within the system, and are a function of θ, z and $d\theta/dz$. The viscous force is a dissipative force and arises due to a coupling between the translational and rotational motion of the molecules (i.e. the rotation of the molecules in one area can induce flow in an adjacent region, and vice versa.). This force is derived from the Raleigh dissipation function, $\Re$, of the system (Goldstein, 1980). By considering the total energy, the equation of motion can be taken directly from the standard Euler-Lagrange equation for the system:

$$\frac{d}{d_i}\left(\frac{\partial L}{\partial_i q}\right) - \left(\frac{\partial L}{\partial q}\right) = \frac{\partial \Re}{\partial \dot{q}} \qquad \text{Eq. 6.8}$$

where L is the Lagrangian of the system, $i = x, y, z$; $q = \theta, \phi$; $\partial_i q = \frac{\partial q}{\partial i}$; $\dot{q} = \frac{dq}{dt}$

a) Derivation of the Lagrangian of the system

The Lagrangian of the system is given by the sum of the elastic and electromagnetic free energy densities.

$$L = F_{el} + F_{em} \qquad \text{Eq. 6.9}$$

The general elastic free-energy density of the system is given by the Frank elastic energy equation (Frank, 1958):

$$F_{el} = \frac{1}{2}k_{11}(\nabla \cdot \mathbf{n})^2 + \frac{1}{2}k_{22}(\mathbf{n} \cdot (\nabla \times \mathbf{n}))^2 + \frac{1}{2}k_{33}(\nabla \times (\nabla \times \mathbf{n}))^2 \qquad \text{Eq. 6.10}$$

In the case of a non-twisted 1D HAN cell, this reduces to:

$$F_{el} = \frac{1}{2}\left(k_{11}\cos^2\theta + k_{33}\sin^2\theta\right)\left(\frac{d\theta}{dz}\right)^2 \qquad \text{Eq. 6.11}$$

The total electromagnetic free energy density has electric and magnetic components given by:

$$F_{em} = \frac{1}{2}\mathbf{D} \cdot \mathbf{E} + \frac{1}{2}.\underline{\underline{\chi}}\,\mathbf{H} \cdot \mathbf{H} \qquad \text{Eq. 6.12}$$

where **D** is the displacement field, **E** is the electric field vector, $\underline{\underline{\chi}}$ is the magnetic susceptibility tensor and **H** is the magnetic field vector. However, this study is only concerned with the response of the cell to an electric field, and hence the magnetic term will be excluded from further discussions. The 1D HAN cell structure with an electric field applied perpendicular to the substrate (i.e. in the *z*-direction only) allows simplification of the electric energy term, which becomes:

$$F_{em} = -\frac{1}{2}D_z E_z \qquad \text{Eq. 6.13}$$

As discussed in chapter 3, the displacement field has contributions from both the dielectric anisotropy and the flexoelectric polarisation. From eq. 3.8, the electric field E_z becomes:

$$E_z(z) = \frac{2D_z - (e_{11} + e_{33})\sin 2\theta\left(\frac{d\theta}{dz}\right)}{2\varepsilon_0\left(\varepsilon_{//}\sin^2\theta + \varepsilon_\perp\cos^2\theta\right)} \qquad \text{Eq. 6.14}$$

where e_{11} and e_{33} are the splay and bend flexoelectric coefficients and $\varepsilon_{//}$ and $\varepsilon_\perp$ are the extra-ordinary and ordinary dielectric permittivities.

Therefore, the Lagrangian of the system is given by:

$$L = \frac{1}{2}\left(k_{11}\cos^2\theta + k_{33}\sin^2\theta\right)\left(\frac{d\theta}{dz}\right)^2 - \frac{2D_z{}^2 - D_z(e_{11} + e_{33})\sin 2\theta\left(\frac{d\theta}{dz}\right)}{4\varepsilon_0\left(\varepsilon_{//}\sin^2\theta + \varepsilon_\perp\cos^2\theta\right)} \qquad \text{Eq. 6.15}$$

b) Derivation of the Raleigh dissipation function

The Raleigh dissipation function $\mathfrak{R}$ contains terms dependent on the rotational viscosity and the shear flow gradients of the system. A full account of the dissipation function and it's derivation from the viscous stress tensor, σ_{ij} is given by Vertogen and de Jeu (1988). However, the only non-zero terms in the function for the HAN cell structure are:

$$\begin{aligned}\Re = &\frac{1}{2(\alpha_3 - \alpha_2)}\left[(\alpha_3 - \alpha_2)\left(\dot\theta\cos\theta + \cos\theta\frac{1}{2}\frac{dv_x}{dz}\right) + (\alpha_3 + \alpha_2)\cos\theta\frac{1}{2}\frac{dv_x}{dz}\right]^2 \\ &+ \frac{1}{2(\alpha_3 - \alpha_2)}\left[(\alpha_3 - \alpha_2)\left(-\dot\theta\sin\theta - \sin\theta\frac{1}{2}\frac{dv_x}{dz}\right) + (\alpha_3 + \alpha_2)\sin\theta\frac{1}{2}\frac{dv_x}{dz}\right]^2\end{aligned} \qquad \text{Eq. 6.16}$$

where v_x is the fluid flow in the x-direction ($v_y = v_z = 0$) and $\dot{\theta} = \frac{d\theta}{dt}$. For variations in the z-direction only, the Euler-Lagrange equation (eq. 6.8) becomes:

$$\frac{d}{dz}\left(\frac{\partial L}{\partial \theta'}\right) - \left(\frac{\partial L}{\partial \theta}\right) = \frac{\partial \Re}{\partial \dot{\theta}} \qquad \text{Eq. 6.17}$$

where $\theta' = \frac{\partial \theta}{\partial z}$. Therefore, combining this with equations 6.16 and 6.17 gives the equation of motion as:

$$\begin{aligned}(\alpha_3 - \alpha_2)\dot{\theta} + \frac{1}{2}\left((\alpha_3 - \alpha_2) + (\alpha_3 + \alpha_2)\cos 2\theta\right)\frac{\partial v_x}{\partial z} = \\ \left(k_{11}\cos^2\theta + k_{33}\sin^2\theta\right)\left(\frac{\partial^2\theta}{\partial z^2}\right) + (k_{33} - k_{11})\cos\theta\sin\theta(\theta')^2 \\ -\frac{d}{dz}\left(\frac{D_z(e_{11} + e_{33})\sin 2\theta}{4\varepsilon_0\left(\varepsilon_{//}\sin^2\theta + \varepsilon_\perp\cos^2\theta\right)}\right) + \frac{d}{d\theta}\left(\frac{2{D_z}^2 - D_z(e_{11} + e_{33})\sin 2\theta\,\theta'}{4\varepsilon_0\left(\varepsilon_{//}\sin^2\theta + \varepsilon_\perp\cos^2\theta\right)}\right)\end{aligned} \qquad \text{Eq. 6.18}$$

This expression is a general equation of motion for a HAN cell. At a time t, D_z can be calculated from the time varying voltage $V(t)$ by using eq. 3.18.

$$D_z = \left(\int_0^d \left(\varepsilon_{//}\sin^2\theta + \varepsilon_\perp\cos^2\theta\right)^{-1} dz\right)^{-1}\left(\int_0^d \frac{\sin 2\theta(e_{11} + e_{33})\theta'}{2\left(\varepsilon_{//}\sin^2\theta + \varepsilon_\perp\cos^2\theta\right)} dz - \varepsilon_0 V(t)\right) \qquad \text{Eq. 6.19}$$

The equation of motion derived here does not include terms involving free-ions and surface polarisation.

6.4.3 The Navier-Stokes equation

The Navier-Stokes equation for an anisotropic fluid is:

$$\rho\dot{v}_i = F_i + \sigma_{ji,j} \qquad \text{Eq. 6.20}$$

where F_i is the external body force acting on the fluid (e.g. gravitation) and ρ is the density of the fluid. $\sigma_{ji,\,j}$ is the differential of the ji^{th} element of the stress tensor, σ_{ji} with respect to j and $\dot{v}_i$ is the rate of change of the flow velocity **v** in the i direction with respect to time. The stress tensor σ_{ji} contains terms dependent on the hydrostatic pressure p, energy density F and flow gradients of the dynamic system, and is given by:

$$\sigma_{ji} = -p\partial_{ij} - \frac{\partial F}{\partial n_{k,j}} n_{k,i} + \alpha_1 n_k n_p A_{kp} n_i n_j + \alpha_2 n_j N_i + \alpha_3 n_i N_j + \alpha_4 A_{ij} + \alpha_5 n_j n_k A_{ki} + (\alpha_2 + \alpha_3 + \alpha_5) n_i n_k A_{kj} \quad \text{Eq. 6.21}$$

The five Leslie coefficients are denoted by α_n. A_{ij} is the symmetric part of the flow gradient tensor:

$$A_{ij} = \frac{1}{2}\left(v_{i,j} + v_{j,i}\right) \quad \text{Eq. 6.22}$$

and N_i contains the anti-symmetric part:

$$N_i = \dot{n}_i + \frac{1}{2} n_j \left(v_{i,j} - v_{j,i}\right) \quad \text{Eq. 6.23}$$

As the 1D structure varies along the z-axis alone, only the derivative of the stress tensor with respect to z (i.e. $j = z$) will be non-zero. Furthermore, $v_y = v_z = 0$ and $n_y = 0$, so the only non-zero component of the Navier-stokes equation is when $i = x$. Under these circumstances, the only stress tensor term that needs to be considered is σ_{zx} which is given by:

$$\sigma_{zx} = \alpha_1 n_x^2 n_z^2 v_x' + \alpha_2 n_z \left(\dot{n}_x + \frac{1}{2} v_x' n_z\right) + \alpha_3 n_x \left(\dot{n}_z + \frac{1}{2} v_x' n_x\right) + \frac{1}{2}\alpha_4 v_x' + \frac{1}{2}\alpha_5 n_z^2 v_x' + \frac{1}{2}(\alpha_2 + \alpha_3 + \alpha_5) n_x^2 v_x' \quad \text{Eq. 6.24}$$

where $v_x' = \frac{\partial v_z}{\partial z}$ In the case of the response of a nematic cell to a change in applied voltage, the inertial terms act over a time scale several orders of magnitude smaller than that of the overall response of the cell. As a result, the inertial terms can be neglected (i.e. $\rho \dot{v}_i = 0$) and since the external body forces F_i are negligible, the Navier-Stokes expression (eq. 6.20) simplifies to:

$$\rho \dot{v}_x = 0 = \frac{\partial}{\partial z}(\sigma_{zx}) \qquad \text{Eq. 6.25}$$

The integral of the RHS of this expression with respect to z is equal to a constant, *C*, which is a function of *t* but not *z*. By using the condition that:

$$\dot{n}_x = \frac{d}{dt}(\cos\theta) = -\dot{\theta}\sin\theta \qquad \text{Eq. 6.26}$$

$$\dot{n}_z = \frac{d}{dt}(\sin\theta) = \dot{\theta}\cos\theta \qquad \text{Eq. 6.27}$$

the Navier-Stokes equation for the response of a HAN cell to a change in applied voltage is:

$$C(t) = \dot{\theta}\left(-\alpha_2 \sin^2\theta + \alpha_3 \cos^2\theta\right) + \frac{1}{2}v_x'\left(2\alpha_1 \cos^2\theta \sin^2\theta + \alpha_2\left(\cos^2\theta - \sin^2\theta\right) + 2\alpha_3 \cos^2\theta + \alpha_4 + \alpha_5\right) \qquad \text{Eq. 6.28}$$

In terms of the Miesowicz coefficients, this becomes:

$$C(t) = \dot{\theta}\left(\left(\frac{\gamma_1 - \eta_1 + \eta_2}{2}\right)\cos^2\theta + \left(\frac{\gamma_1 + \eta_1 - \eta_2}{2}\right)\sin^2\theta\right) + \frac{1}{2}v_x'\left(\eta_{12}\cos^2\theta\sin^2\theta + (\eta_1 - \eta_2)\sin^2\theta + \eta_2\right) \qquad \text{Eq. 6.29}$$

6.5 HAN cell dynamics modelling program

The equation of motion and the Navier-Stokes equation allows the modelling of the director profile with time to be determined when at time $t = 0$ a voltage is either applied across or removed from a HAN cell. The iterative process used to solve the equations at discrete points in time is a standard numerical technique, and has been used previously to model the dynamics of twisted nematic cells (Berreman (1975), van Sprang et al (1988)) and, more recently, pi-cells (Walton et al, 2000).

The HAN cell modelled has a thickness d, and rigid surface anchoring at the upper and lower surfaces is assumed ($\dot{\theta}_0 = \dot{\theta}_d = 0$). θ_0 and θ_d remain unchanged throughout the modelling routine, although their derivatives with respect to z are allowed to vary. The cell is divided into n equally spaced points, and these are labelled with indices from i=1 at the upper surfaces to i=n at the lower surface.

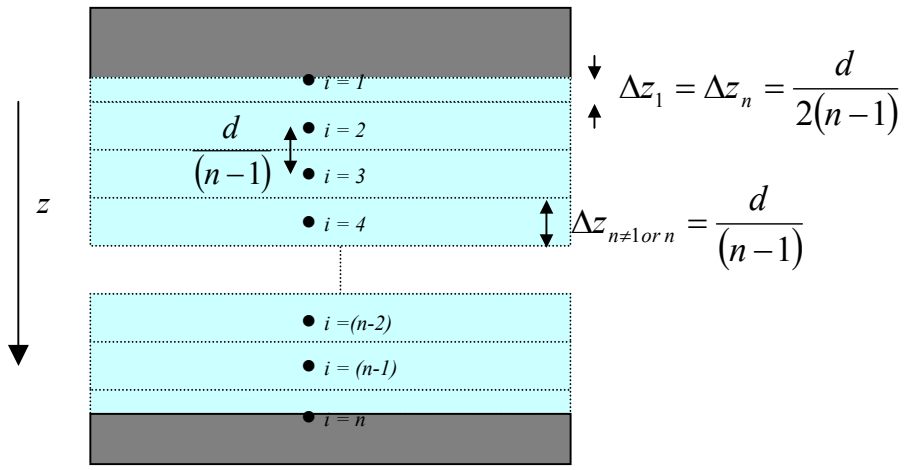

Fig. 6.2 Diagram to show the spacing in the HAN cell used in the modelling program

The modelling program has been specifically written to model a HAN cell, and a flow-chart illustrating the modelling process is given in fig. 6.3. The same model is used for both switch-on and switch-off dynamics, as only the initial static profile and the applied voltage parameters are different.

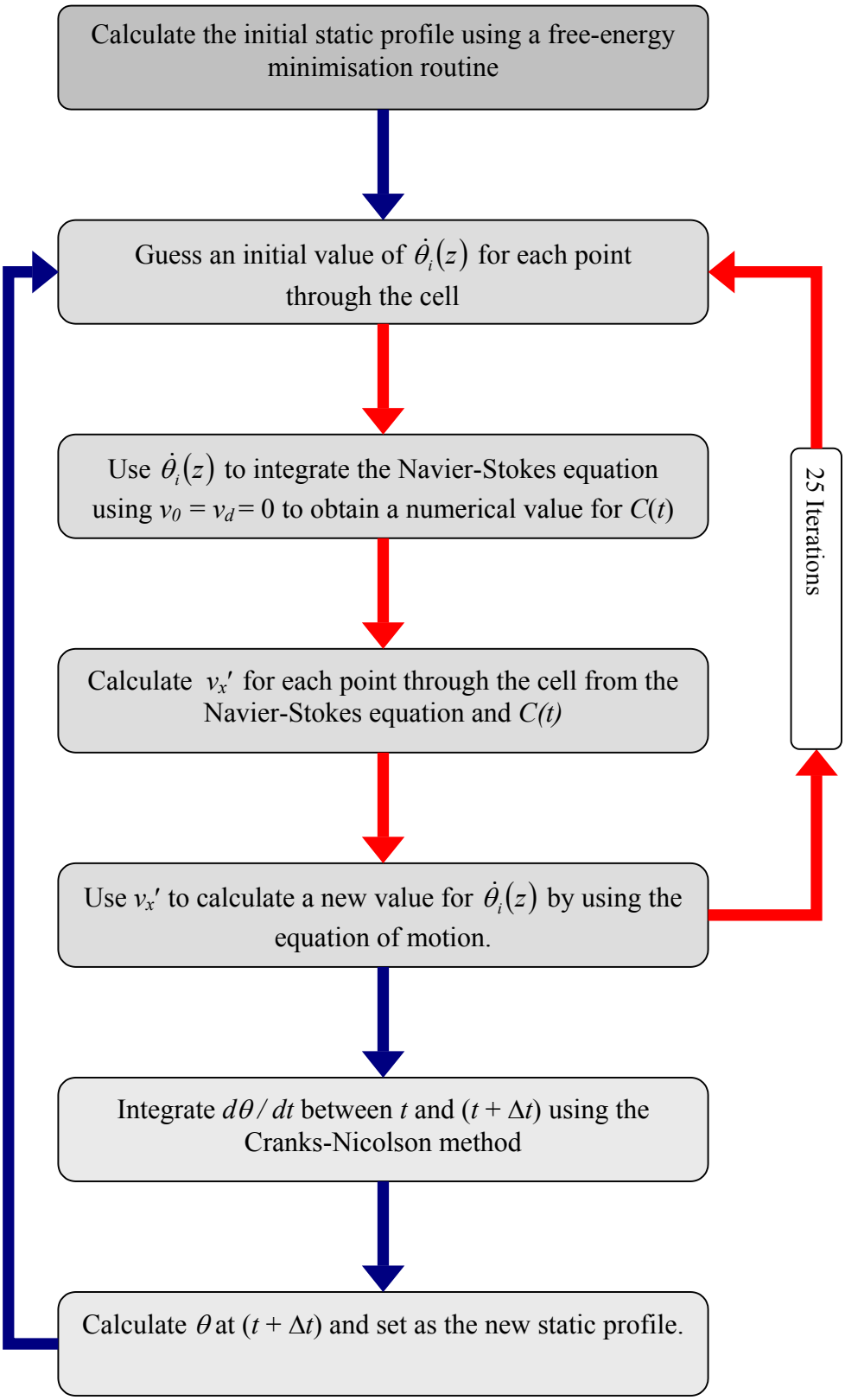

Fig. 6.3 Flow diagram to show the operation of the HAN cell dynamics modelling routine

The first stage involves the calculation of the static director profile at time *t=0*. This is done by using a free-energy minimisation method, as discussed in chapter 3. Alternatively, the profile can be obtained by setting the flow-gradient and $\dot{\theta}$ in the equation of motion (eq. 6.18) to zero, and solving the partial differential equation obtained.

The second stage is an iterative loop to calculate the value of $\dot{\theta}$ for each point at time *t=0*. To start with, an initial guess of the value of $\dot{\theta}(z)$ at time *t=0* needs to be made. In practise, it was found that simply setting $\dot{\theta}_i = 0$ was an adequate starting point.

The use of non-slip boundary conditions ($v_x=0$ at $z=0$ and $z=d$) means that by integrating the Navier-Stokes equation (6.29) with respect to z between $z=0$ and $z=d$ removes the flow-gradient term from the equation. The resulting expression can then be integrated numerically (eq. 6.30) and an initial guess for the constant *C(t)* at time *t=0* is obtained.

$$C(t) = \frac{1}{d}\sum_{i=1}^{n}\left(-\alpha_2 \sin^2\theta_i + \alpha_3 \cos^2\theta_i\right)\dot{\theta}_i \Delta z_i \qquad \text{Eq. 6.30}$$

θ_i is the (known) static value for θ at point *i* at $t=t_0=0$, and $\dot{\theta}_i$ is the guessed value of the rate of change of θ with time. Δz_i is the layer thickness at each point. In the modelling program produced, all the points through the cell are equally spaced, so the thickness attributed to the upper and lower points are $\Delta z_1 = \Delta z_n = \frac{1}{2}\left(\frac{d}{n-1}\right)$, with the remaining layers having $\Delta z_i = \left(\frac{d}{n-1}\right)$.

The value of *C(t)* is used in the Navier-Stokes equation to calculate v_x' for each point through the cell, and this is then used in the equation of motion (eq. 6.18) to calculate new values for $\dot{\theta}_i$. The whole iteration loop is then run through again, using the new values of $\dot{\theta}_i$ as the guessed values for the rate of change of θ with time. In total, it was found that, for the very first time-step calculation of $\dot{\theta}_i$ 50 iterations were

required before the value of *C(t)* (and hence the value of $\dot{\theta}_i$) converged to a reasonable level for time *t=0*. For subsequent time-steps, by using the value of $\dot{\theta}_i$ calculated for the previous time-step as the initial guess for $\dot{\theta}_i$, the number of iterations required reduced to 25 for time steps of 1μs.

The third stage involves using the (now known) values of $\dot{\theta}_i$ at $t=t_0=0$ to calculate a new static profile at $t=(t_0 + \Delta t)$ to second order. As the value of $\dot{\theta}_i$ varies over the time interval Δt, the Cranks-Nicolson technique is required to calculate numerically the new angle at $t=(t_0 + \Delta t)$. The equation used is:

$$\theta_i\left(t_0 + \Delta t\right) = \theta_i\left(t_0\right) + \frac{\Delta t}{2}\left[\dot{\theta}_i\left(t_0\right) + \dot{\theta}_i\left(t_0 + \Delta t\right)\right] \qquad \text{Eq. 6.31}$$

The value of $\dot{\theta}_i(t_0)$ at each point is known as this is the final value produced by the iterative process in stage 2 of the program. The value of $\dot{\theta}_i(t_0 + \Delta t)$ is calculated iteratively as before using the Navier stokes equation (6.29) with $C(t+\Delta t)$ initially set as $C(t)$ and $\theta_i(t_0 + \Delta t)$ given by the first order approximation:

$$\theta_i\left(t_0 + \Delta t\right) = \theta_i\left(t_0\right) + \Delta t\dot{\theta}_i\left(t_0\right) \qquad \text{Eq. 6.32}$$

The result of this is used in eq. 6.31 to obtain the new tilt profile at $t=t+\Delta t$. This profile is then used as the static tilt profile in stage 1 of the routine, and the whole process is repeated until the profile at the required time after the voltage is applied / removed is reached.

6.6 Switch-off dynamics (Applied DC Field)

To model the switch-off dynamics of a HAN cell, the starting profile used is the static director profile at an applied voltage. This can either be measured by experiment or modelled using the free-energy minimisation model described in chapter 3. When the voltage is removed, it is assumed that V drops to zero instantaneously, and the director responds accordingly.

The variation in tilt profile for a HAN cell relaxing from applied 10kHz AC rms voltages of 2V and 7V are shown in fig. 6.4 (a) and (c) respectively.

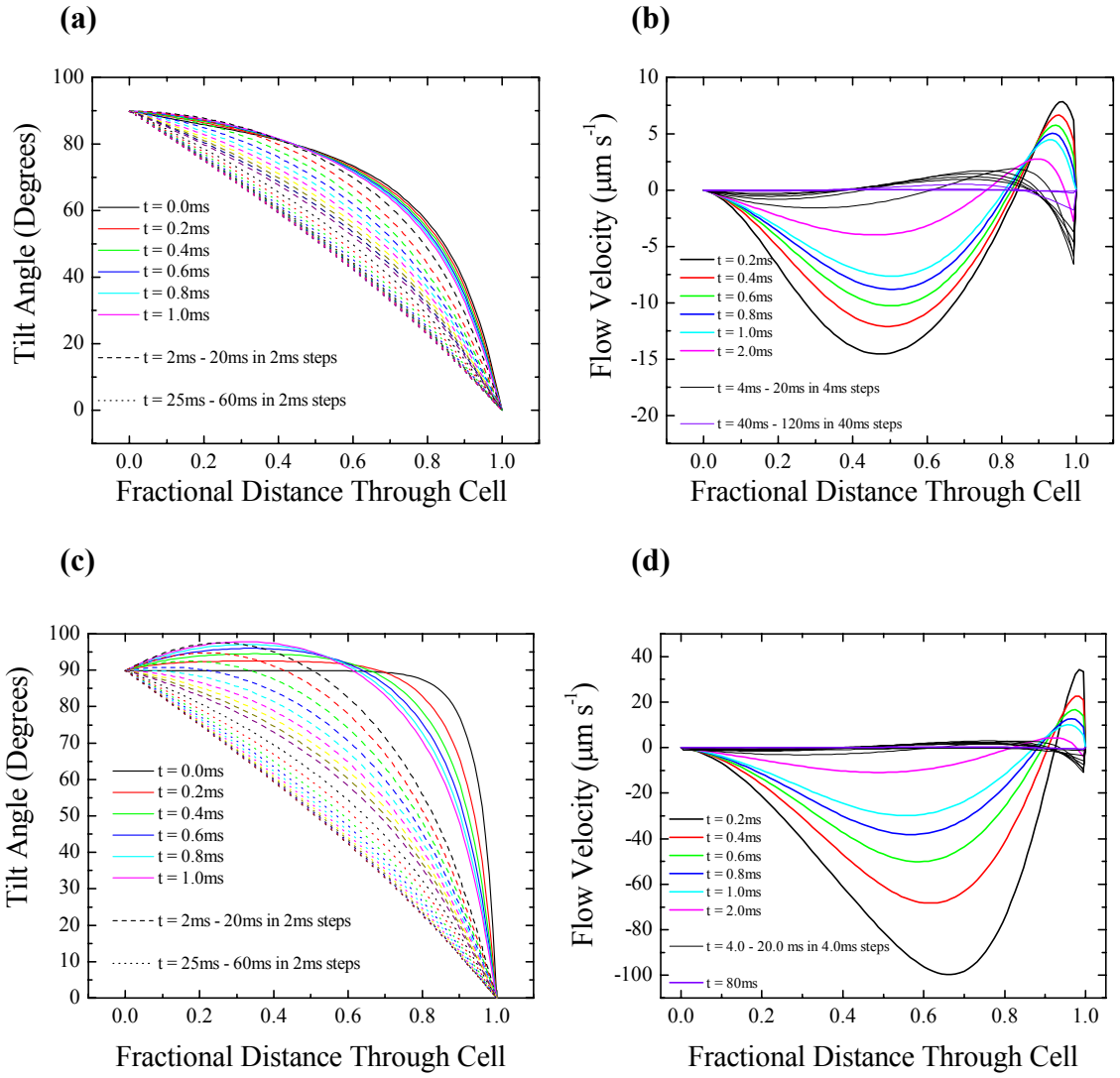

Fig. 6.4 Tilt profile and flow gradient profiles for relaxation from (a) and (b) 2V and (c) and (d) 7V rms AC in a 5μm ZLI-2293 HAN cell

The cell modelled is 5μm thick, and filled with ZLI-2293 with K_{11} = 12.5pN, K_{33} = 17.9pN, $\varepsilon_{\perp}$ = 4.1 and $\varepsilon_{//}$ = 14.1. In this case, the flexoelectric coefficient has been neglected as a high-frequency field is used. Infinite anchoring with surface tilt angles of 90° and 0° are assumed at the homeotropic and homogeneous surfaces respectively.

In both cases, immediately after the voltage is removed, the dynamics of the cell is driven solely by the viscous and elastic terms in the equation of motion (eq. 6.18) as the displacement field, D_z , is assumed to go to zero instantaneously as the flexoelectric terms are neglected.

The phenomenon known as backflow is observed in the region of the cell close to the homeotropic surface. In this region, instead of the tilt angle immediately decreasing towards the 0V static profile, the director tilts in the opposite direction, in some cases increasing above 90°, before relaxing back to the 0V state. A similar effect has previously been observed during the relaxation of a twisted nematic cell (Smith et al, 2000) and a pi-cell (Walton et al, 1999).

The origin of this motion in a homogeneously aligned cell with a field applied perpendicular to the substrate is discussed qualitatively by Chandrasekhar (1992), and this argument can be adapted for the case of a HAN cell. The backflow close to the homeotropic region is driven by the fluid motion close to the homogeneous surface. From the initial director profile for the 7V case, (fig. 6.14(c)) it can be seen that the greatest elastic torque will occur at around three-quarters of the way through the cell, as this is where the curvature is greatest. Whilst the field is applied, this elastic torque is balanced by an equal and opposite dielectric torque. However, when the electric field is removed the elastic torque is unopposed, producing a clockwise rotation of the director (fig. 6.5). The coupling between the fluid flow and the director rotation produces a net shear flow in the adjacent region, which in turn produces an anticlockwise torque in the first quarter of the cell. As the director in this region is uniformly aligned homeotropically, the elastic torque is small and does not oppose the induced anti-clockwise rotation. The director is therefore able to tilt above the 90° angle, before relaxing back down to the 0V state.

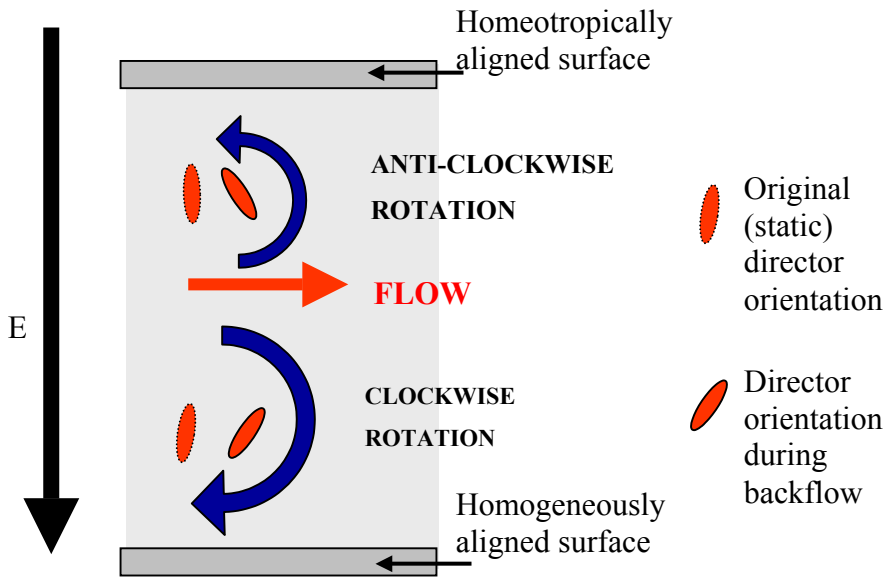

Fig. 6.5 Schematic diagram of backflow occurring during the relaxation of a HAN cell from an applied voltage.

Evidence for this opposing motion in the two regions of the cell can be seen by studying the flow profiles of the cell as it relaxes (Figs. 6.4 (b) and (d)). Clear correlations can be seen between the location of the peak flow velocity in the profiles, and the point in the cell at time t where $d\theta/dt = 0$.

6.7 Switch-on dynamics (Applied DC Field)

When an electric field is applied across a HAN cell originally at 0V, the director is driven by the force due to the coupling between the applied field and dielectric anisotropy of the material into the distorted state. The presence of this dielectric term in the equation of motion (eq. 6.18) results in the switch-on response time being much shorter than the relaxation time.

The result of applying a 10kHz AC field of rms voltage values 2V and 7V at *t=0* to a 5μm HAN cell initially at 0V is shown in fig. 6.6. The liquid crystal parameters used for the ZLI-2293 are the same as in the switch-off case above.

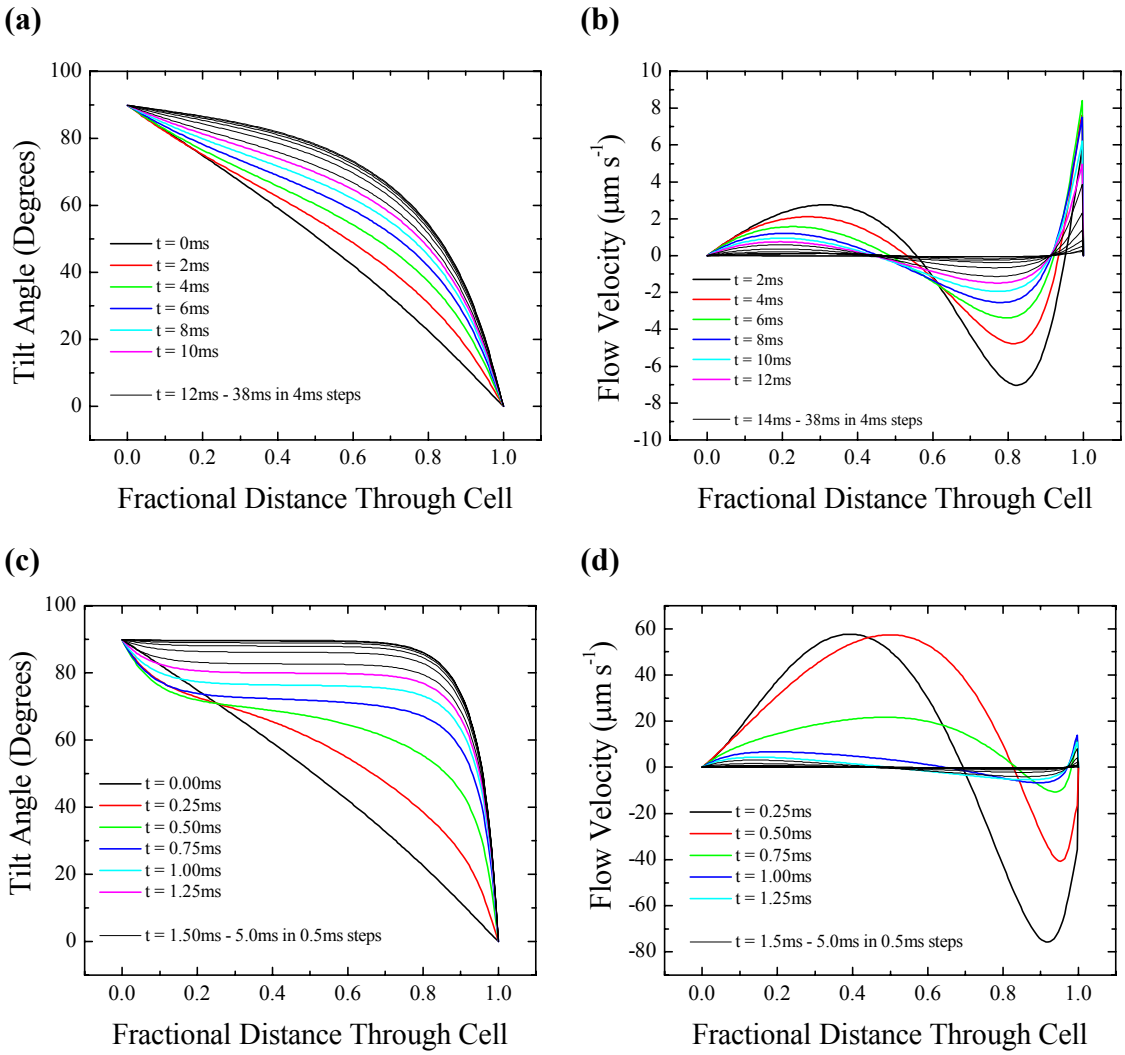

Fig. 6.6 Tilt profiles and flow velocity profiles for the switch-on dynamics from 0V to (a) and (b) 2V and (c) and (d) 7V rms AC in a 5μm ZLI-2293 HAN cell

As in the case of relaxation dynamics, the switch-on profiles show backflow occurring in the initial stages of the director response, although, in the case of 2V, the effect is very small. As before, the backflow in the homeotropic region of the cell appears to be driven by the fluid motion due to an unbalanced force acting in the homogeneous section of the cell. In the case of the switch-on dynamics, this force must be due to the dielectric response of the liquid crystal material to the applied field. By using eq. 6.14 the field distribution through the cell at the point in time when a voltage is first applied can be plotted. From fig. 6.7 it can be seen that, as discussed previously in chapter 3, the electric field profile through the cell is non-uniform. (It should be noted that as the system is in a non-equilibrium state, $\int_0^d E_z dz \neq 0$). In particular, due to the positive dielectric anisotropy of the material, the field is strongest in the homeotropic section of the cell as $\mathbf{D} = \varepsilon_\perp \mathbf{E}$ and so for a small value of $\varepsilon_\perp$, **E** is big.

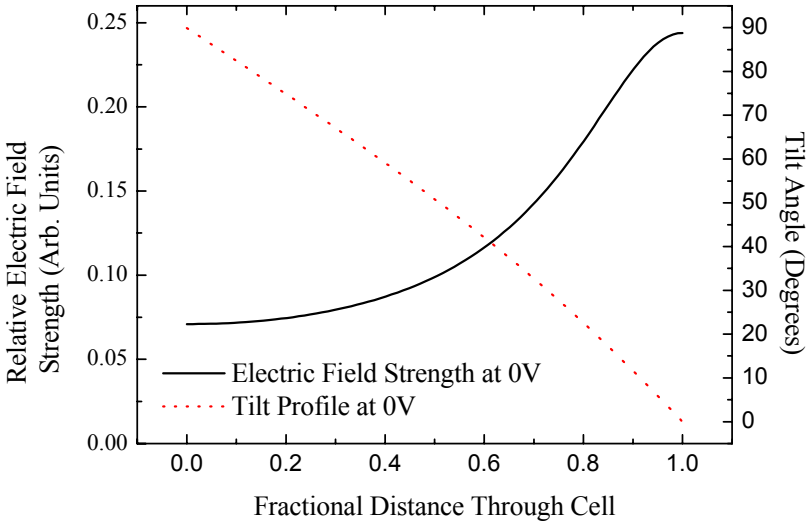

Fig. 6.7 Variation of electric field strength through a HAN cell originally at 0V immediately after an arbitrary voltage is applied to a material of positive dielectric anisotropy ($\varepsilon_{//} - \varepsilon_\perp = +10$).

The origin of the backflow seen during the switch-on of a HAN cell is therefore analogous to the backflow occurring during relaxation. In the switch-on case, the application of a field to the cell with a near-linear director profile in the 0V state instantaneously produces a strong torque on the director in the homogeneous half of the cell. As shown previously in fig. 6.5, the torque induces a region of shear flow in the

cell, which in turn causes the director in the homeotropic region (where the electric field strength is weaker) to rotate in the opposite direction, driving the director to a tilt angle higher than its initial starting point. This reorientation of the director causes the electric field distribution, and hence force experienced in different areas of the cell to vary with time. As a result, after a maximum tilt angle has been reached in the homeotropic region of the cell, the dielectric response of the molecules overcomes the backflow, and the director moves towards the static configuration for the applied voltage.

In the switch-on case, it is assumed that the applied (external) voltage instantaneously reaches its maximum value. The variation of the displacement field D_z with time (due to the re-orientation of the director) can therefore be calculated by using eq. 6.14. If the flexoelectric contribution is neglected, the displacement field D_z (which is constant across the cell) can be calculated from the applied voltage, V and the tilt profile using:

$$D_z = -V\varepsilon_0\left[\int_0^d\left(\varepsilon_{//}\sin^2\theta + \varepsilon_\perp\cos^2\theta\right)^{-1}dz\right]^{-1} \qquad \text{Eq. 6.33}$$

The variation of the displacement field with time after a 7V rms 10kHz voltage is applied is shown in fig. 6.8.

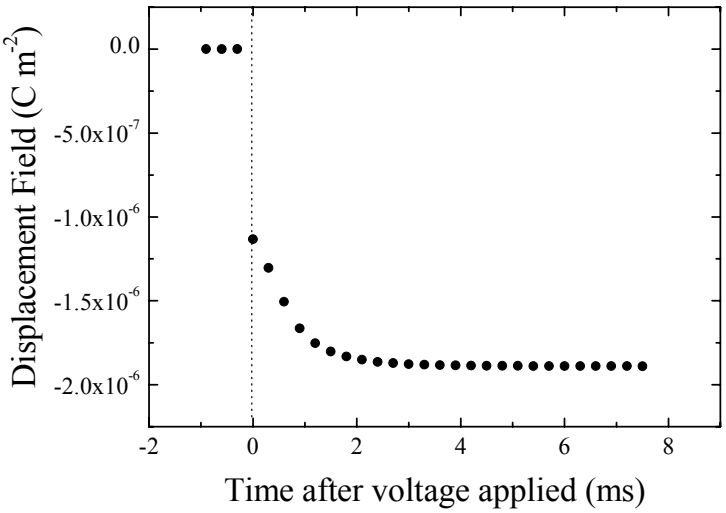

Fig. 6.8 Variation of displacement field with time for a HAN cell (originally at 0V) responding to an applied AC voltage of 7V rms applied at t = 0.

The influence of the strength of the applied field on the extent of the backflow produced is readily seen when the director profiles for the switch-on of the cell at 2V and 7V are compared. In both cases, the only initial distortion in the cell at 0V is the

splay and bend elastic deformation of the director. When the field is applied, this elastic distortion will oppose the dielectric response of the cell, and hence the higher the applied voltage, the faster the profile is driven to its equilibrium value.

6.8 Applied AC voltages ("Steady State")

The effect that the frequency of an applied AC field has on the "steady state" director profile of a HAN cell can be modelled by defining the applied voltage, V, in eq. 6.33 for each time-step. In the case of an AC voltage of rms value V_0 and frequency f the applied voltage becomes:

$$V(t) = \sqrt{2}\,V_0 \sin(2\pi f t) \qquad \text{Eq. 6.33}$$

The result of applying different frequency sinusoidal voltages to a HAN cell is shown in fig. 6.9. To highlight the influence of the sinusoidal field, the tilt angle at fractional distances of 0.1, 0.25, 0.75 and 0.9 through the cell have been plotted against time after a 5V rms AC voltage is applied.

In all cases, the tilt profile takes approximately 7ms to respond to the rms value of the applied AC voltage, and in each case, the calculation of the change in director profile with time is performed in 0.1μs steps, which is ample resolution for even the highest frequency used. The flexoelectric coefficient was set to zero in this modelling and therefore the free-energy equations are only dependent on E_z^2 giving the double-periodicity observed in the 100Hz and 1kHz traces .

In the 100Hz case the time period of the ac signal (10ms) is slow enough to allow the effect of driving the director with the applied field to be observed. In particular, in the region of the cell closest to the homeotropic surface the influence of backflow can be seen, both during the initial 2.5ms, where the cell is switching on from the 0V profile, (as discussed in section 6.7) and during the "steady state" period. This has been highlighted in fig. 6.9 (a) where the sinusoidal applied field has been superimposed on the director response. Due to the viscosity of the system, the director "lags" the applied voltage, but it is generally apparent that as $|V(t)|$ starts to increase θ initially decreases. Subsequently, as the field starts to decrease, the director tilts above

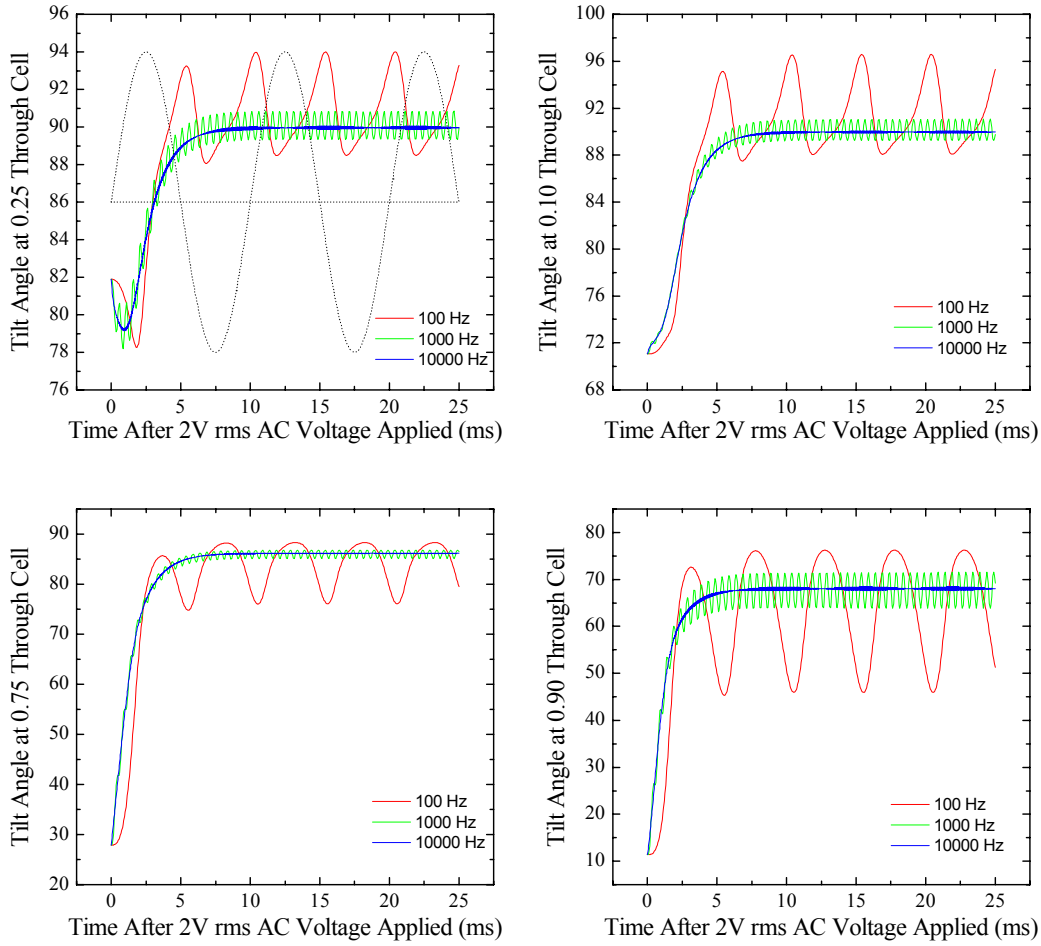

Fig. 6.9 Variation of tilt profile with applied ac voltages at fractional distances of (a) 0.1; (b) 0.25; (c) 0.75 and (d) 0.9 through a HAN cell

90° which indicates that backflow is again occurring. In contrast, at the opposite side of the cell where backflow is not occurring, the variation in director with time is far more symmetric (fig. 6.9 (d)).

This study also demonstrates that the use of high frequency (10kHz) ac fields to study the static profiles in the previous two chapters is valid. The response time of the director is sufficiently slow enough to respond to the rms value of the applied field and not the actual amplitude, and so it maintains a steady profile throughout the duration of the applied voltage. However, in this high frequency case, backflow is still clearly observed during the switch-on process on a timescale comparable to that of the lower frequencies. This indicates that the viscous torque which produces it is on a far greater timescale than that of the period of the applied 10kHz field.

6.9 Conclusions

In this chapter, the Leslie-Ericksen-Parodi theory for the fluid dynamics associated with liquid crystals has been introduced, and the differences between this theory and the hydrodynamics of an isotropic fluid have been highlighted.

The Euler-Lagrange and Navier-Stokes equations for a HAN cell geometry have been derived, and these have been used to model the dynamic response of the director when high-frequency AC electric fields are either applied or removed from the HAN cell. In both cases, the flow gradient in the cell during switching has also been calculated, indicating the origin of backflow, which is observed in both cases. The "steady-state" situation where AC voltages of different frequencies are applied across the cell has also been modelled to confirm the validity of using high-frequency AC fields when static director profiles are studied, as used in the previous two chapters.

In the following chapters, model tilt profiles produced by this dynamics modelling program will be compared with dynamic tilt profiles measured using the convergent beam technique.

Chapter 7

Convergent Beam Measurement of HAN Cell Switch-On Dynamics

7.1 Introduction

The nematodynamic model produced in the previous chapter has shown that the switch-on time for a HAN cell is of the order of a few milliseconds. This is several times faster than the equivalent response time of twisted or parallel cells containing a nematic liquid crystal. When measuring the director profile during the switch-on process, it is essential that the technique used has a time resolution in the sub-millisecond range whilst at the same time being sensitive to subtle changes in the tilt profile. The optical convergent beam technique is therefore ideal for studying the change in director during this transition process as data can be collected in 0.3ms steps. This technique is also particularly sensitive to subtle changes in the director profile, so the backflow (predicted by the modelling in chapter 6) occurring in the first few milliseconds of the reorientation process can be resolved in excellent detail.

In this chapter, the switch-on dynamics of a 5μm ZLI-2293 filled HAN cell is measured on a 0.3ms time-scale and compared to model profiles produced by the nematodynamics model discussed in the previous chapter. From these measurements the viscosity coefficients of the liquid crystal are determined, and the influence of each of the four viscosity coefficients used in the dynamic model is discussed.

7.2 Experiment

A HAN cell was constructed from two low-index glass ITO-coated substrates. Homogeneous alignment was produced by a 15nm layer of silicon monoxide evaporated at a 60° angle of incidence, and homeotropic alignment was produced by a monolayer of Octadecyltrimethoxysilane (OTMS) (fig. 7.1). The cell was spaced with 5μm beads dispersed in a UV setting glue, and a wire was attached to each surface using indium solder.

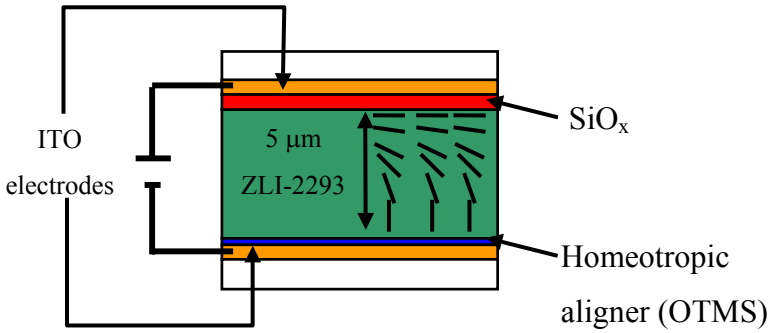

Fig. 7.1 Schematic diagram of the HAN cell used in the switch-on dynamics study.

The convergent beam experimental arrangement (as discussed in chapter 2) was used, and the cell was index-matched between two low-index glass hemispheres at a 60° azimuthal angle with the homeotropic surface as the incident face. The capture time of the CCD camera was set to 0.3ms, as this was found to be the minimum capture time that would allow a suitable resolution of the shallow oscillations in the optical intensity versus angle of incidence data for this cell at 0V. Optical data was then collected in transmission and reflection for polarisation conserving and converting signals of the incident *p*- and *s*-polarised light when a 7V rms 10kHz AC voltage was applied across the cell. In each case, data was captured over a 30ms period (i.e. 100 lines recorded) to ensure that the switch-on process was completely covered.

This data was then normalised and the optical-intensity versus angle of incidence data at each point in time was fitted to using the multilayer-optics modelling program discussed in chapter 2.

7.3 Results

The switch-on data collected for the 5μm HAN cell is shown in fig. 7.2. The colour at each point on the graphs denotes the intensity of the light at a pixel on the CCD array (corresponding to the angle-of-incidence shown on the horizontal axis) at a particular time after the voltage has been removed (shown on the vertical axis). In practise, it was found that of the reflectivity data taken, only the *s*- to *s*-polarisation conserving data was of an intensity strong enough to allow the data to be captured. In all other cases, any useful features were too low in intensity or obscured by noise in the system. However, the transmission data in all cases showed clear features during the transition between the two voltages.

Qualitative analysis of the optical data collected suggests that the speed of the switch-on transition in the case of this HAN cell is around 2.5ms. The transmitted data-sets (T_{pp}, T_{ps}, T_{sp} and T_{ss}) show an initial, very fast, change in intensity in the first few time steps, suggesting a rapid change in the director profile in the bulk. Similarly, the reflectivity data recorded (R_{ss}) shows a small but rapid shift in the position of the fully-leaky guided-modes immediately after the application of the voltage, but the actual change in the level of the optical intensity with time is far less dramatic. As the cell was mounted with the homeotropic alignment as the incident surface, this data suggests that although there is some small but rapid change at the homeotropic surface (e.g. backflow), overall there is little change occurring in that region of the cell.

The rapid response of the cell in comparison to the capture time of the CCD array means that only nine lines of optical data (i.e. time-steps) are available to characterise the transition from 0V to 7V. To highlight the speed at which the intensity at each pixel of the CCD, and hence the director profile changes, the variation in intensity with time at a 60° angle of incidence for the four transmitted data-sets has been plotted (fig. 7.2(e)).

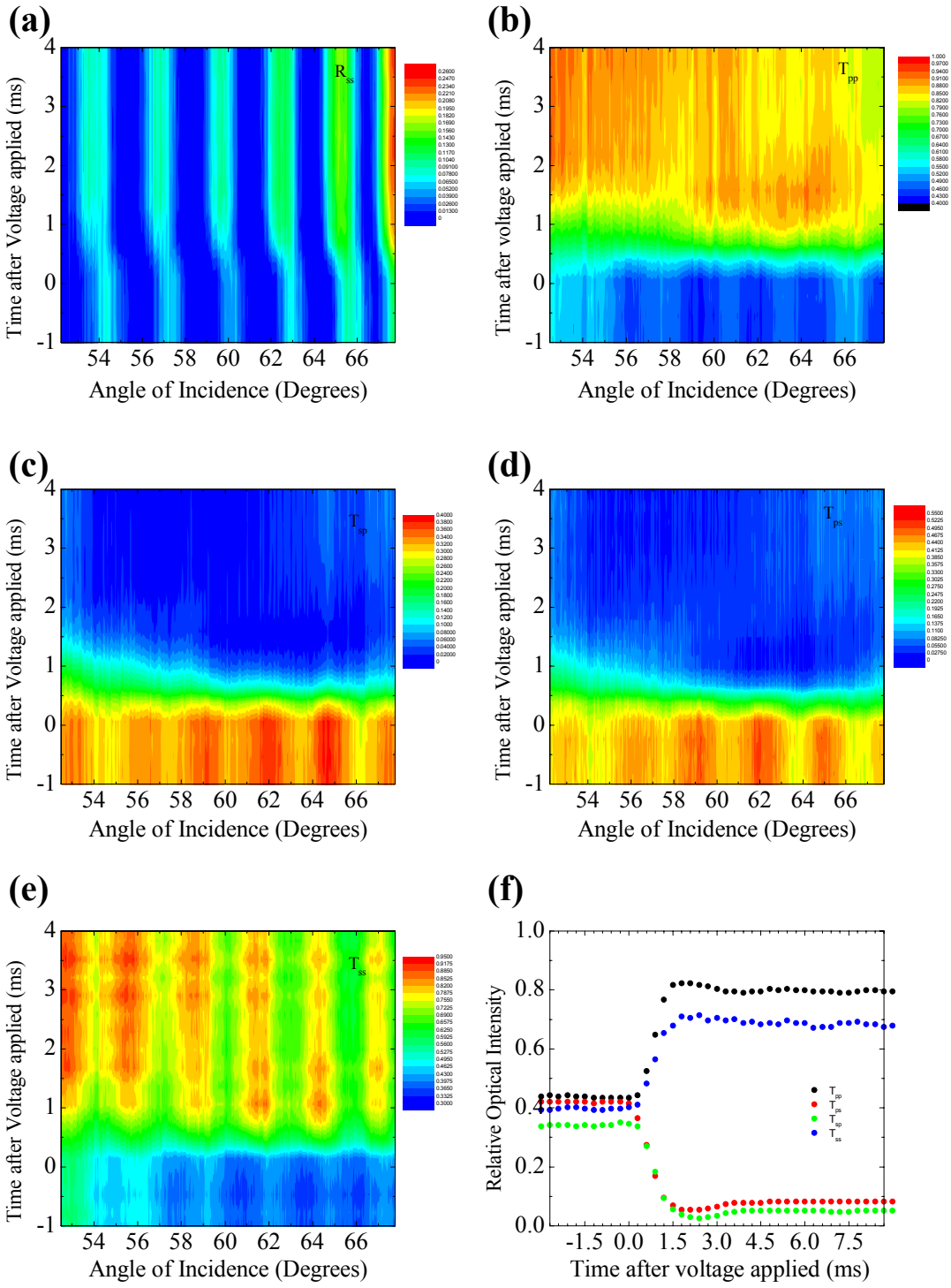

Fig. 7.2 **Variation of optical intensity vs. angle-of-incidence data with time for (a) R_{pp}; (b) T_{pp}; (c) T_{ps}; (d) T_{sp} and (e) T_{ss} data-sets and (e) variation in optical intensity with time at the pixel corresponding to a 60° angle of incidence.**

7.3.1 Measurement of static profiles

To obtain the cell substrate parameters and director profiles at 0V, 10 lines of optical data collected prior to the application of the voltage to the cell were averaged for each dataset to reduce the noise in the data. This data was then fitted using the multi-layer optics fitting routine. The same procedure was then followed to obtain the director profile at 7V by averaging a number of lines of data collected 10ms after the application of the voltage, by which time the reorientation of the director had stopped. The resulting optical permittivity, absorption and layer thickness parameters for the Silicon Monoxide, ITO and ZLI-2293 from these fits are shown in table 7.1. These values show good agreement with values previously measured for similar cells (e.g. chapters 4 and 8).

Optical Layer	ε_r	ε_i	Thickness
ITO	3.35 ± 0.05	$(0.1 \pm 0.04) \times 10^{-3}$	31 ± 2 nm
SiO_x	2.42 ± 0.01	$(1 \pm 0.1) \times 10^{-3}$	31 ± 2 nm
ZLI-2293 ($\varepsilon_\perp$)	2.274 ± 0.007	$(1.9 \pm 0.2) \times 10^{-5}$	4.63 ± 0.03 μm
ZLI-2293 ($\varepsilon_{\|\|}$)	2.78 ± 0.01	$(5.0 \pm 2.0) \times 10^{-4}$	

Table 7.1 Substrate parameters produced by fitting to the 0V and 7V optical data for the 5μm HAN cell measured during the switch-on process.

The static tilt profiles produced for 0V and 7V rms AC show good agreement with profiles generated using the free-energy minimisation modelling program, as discussed in chapter 3 (fig. 7.3). The elastic and dielectric constants used to produce these fits are K_{11} = 12.5 ± 0.2 pN; K_{33} = 17.9 ± 0.2 pN; $\varepsilon_{//}$ = 14.1 ± 0.1 and $\varepsilon_\perp$ = 4.1 + 0.1, and these show good agreement with the standard physical constants provided by Merck (K_{11} = 12.5 pN; K_{33} = 17.9 pN; $\varepsilon_{//}$ = 14.0 and $\varepsilon_\perp$ = 4.0 at 20°C).

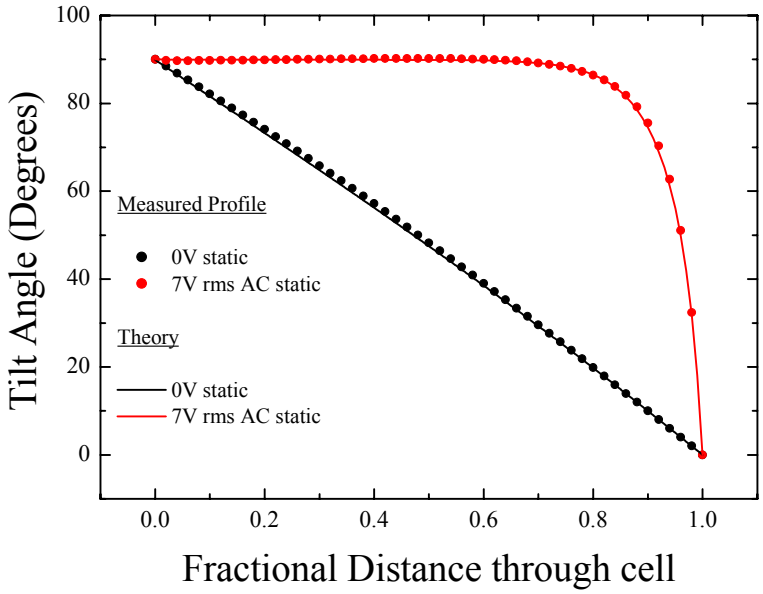

Fig. 7.3 **Measured 0V and 7V rms 10kHz AC static profiles (circles) and static tilt profiles produced using the parameters K_{11} = 12.5 ± 0.2 pN; K_{33} = 17.9 ± 0.1 ± 0.2 pN; $\varepsilon_{//}$ = 14.1 ± 0.1 and $\varepsilon_{\perp}$ = 4.1 + 0.1 in a free-energy minimisation modelling routine.**

7.3.2 Measurement of dynamic profiles

To obtain the intermediate director profiles produced as the director responds to the applied field, the lines of optical data collected during the switch-on process were normalised. The optical datasets for each time-step were then fitted to simultaneously, as in previous static studies, using a multi-layer optics fitting routine. The optical parameters for the ITO, SiO_x and liquid crystal were held constant at the values determined when fitting to the 0V and 7V data. To get a good starting point for the highly curved director profiles produced during the switch-on procedure, the nematodynamics modelling routine discussed in chapter 6 was used to produce a model profile for each time-step. A bezier curve was then fitted to each profile to ensure that the function was suitable for describing the complex form of the director, and to allow the starting values for the curve parameters required for the multi-layer optics fitting routine to be determined.

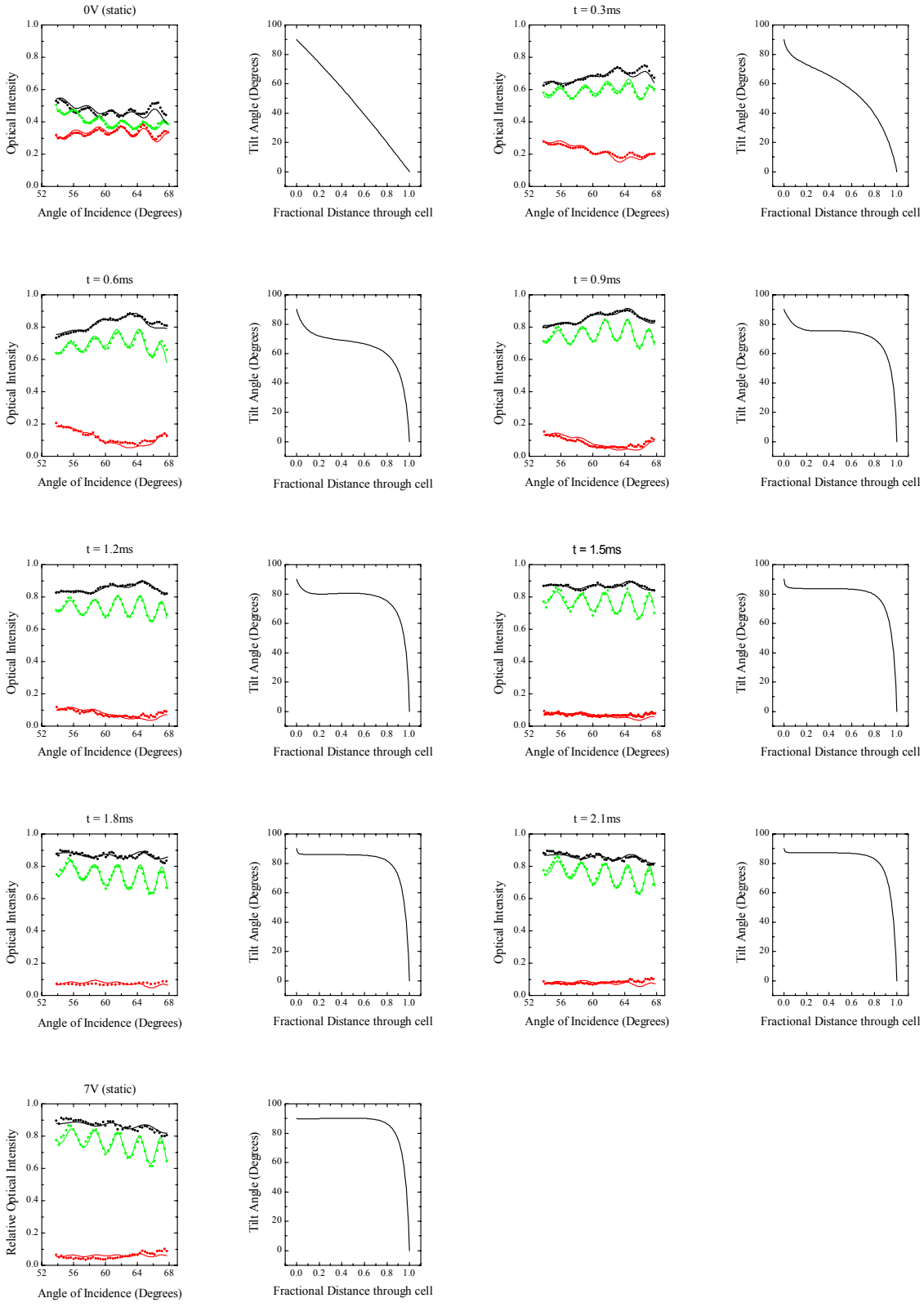

Fig. 7.4 **Measured (circles) and modelled (lines) optical intensity versus angle-of-incidence data for T_{pp} and T_{ss} polarisation conserving and T_{sp} polarisation converting signals. The resulting tilt profile is also shown.**

The fits produced to the optical data at each time step and the resulting tilt-profiles are shown in fig. 7.4. For clarity, only the T_{pp}, T_{ss} and T_{sp} data-sets are shown. It can be seen that the "best" agreements are seen between the measured and model data for the strong polarisation conserving signals for each time step. The polarisation converting signals were of much lower intensity and hence more affected by noise in the system.

The relatively long capture time of the system (required to allow good resolution of the shallow features in the optical data) also proved a factor in the quality of the data recorded. The rapid change in the director profile during the first couple of milliseconds in turn results in the optical data changing rapidly. The optical intensity vs. angle of incidence data recorded at the CCD array is an integral over the 0.3ms capture time.

7.3.3 Determination of viscosity coefficients

To obtain the viscosity coefficients of the material, the measured tilt-profiles were compared with model tilt-profiles generated using the nematodynamics modelling program. The best agreement between measured and model data, produced using the parameters in table 7.2, is shown in fig. 7.5. In both the measured and modelled tilt profiles, rigid anchoring at the two surfaces has been assumed. This is because the lack of reflectivity data makes determining the behaviour of the director at the homogeneous surface of the cell, particularly when the majority of the cell is homeotropically aligned, very difficult.

Miesowicz Coefficient	Measured Value
η_1	0.160 ± 0.005 Pa s
η_2	0.010 ± 0.005 Pa s
η_{12}	-0.100 ± 0.050 Pa s
γ_1	0.155 ± 0.005 Pa s

Table 7.2 Measured Miesowicz coefficients for ZLI-2293

These values show good agreement with values previously measured using a twisted nematic cell filled with ZLI-2293 (Smith et al, 2002).

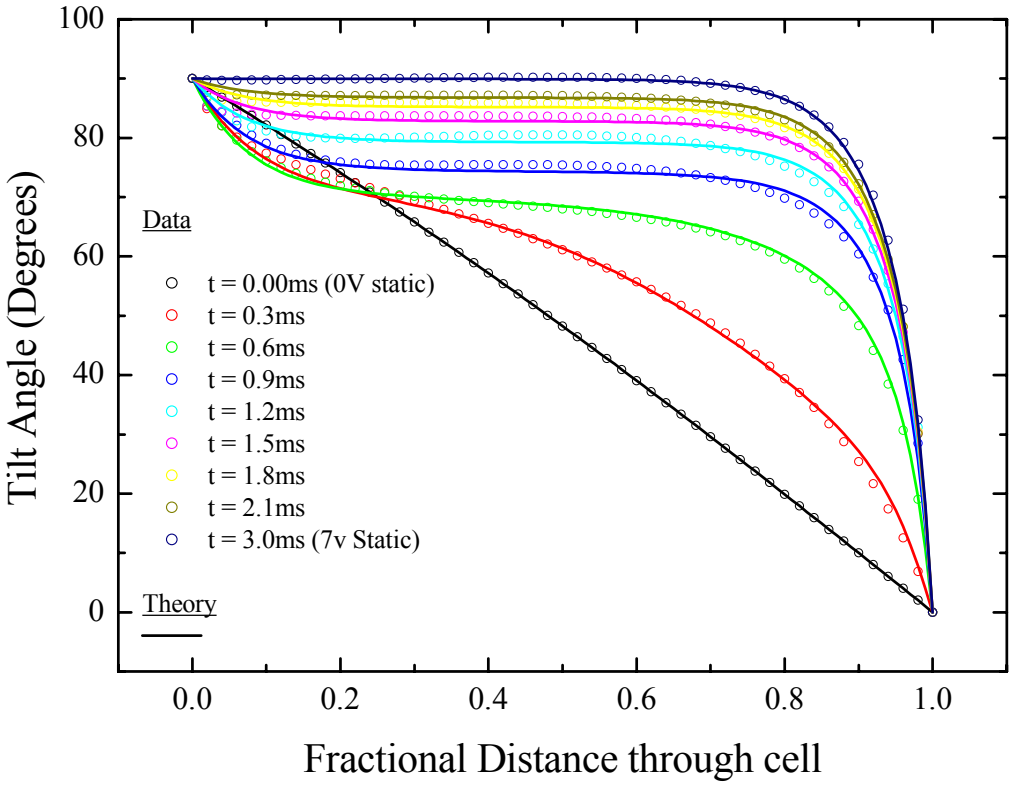

Fig. 7.5 Comparison between measured (circles) and modelled (solid lines) dynamic tilt profiles, using the viscosity coefficients given in table 7.2.

Backflow, as discussed in section 6.7, can clearly be seen occurring in the homeotropic region of the cell during the first 1.5ms after the voltage is applied. In this region, the torque exerted on the director due to the fluid motion in the "homogeneous" region of the cell causes the director tilt angle close to the homeotropic surface to first decrease, before rising up to the 90° tilt angle seen in the static 7V state. The influence of the viscosity coefficients on this phenomenon will now be discussed.

7.4 Analysis

To highlight the influence of each of the four viscosity coefficients required to characterise the switch-on dynamics of a HAN cell, the nematodynamics model has been used to model the effect of changing either η_1, η_2, η_{12} or γ_1 by ±5%, ±10% and ±15% with the other remaining coefficients held at their measured values. The results are shown in fig. 7.6.

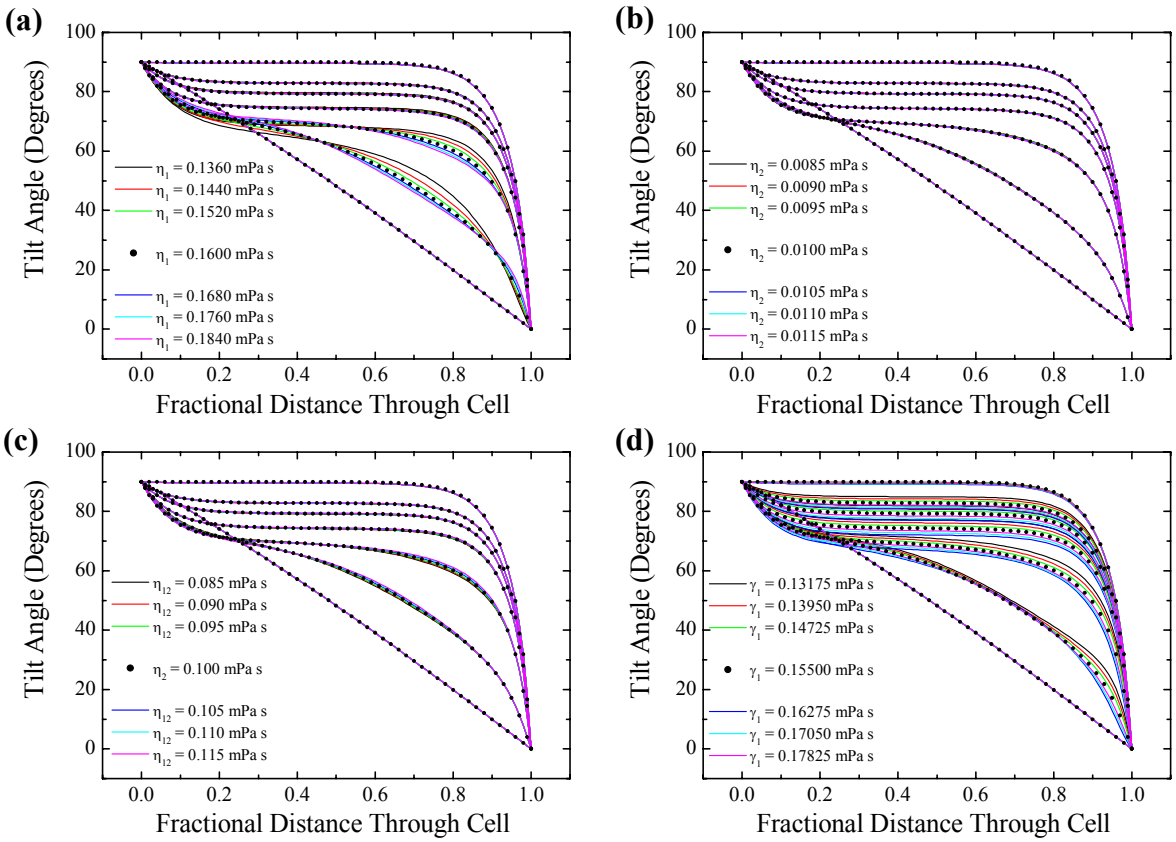

Fig. 7.6 Modelled dynamic tilt profiles at t = 0.3ms, 0.6ms, 0.9ms, 1.2ms 1.5ms and 6.0ms after a 7V rms 10kHz AC voltage is applied to a 5μm HAN cell. The result of changing (a) η_1 ; (b) η_2 ; (c) η_{12} and (d) γ_1 by ±5%, ±10% and ±15% is shown. Unless otherwise stated, the viscosity coefficients used are given in table 7.2.

This analysis shows that although the over-all switch-on time for the HAN cell is dominated by the rotational viscosity coefficient, γ_1, it is the shear viscosity coefficient η_1 which is most influential during the initial stages of the dynamic response, and hence influences the backflow in the first 1.5ms. This is to be expected as the viscosity coefficient η_1 describes the viscosity in the situation where the director is parallel to the flow gradient (fig. 6.1 (a)). This will therefore influence the backflow as the backflow region occurs between the homeotropic surface and the point where the flow gradient at time *t* is zero.

The overall response time appears to be almost entirely dependent on the rotational viscosity coefficient, γ_1, indicating that rotational (rather than shear) motion is the dominant process during the switch-on technique. It must be noted though that this analysis is very simplistic and only intended as a guide as certain rules apply to combinations of viscosity coefficients (see Appendix 1).

The remaining two shear viscosity coefficients, η_2 (director parallel to the flow direction) and η_{12} (stretch deformation around the director) have minimal influence on the tilt profiles and so it is not possible to accurately determine their values from this experiment.

7.5 Conclusions

The optical convergent beam technique has been used to study the switch-on dynamics of a HAN cell of thickness 4.62μm and filled with ZLI-2293 liquid crystal. The variation in the tilt profile was measured in 0.3ms time-steps as the director in the cell, originally at 0V, responded to the application of a 7V rms 10kHz voltage. Backflow was observed close to the homeotropic surface of the cell in the first 1.5ms of the cell transition, and the total switch-on time was found to be around 2.4ms.

Comparing the measured tilt profile at each time-step with model profiles produced using a nematodynamics model gave the viscosity coefficients of the material as η_1 = 0.160 ± 0.005 Pa s; η_2 = 0.010 ± 0.005 Pa s; η_{12} = -0.100 ± 0.050 Pa s and γ_1 = 0.155 ± 0.005 Pa s. However, further analysis of the variation in director profiles with different values for the viscosity coefficients showed that only η_1 and γ_1 had any significant effect on the switch-on process, with η_1 determining the shape of the backflow region during the first 1.5ms of the switch-on process, and γ_1 determining the over-all relaxation time.

In the following chapter, the form of the director as the cell relaxes from 7V rms AC to 0V will be measured, and comparisons will then be made between the response times and the influence of the viscosity coefficients in each case.

Chapter 8

Relaxation Dynamics of a ZLI-2293 Filled HAN Cell

8.1 Introduction

In the operation of a liquid crystal display device the time taken for the liquid crystal director to relax from an applied voltage tends to significantly exceed that of the switch-on time, and hence dictates the total switching time of the device. A good understanding of the relaxation process in a liquid crystal cell and the factors influencing the dynamic process are therefore required to enable progress in this field.

In this study, the convergent beam technique has been used to measure the changing director profile in a 5μm ZLI-2293 filled HAN cell when a 7V rms10kHz AC voltage is removed from the cell. The relaxation process has been measured in 0.3ms time-steps allowing the backflow occurring in the initial few milliseconds of the process to be directly observed. The measured tilt profiles have then been compared to model tilt profiles produced using the nematodynamics program discussed in chapter 6, and the influence of the four viscosity coefficients used in the model have been considered. Finally, the switch-off behaviour has been compared with that of the switch-on behaviour studied in the previous chapter, and the role of shear viscosity coefficient η_1 has been discussed in detail.

8.2 Experiment

A HAN cell was constructed using 5μm beads in UV setting glue as spacers and filled with the nematic liquid crystal compound ZLI-2293 (Merck). A 15nm layer of silicon monoxide obliquely evaporated at a 60° angle of incidence provided homogeneous alignment on one ITO surface, and a monolayer of Octadecyltrimethoxysilane on the other provided homeotropic alignment (fig. 8.1). A wire was attached to each ITO electrode with indium solder, and the cell was sealed using epoxy resin. The cell was mounted between two low-index hemispheres at a 60° azimuthal angle, and centred in the convergent-beam arrangement (see chapter 2) with the homeotropic surface as the incident face and the principal ray set at a 60° angle of incidence.

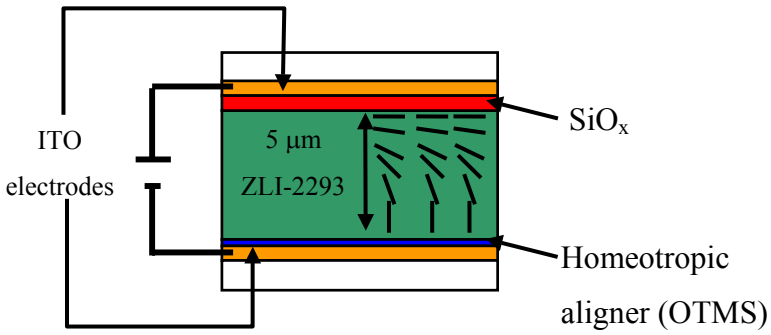

Fig. 8.1 Schematic diagram of the HAN cell used in the switch-off dynamics study.

The CCD array was set to a capture time of 0.3ms, as this was found to be the optimum capture time, allowing reasonable resolution of shallow features in the transmitted optical data whilst still allowing data to be captured on a time scale with minimal temporal interference between each line of data.

A 10 kHz AC 7V rms voltage was applied across the cell and optical intensity versus angle of incidence data was collected as the cell relaxed to the 0V state. Preliminary investigations showed that a total of 250 lines of data (75ms total capture time) was required to completely cover the relaxation of the cell. In addition, 30 lines of

data were collected prior to the voltage being removed to allow the initial static tilt profile to be obtained by averaging these lines.

In total, 5 datasets were collected, four transmitted (Tpp, Tps, Tsp and Tss) and one reflected (Rss). It was not possible to collect any other reflected datasets due to the low reflected signal intensity making it difficult to see any features in the data collected, let alone any changes when the voltage was removed. The data was then normalised, and seperated into individual time-slices to allow the data to be fitted to using the multi-layer optics fitting routine, as used previously in the static cases studied.

8.3 Results

The variation of the optical-intensity versus angle-of-incidence data with time for the five sets of data collected is shown in fig. 8.2 [(a)-(e)]. In each case, the angle of incidence is shown on the horizontal axis, and time after the voltage removed (in ms) is on the vertical axis. The colour at each point then denotes the intensity on a scale from 0 to 1.

Analysing this data qualitatively shows that, in the case of the four transmitted datasets, there are three distinct stages in the relaxation process. Initially there is an extremely rapid change in optical intensity in the initial few milliseconds. A large change in the position of the fully-leaky modes then occurs over the subsequent 20ms, and the modes then remain in roughly the same place, but change in amplitude over a further 50ms. These three stages can be illustrated by plotting the variation of intensity at the 67° angle of incidence pixel with time for each of the transmission datasets collected (fig. 8.2 (f)). In the case of the reflectivity data however the change in the data collected during the relaxation is much less dramatic. In the first ten milliseconds of the relaxation process there is a subtle shift in the location of the fully-leaky guided modes, but during the remainder of the relaxation process, no more change is observed.

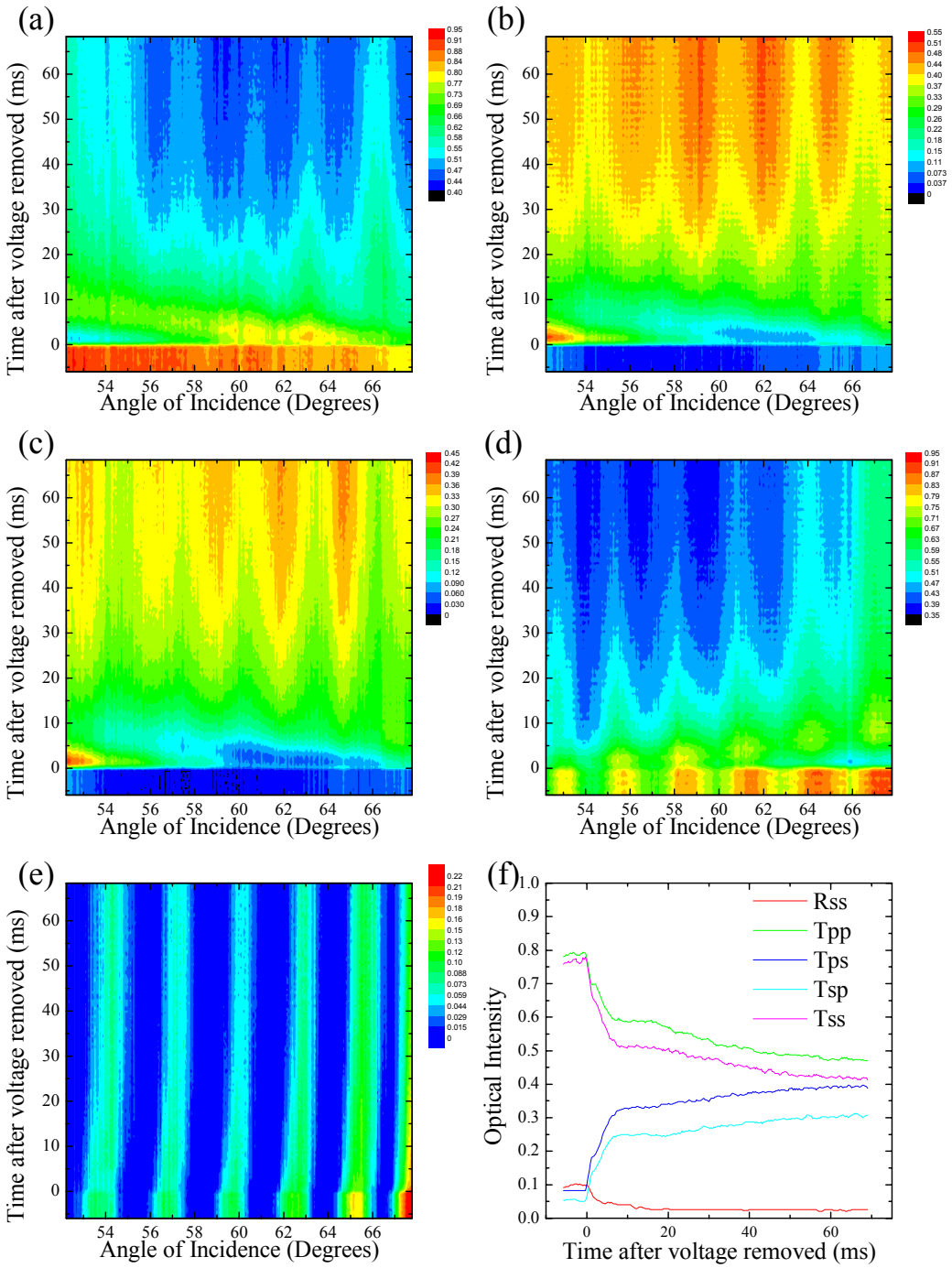

Fig. 8.2 **Variation of optical intensity vs. angle-of-incidence data with time for (a) T_{pp}; (b) T_{ps}; (c) T_{sp}; (d) T_{ss} and (e) R_{ss} data-sets and (f) variation in optical intensity with time at the pixel corresponding to a 67° angle of incidence.**

8.3.1 Fitting to optical data

To determine the evolution of the director profile during the relaxation process, all four lines of transmitted data for each timeslice were fitted simultaneously. The cell used for this study was the same as the one used previously for the switch-on study in chapter 7, and so the optical parameters used for the layers in the multi-layer optics fitting routine were the same as those shown in table 7.1. Fitting to the static tilt profiles at t = 0 (7V applied) and t = 70ms (0v) produced tilt profiles showing excellent agreement with model profiles produced by a free-energy minimisation static tilt profile model, as discussed in section 7.3.1.

To obtain the dynamic profiles, the relaxation of the cell from 7V was modelled using the nematodynamics program discussed in chapter 6. For each time slice, a bezier function was fitted to the modelled tilt profile using Microcal Origin 6.0 software, and the parameters produced were put into the fitting routine as the starting values for the multi-layer optical fit.

The result of fitting to a selection of lines of dynamic data are shown in fig 8.3. Fits to the T_{pp}, T_{ps} and T_{ss} data in each case are shown, along with the resulting tilt profile. The tilt profiles were produced by holding the optical parameters of the non-liquid crystal layers constant at the values shown in table 7.1. During the fitting procedure the cell thickness and liquid crystal optical permittivities were allowed to vary, although in practise they again remained at the values shown in table 7.1.

By comparing the evolution of the director profile with the changes occurring in each consecutive line of optical data, a clear correlation can be seen between the optical intensity recorded at each pixel of the CCD array and the form of the tilt profile.

(i) In the initial 1.2 ms after the voltage is removed, the tilt profile shows a rapid *decrease* in tilt angle in the region towards the homogeneous end of the cell, accompanied by an *increase* in tilt close to the homeotropic surface (i.e. backflow occurs and the director is moving away from the homeotropic alignment). Over this time period, all three optical datasets shown indicate a similarly rapid change in the intensity of light recorded at the lower angles of incidence. In the case of T_{pp} and T_{ss} this is a decrease in intensity, and for T_{ps}

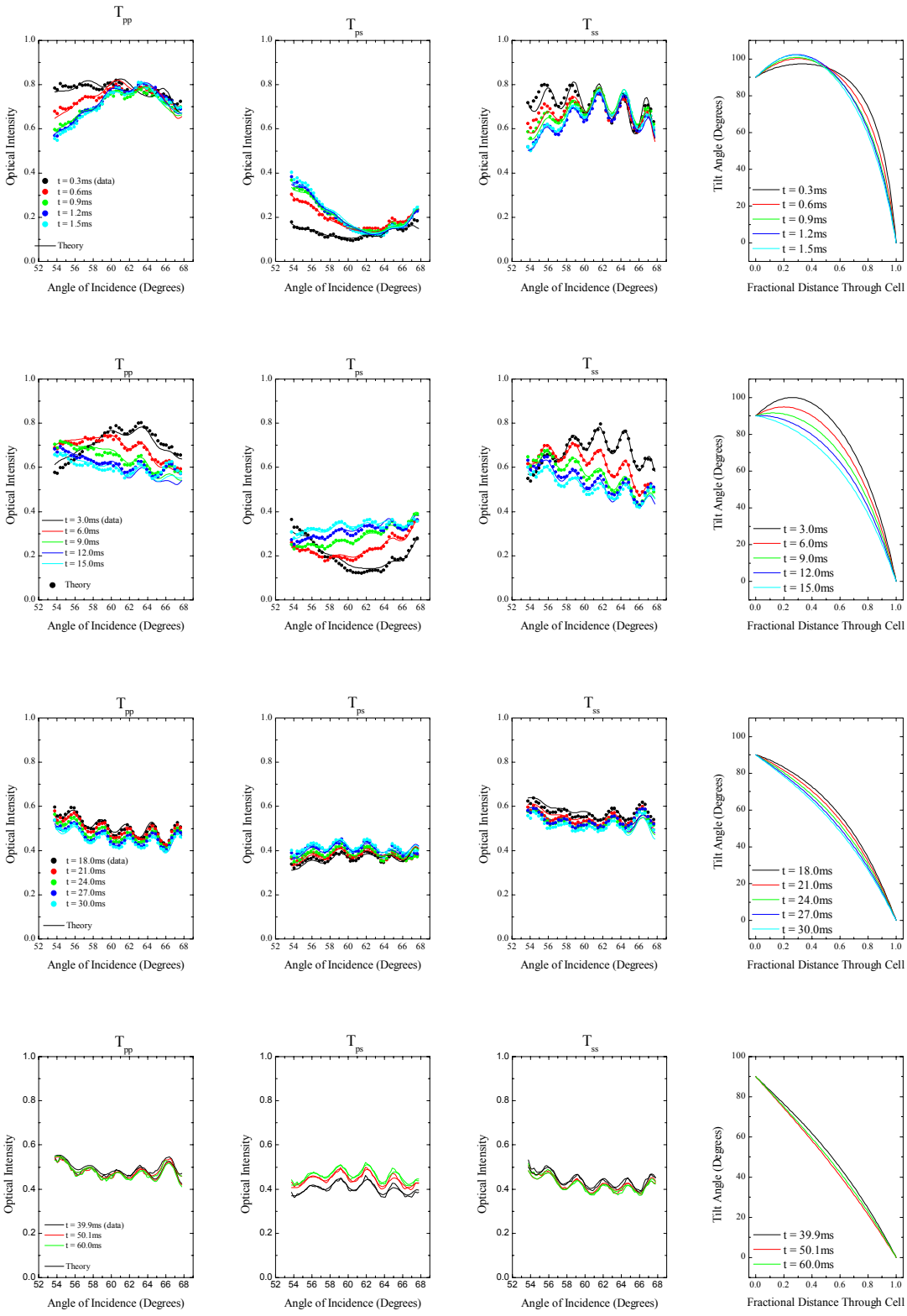

Fig. 8.3 **Measured (circles) and modelled (lines) optical intensity versus angle-of-incidence data for T_{pp} and T_{ss} polarisation conserving and T_{ps} converting signals. The resulting tilt profile is also shown.**

an increase. In all cases though, the intensity above ~ 62° angle of incidence shows little change.

(i) At around 1.5 ms, the backflow reaches its peak and for the time period 1.5ms – 9.0ms the director close to the homeotropic surface is still above 90° in places, but the tilt angle is now *decreasing* with time, and hence moving towards homeotropic alignment. Again, this is reflected in the behaviour of the optical data shown. The polarisation converting data now starts to *decrease* in intensity in the low angle of incidence region, whilst in the higher angle of incidence region there is a rapid increase in intensity. Similarly, in the case of the polarisation conserving data, the optical data in the lower angle of incidence range sees an *increase* in intensity with a rapid decrease in intensity at the higher angles of incidence.

(ii) Finally, after 9.0ms all regions of the cell are at tilt angles below 90° and relaxing towards the 0V alignment. This relatively uniform motion of the director is illustrated by the relatively uniform decrease in intensity of the transmitted polarisation conserving data, and increase in intensity of the polarisation converting data.

8.3.2 Comparison with modelled relaxation profiles

The result of comparing the measured tilt profiles to model tilt profiles produced using the viscosity coefficients given in table 7.2 are shown in fig. 8.4. As predicted by the modelling program produced in chapter 6, during the switch-off process backflow is clearly seen in the region adjacent to the homeotropically aligned surface. Excellent agreement is seen between the measured and modelled tilt profiles of the HAN cell.

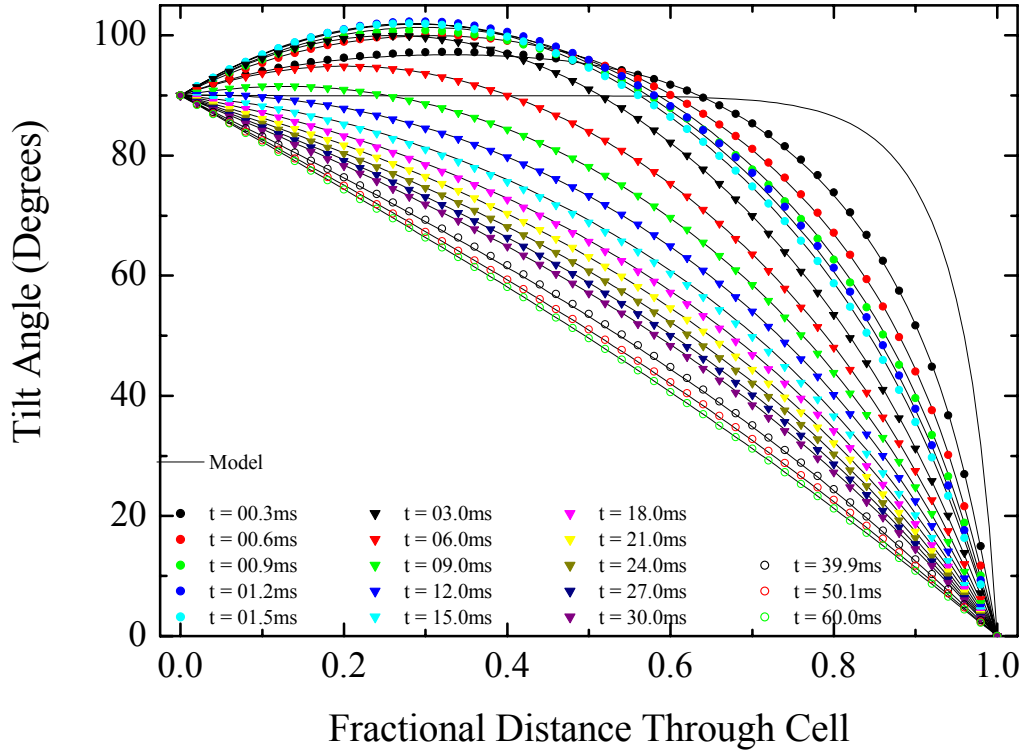

Fig. 8.4 **Comparison between measured profiles (symbols) and modelled profiles produced using the nematodynamics modelling program discussed in chapter 6, in conjunction with the viscosity parameters given in table 7.2.**

8.3.2 Analysis of the viscosity coefficients

The sensitivity of the dynamic profiles to each of the four coefficients involved in the dynamic relaxation of a HAN cell are illustrated in fig. 8.5. In each case, three of the viscosity coefficients η_1, η_2, η_{12} and γ_1 are held constant at the measured values given in table 7.2, and the fourth is varied by ±10% of its measured value. For clarity, only the profiles at 0.2ms, 1.0ms, 20.0ms and 70.0ms after the voltage is removed are shown.

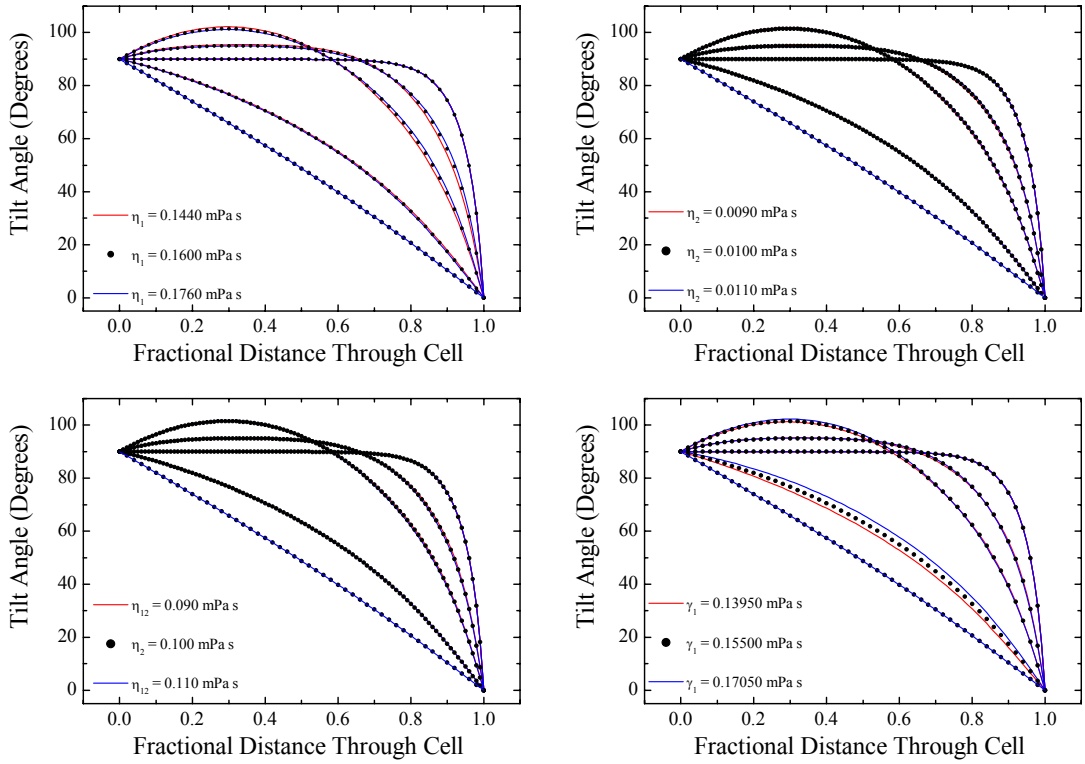

Fig. 8.5 **HAN cell tilt profiles at (i) t = 0, (ii) t = 0.2ms, (iii) t = 1.0ms, (iv) t = 20.0ms and (v) t = 70.0ms after a 10kHz AC 7V rms voltage is removed from a 5μm ZLI-2293 filled HAN cell. In each case, three of the viscosity coefficients η_1, η_2, η_{12} and γ_1 are held constant and the fourth is varied by ±10%.**

As in the case of the switch-on profiles, the coefficients η_2 and η_{12} appear to have no significant influence on the director profile during the relaxation process. (The reason for this is discussed in the next section.) However, the flow coefficient η_1 has a small influence on the shape of the director profile in the initial few milliseconds of the relaxation (but does not appear to influence the overall total relaxation time). In contrast, the rotational viscosity coefficient γ_1 has little influence on the actual shape of the director profile, but dictates the overall time taken to relax to the 0V state. These effects are highlighted in fig. 8.6 where the variation of the tilt angle with time at a fractional distance of 0.25 and 0.85 through the cell as shown. (These points were chosen as they correspond to the two points of maximum tilt-angle change during the backflow process.)

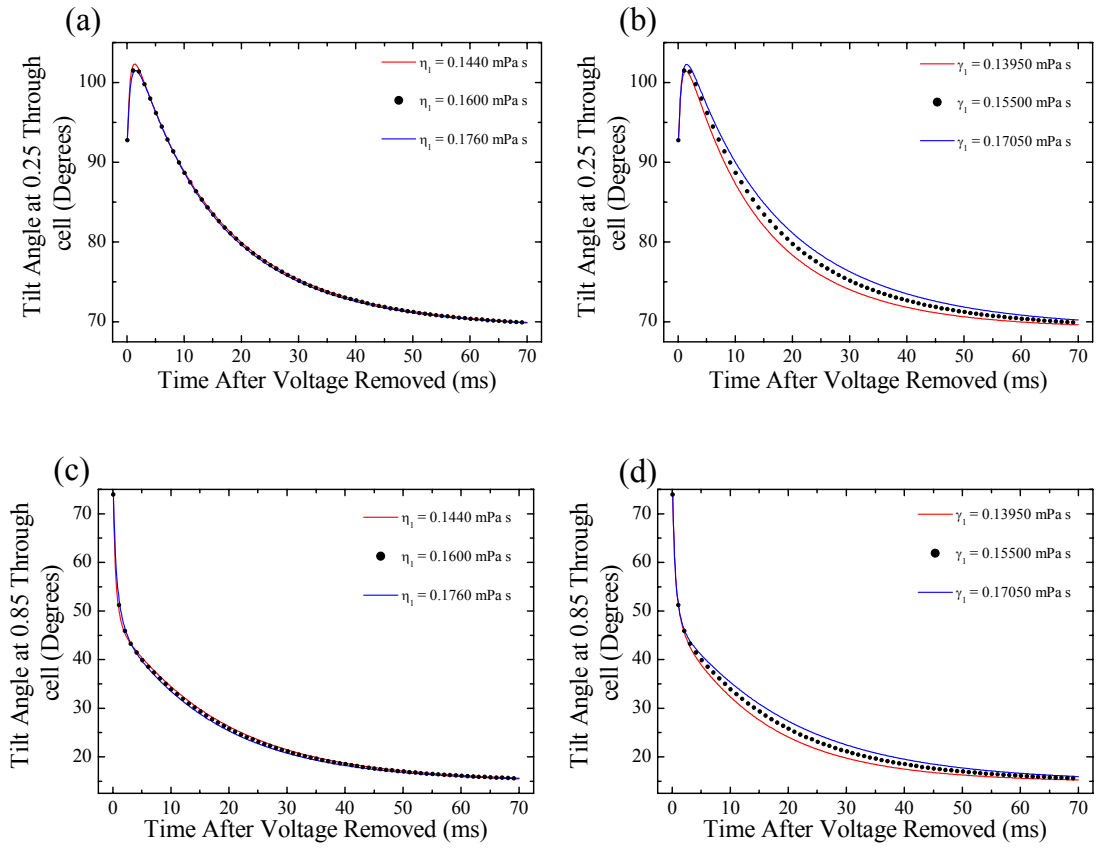

Fig. 8.6 Variation of tilt angle with time at a fractional distance of 0.25 [(a) and (b)] and 0.85 [(c) and (d)] through the cell. In each case, three of the viscosity coefficients have been held fixed at the values given in table 7.2, and the fourth has been varied by ±10% .

8.4 Comparison with switch-on

Apart from the obvious difference in total transition times, there are clear similarities between the switch-off dynamics of a HAN cell and the switch-on process discussed in the previous chapter. Crucially, measurement of the switch-on and switch-off director profiles agree with model profiles produced using the same viscosity coefficients. Most notably though, in both cases it is only the flow viscosity coefficient η_1 and the rotational viscosity coefficient γ_1 that have a significant influence on the form of the HAN cell director profile when responding to a change in applied voltage. The reason for the influence of η_1 can be understood when the coupling between the flow and director orientation is considered.

As discussed in chapter 6, η_1 is a measure of the viscosity in the situation where the director is perpendicular to the shear flow direction (the *x*-axis) and parallel to the viscosity gradient (the *z*- axis) as shown in fig. 8.7.

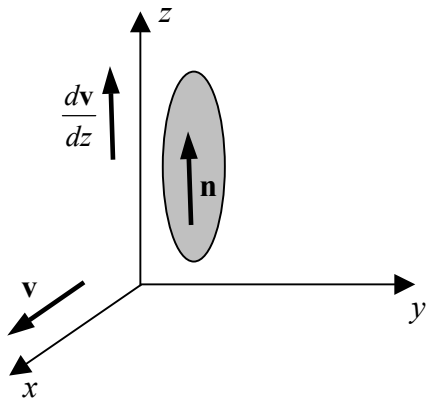

Fig. 8.7 Schematic diagram of the relative directions of the fluid flow, flow gradient and the director for the viscosity coefficient η_1.

In the case of a HAN cell containing material of a positive dielectric anisotropy, the director in the majority of the cell will be homeotropically aligned when a high voltage is applied, and so the influence of the coefficient η_1 on the dynamic properties is expected to be notable. In contrast, the coefficient η_2, relating to the viscosity where the director is parallel to the flow direction (i.e. along the *x*-axis in fig. 8.7) will have little influence on the dynamics. Similarly the viscosity coefficient η_{12}, which relates to a stretch deformation around the director, will have little effect.

To illustrate the effect of η_1 on the dynamic behaviour of a HAN cell, fig. 8.8 shows the velocity gradient through a 5μm HAN cell 0.2ms after a 7V rms 10kHz AC voltage is removed. In Fig. 8.8 (a) the values of η_1 have been adjusted by ±10% of the measured value, and the corresponding tilt profiles have been plotted for reference. It is interesting to note that the extrema of the flow gradient profiles coincide with the regions of maximum change in the regions of backflow. This is to be expected as these regions are the places of maximal rotational torque in the 1D HAN cell geometry, hence producing maximum rotation of the director. For comparison, graph 8.8 (b) shows the effect on the tilt profile and flow gradient profile when the coefficient η_2 has been adjusted by ±10% of the measured value. This viscosity coefficient is associated with a

direction perpendicular to the flow gradient, and so, as expected, has little influence on the velocity gradient.

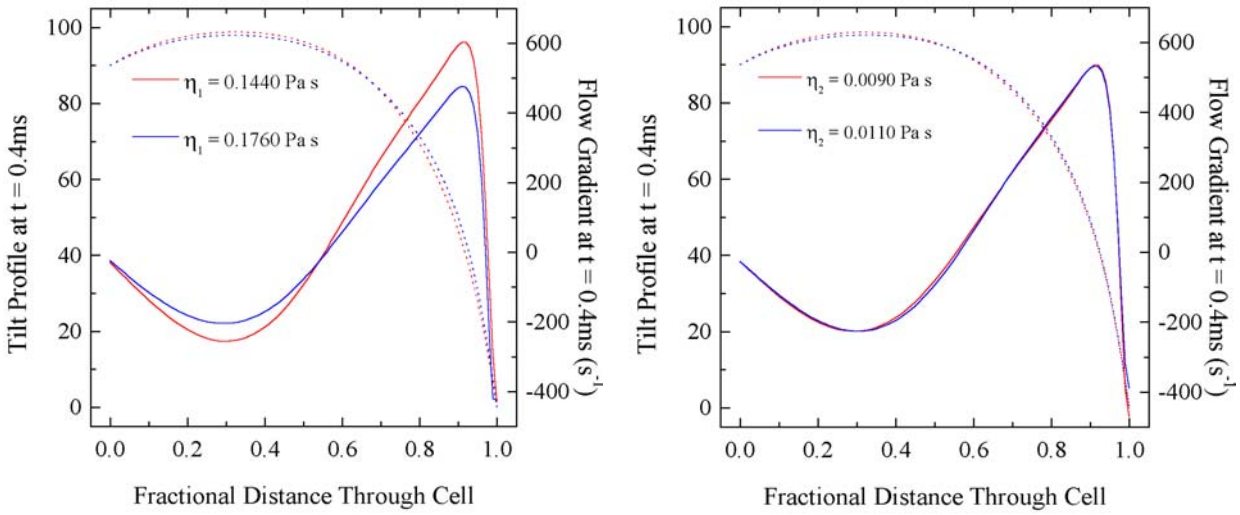

Fig. 8.8 **Illustration of the variation of flow gradient across a 5μm HAN cell 0.4ms after a 10kHz 7V AC voltage is removed when (a) η_1 and (b) η_2 are varied by ±10% of their "best" values. The tilt profiles are shown as dotted lines for reference.**

Although in both the switch-on and switch-off cases altering the viscosity coefficients does not appear to have a significant influence on the form of the director profile during the dynamic process, the mass flow of the material along the *x*-axis is crucial for the backflow to occur. The commercially available liquid crystal cell dynamics modelling package called DIMOS allows the dynamics of a cell to be modelled with or without flow being included in the calculation.

If this package is used to model the 7V switch-on and relaxation of a HAN cell using just the rotational viscosity coefficient (0.155 Pa s) the tilt profiles produced show a steady change in the director during the dynamic processes, with no backflow occurring (fig. 8.9 (a) and (c)). This is to be expected as it is the coupling between the rotation in the homogeneous region and the shear flow in an adjacent region which induces the backflow close to the homeotropic surface. When the change in the tilt angle at the centre of the cell with time is plotted for the rotation and rotation plus shear

flow modelling, it is clear that backflow makes the switching faster for both switch-on and switch-off.

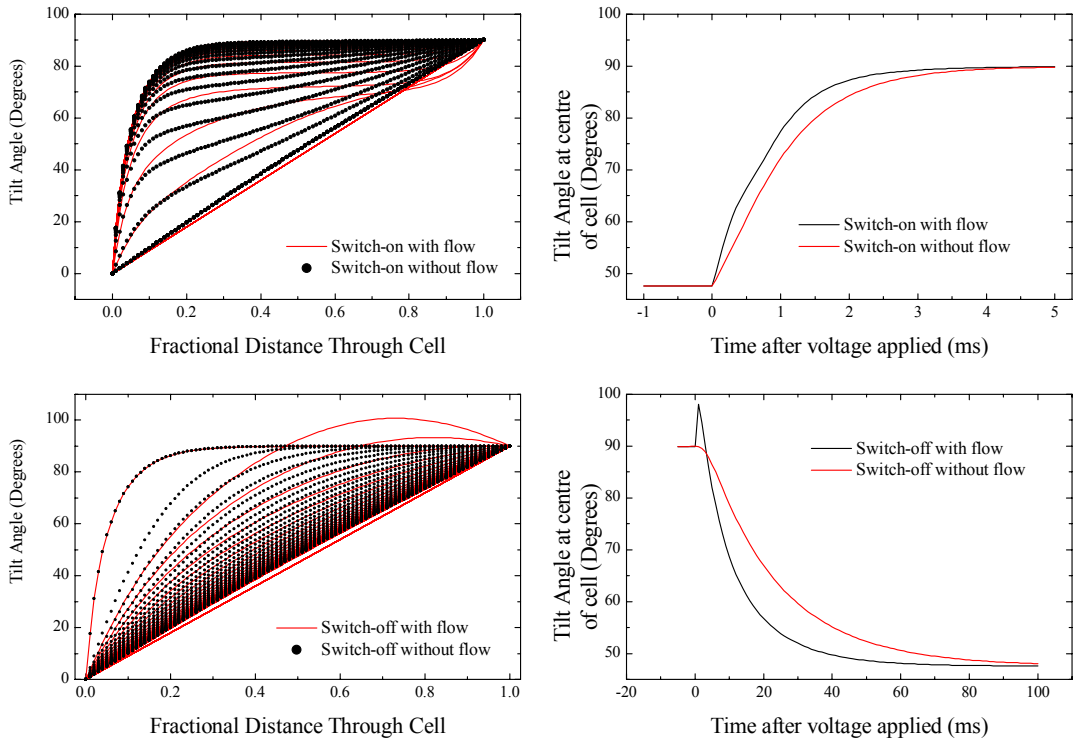

Fig. 8.9 **Switch-on (a) and switch-off (c) profiles for a HAN cell when rotational and rotational plus shear viscosities are considered. The variation of the mid-point tilt in the cell with time is also shown for the switch-on (b) and switch-off (d) cases indicating the total time taken for the dynamic responses.**

8.6 Conclusions

This study has used the convergent beam technique to measure the director profile in 0.3ms steps during the relaxation of a 4.6μm ZLI-2293 filled HAN cell from an applied 7V rms 10kHz AC voltage. The total relaxation time for the cell was 60ms, and, as predicted in chapter 6, the tilt profile exhibited backflow in the first 9ms after the voltage was removed.

The profiles measured show excellent agreement with model profiles produced using a nematodynamics modelling program, and the viscosity coefficients used agree with the values measured previously when studying the switch-on dynamics of a HAN cell. Further analysis has shown that the form of the backflow region of the cell is governed by the value of the shear viscosity coefficient η_1 and the overall relaxation time is determined by the rotational viscosity coefficient γ_1. A brief comparison has also been made with the switch-on dynamics of a HAN cell, and it has been shown that the occurrence of backflow in both situations (due to coupling between flow and rotational motion of the director) results in a faster response time than if rotation of the director alone is considered.

Chapter 9

Conclusions

9.1 Summary of Thesis

The aim of this thesis has been to explore the fundamental properties of nematic liquid crystalline materials by constructing hybrid aligned nematic cells and using optical waveguide techniques to measure the director profile in both static and dynamic situations.

The HAN geometry was chosen for two reasons. Firstly, the high bend and splay elastic distortion present in the cell results in a thresholdless response to applied voltages. Therefore, the director is highly sensitive to the application of small electric fields applied perpendicular to the substrate, and by measuring these distortions, physical parameters of the liquid crystal can be determined. Secondly, the HAN geometry is of commercial interest as it forms one of the two stable states in the Zenithal Bistable Device. This type of low power consumption device is set to become a key factor in the new generation of portable liquid crystal displays.

The first chapter of this thesis gives a general introduction to the liquid crystalline state of matter, before concentrating on properties specifically associated with nematic liquid crystals. A brief account of the various surface alignment techniques used in different studies discussed in subsequent chapters is given along with a description of the method used to assemble test cells. The optical properties of a twisted cell are derived to illustrate the optical properties behind conventional liquid crystal displays. The dielectric and optical properties of a HAN cell is then discussed in detail. The chapter concludes with a description of the operation of the Zenithal Bistable Device to highlight the importance of the HAN geometry commercially.

Chapter 2 is concerned with the optical techniques used to probe the director structure in the test cells produced. An introduction to optical waveguides is given along with an overview of the different waveguide techniques previously used to characterise liquid crystal cells. The fully-leaky waveguide technique, used to study static director profiles, is then discussed in detail. Finally, the latest waveguide technique developed, known as the convergent beam technique and used to investigate liquid crystal dynamics on the sub-millisecond timescale, is described.

The remainder of the thesis is divided into two sections, the first considering static properties of the HAN cell director, and the second focussing on the dynamics of the cell when there is a change in the applied voltage.

The influence of flexoelectricity in liquid crystal structures (analogous to the piezoelectric effect in solids) is introduced in chapter 3. To highlight the importance of its apparently subtle effect on the director profile in a HAN cell, its role in two devices, (the ZBD display and a polarisation rotator) is discussed. The continuum theory has then been used to derive an expression for the static equilibrium structure of a hybrid aligned nematic cell at an applied voltage when the flexoelectric contribution to the free-energy is considered. This has formed the basis of a program developed to model the director profile in a HAN cell at applied fields. The effect of varying the flexoelectric coefficients on the director profile and the internal fields produced within the cell have subsequently been modelled.

Chapter 4 describes a fully-leaky guided mode study performed to measure the director profile in a HAN cell when low voltages were applied. Firstly, a qualitative analysis of the influence of ionic contaminants from the aligning layers used was performed. It was found that rubbed polyimide was unsuitable for use in these low voltage situations as ionic contaminants caused the applied DC fields to be reduced over the duration of the applied pulse. However, obliquely evaporated silicon monoxide produced no such effect. The sum of the splay and bend flexoelectric coefficients of E7 was then measured by applying forward and reverse bias DC voltages of magnitudes up to 1.5V and measuring the director profile in each case. This study found that the resulting profiles were dependent not only on the flexoelectric coefficients, but also the presence of surface polarisation at the

homeotropic aligning layer. The origin of this polarisation was found to be due to a preferential alignment of the dipolar liquid crystal molecules at the homeotropic surface. This study also highlights the sensitivity of the fully-leaky waveguide technique to very subtle changes in the director profile.

Chapter 5 is a further experimental chapter investigating the static director profile in a HAN cell filled with a nematic material of a negative dielectric permittivity. In this case a fully-leaky waveguide structure was used in conjunction with a polarimeter to measure the Stokes' parameters of light transmitted through the structure as a function of angle of incidence when high frequency AC voltages were applied. From this information, the director profiles were determined, and the anchoring energy at the homogeneous surface was calculated.

The dynamics section of this thesis commences in chapter 6 with the theory behind the dynamical response of the director in a HAN cell to changes in applied fields. Initially, the fluid mechanics associated with an isotropic fluid is considered, and the Leslie-Eriksen-Parodi theory of nematodynamics for anisotropic materials is then introduced and the added degrees of complexity due to the use of five viscosity coefficients are highlighted. The nematodynamics equations specifically relating to a HAN geometry have then been derived, and an account of their use in a nematodynamics modelling program produced has been given. This program was then used to model the director profile and shear flow on the millisecond time-scale when AC and DC voltages are applied to, and removed from, a HAN cell.

A convergent beam experiment performed to measure the switch-on dynamics of a ZLI-2293 filled HAN cell is described in chapter 7. The total switch-on time when a 7V 10kHz AC voltage was applied across the cell was measured as around 2.4ms, and the tilt profile was recorded in 0.3ms time steps. This time resolution was sufficient to allow backflow occurring in the first millisecond of the switching process to be observed. Good agreement was found with predicted model profiles produced by the nematodynamics modelling program, and the viscosities of the liquid crystal were determined.

The switch-off dynamics of a ZLI-2293 filled HAN cell were studied in chapter 8. Measurements were taken on a 0.3ms timescale using the convergent beam technique, and the relaxation process was found to take around 60ms. This dynamic

switching again exhibited backflow during the initial response of the cell, and was in agreement with model profiles produced by the dynamics modelling program. A comparison was made between the switch-on and switch-off dynamics, and it was found that in both cases, the shape of the director profile during the initial backflow of the cell was primarily determined by the shear viscosity coefficient η_1 and the overall response time is characterised by the rotational viscosity coefficient γ_1.

9.2 Further Work

Due to its previous lack of practical applications, up until now the HAN geometry has received relatively little attention. As a result there are many areas that can be explored further to improve the understanding of both the dynamic and static properties of this geometry.

For the static HAN geometry, the surface anchoring and the surface flexoelectric effect (Sonin, 1995) are still to be explored in detail. Although the fully-leaky technique used here has proved to be particularly sensitive to the director in the bulk of the cell, the use of the fully-guided technique, where the liquid crystal is contained within a metal-clad waveguide allows the surface physics of a cell to be explored in great detail. This method would therefore be ideally suited to measuring the anchoring strength at the surface. This could ultimately then be combined with the convergent beam technique to allow the surface dynamics during switching to be explored in previously unseen detail.

The high sensitivity of the optical waveguide technique to subtle changes in the director profile makes the convergent beam system an ideal tool for determining the influence of flexoelectricity during the switch-on and switch-off processes of the HAN cell when low voltage dc pulses are applied. In particular, the role of flexoelectricity in the director profile when switching between forward and reverse bias dc biases, as modelled in chapter 6, could be observed. This is ultimately of great importance to the understanding of the switching process involved in the zenithal bistable device, as discussed in chapter 3.

The use of the HAN geometry in conjunction with a cholesteric liquid crystal is another area which has great potential, but has received little attention so far (Lewis and Wiltshire, 1987). By adding a chiral dopant to the nematic material contained in a HAN structure, the director both tilts and twists through the cell. However, as the azimuthal twist is undefined at the homeotropic surface, the twist through the cell is unconstrained by the surfaces, as is the case in a twisted nematic structure. This therefore allows the material to adopt its natural pitch at any temperature. This change in pitch with temperature could be readily studied using the static fully-leaky guided-mode technique. The dynamics of this structure would also be of great interest due to possible backflow effects arising not only from the tilt alignment, but also the twist.

Finally, another area of great interest is the use of the HAN structure filled with a "dual frequency" liquid crystalline material. These compounds have a positive dielectric anisotropy when an AC field in one particular range of frequencies is applied, and a negative dielectric anisotropy over another frequency range. These materials therefore have the potential for fast switching as the director can be "driven" by an applied field to both the field-on state, and more importantly, the field-off state, greatly reducing the normal relaxation time associated with liquid crystals. The high data capture speed of the convergent beam system makes it extremely suitable for studying this type of structure, which could ultimately be used in display devices.

These suggestions of further areas of study have considered applications specific to the HAN geometry. However, the high sensitivity of the FLGM technique to subtle changes in the director profile makes it suitable for studying a vast array of cell geometries and new liquid crystal materials. Similarly, the fast capture time of the convergent beam technique can allow the dynamics of a director profile to a multitude of voltage pulses to be studied in exceptional detail.

9.3 Publications and Presentations

9.3.1 Publications

1. "*Fully Leaky Guided Mode Study of the Flexoelectric Effect and Surface Polarisation in HAN Cells*", SA Jewell and JR Sambles, J. Appl. Phys. **92**, 1, 19-24 (2002)

2. *"Fully-Leaky Guided Mode Measurement of the Flexoelectric Coefficient (e_{11}+e_{33}) in a Hybrid Aligned Nematic Liquid Crystal Cell"*, SA Jewell and JR Sambles, Mol. Cryst. Liq. Cryst., **(to be published)**

3. "*Backflow In The Relaxation Of A Hybrid Aligned Nematic Cell*", SA Jewell and JR Sambles, Appl. Phys. Lett. **(to be published)**

9.3.2 Oral Presentations

1. *"The Flexoelectric Effect in HAN Cells"*, BLCS 2001, March 2001, University of Oxford, UK

2. *"Driven Bananas with HAN Cell Dynamics",* Rank Symposium, May 2001, Grasmere, UK

3. *"Optical Convergent Beam Measurement of HAN Cell Relaxation Dynamics",* Invited Talk, BLCS 2002, March 2002, London

9.3.3 Poster Presentations

1. "*Determination of the Director Profile Within a HAN Cell Using Fully-Leaky Guided-Modes*", BLCS 2001, March 2000, University of Strathclyde, UK.

2. *"Fully-Leaky Guided Mode Measurement of the Flexoelectric Coefficient (e_{11}+e_{33}) in a Hybrid Aligned Nematic Liquid Crystal Cell"*, Anglo-Japanese Symposium on Liquid Crystals, September 2001, York, UK.

3. *"Optical Convergent Beam Measurement of HAN Cell Relaxation Dynamics",* International Liquid Crystal Conference 2002, July 2002, Edinburgh, UK.

Adam, CJ, Clark, SJ, Ackland, GJ and Crain J	1997	"Conformation Dependent Dipoles of Liquid Crystal Molecules and Fragments from First Principles", *Phys Rev E* **55,** 5641
Anzelius, A	1933	*Uppsala Univ. Arsskr. Mat. Naturv.*, **1**
Azzam, RMA and Bashara, NM	1996	"*Ellipsometry and polarized light*", Elsevier Science, The Netherlands
Bahadur, B	1990	"*Liquid Crystals Applications and Uses, Vol. 1"*, World Scientific, Singapore
Barnes, WL	1986	"*Guided optical waves in Langmuir-Blodgett films of 22-tricosenoic acid*", Ph.D. Thesis, University of Exeter, UK
Berreman, DW	1975	"Liquid Crystal Twist Cell Dynamics with Backflow", *J. Appl. Phys*. **46** (9) 3746
Billeter, JL and Pelcovits, RA	2000	"Molecular Shape and Flexoelectricity", *Liq. Cryst*. **27**, (9), 1151
Blinov, LM, Ozaki M and Yoshino K	1999	"Flexoelectric Polarization in nematic Liquid Crystals Measured by a Field on-off Pyroelectric Technique", *JETP Letters* **69**, (3) 236
Born, M and Wolf, E	1999	"*Principles of Optics*", 7th edition, Cambridge University Press, UK

Bryan-Brown, GP, Wood, EL, Brown, CV, Jones, JC, Sage, IC and Brett, P	1997	"Grating Aligned Bistable Nematic Device", *Proceedings of International Displays Workshop (IDW), Nagoya, Japan*, **PLC2-1**, pp261
Chandresekhar, S	1992	"*Liquid Crystals*", (2nd Edition), Cambridge, UK
Clark, NA, Maclennan, JE, Handschy, MA and Meadows, MR	1990	"Director Reorientation Dynamics In Chevron Ferroelectric Liquid-Crystal Cells"**,** *Liq. Cryst*. **7**, (6) 753
Collings, PJ and Hird, M	1998	"*Introduction to Liquid Crystals – Chemistry and Physics*", Taylor and Francis, London.
Davidson, AJ and Mottram, NJ	2002	"Flexoelectric Switching in a Bistable Nematic Device", *Phys. Rev. E*., **65,** Art. No. 051710
De Gennes, PG	1974	"*The Physics Of Liquid Crystals*", Clarendon, Oxford
De Jeu, WH	1980	"*Physical Properties of Liquid Crystalline Materials*", Gordon and Breach, London
Denniston, C and Yeomans, JM	2001	"Flexoelectric Surface Switching of Bistable Nematic Devices", *Phys. Rev. Lett*. **87**, (27) art. No. 275505
Dlugunovich, VA, Snopko, VN and Tsaryuk, OV.	2001	"Analysis of a Method for Measuring Polarization Characteristics with a Stokes Polarimeter Having a Rotating Phase Plate," *J. Opt. Technol.* **68** (4) 269

Dozov, I, Martinot-Lagarde, Ph and Durand, G	1982	"Flexoelectrically Controlled Twist of Texture in a Nematic Liquid Crystal", *J. Phys. Lett*. **43** L-365
Elston, S and Sambles, R	1998	"*The Optics of Thermotropic Liquid Crystals*", Taylor and Francis, UK
Elston, SJ, Sambles, JR and Clark, MG	1989	"Determination Of The Director Alignment In A Ferroelectric Liquid-Crystal Device By Observation Of Optical Modes", *J. Mod. Opt.,* **36**, (8) 1019
Eriksen, JL	1961	"Conservation Laws for Liquid Crystals", *Trans. Soc. Rheol*., **5**, 23
Eriksen, JL	1962	"Hydrostatic Theory of Liquid Crystals", *Arch. Ration. Mech. Anal.,* **9,** 371
Franck, FC	1958	"On the theory of Liquid Crystals", *Discuss. Faraday Soc*., **25**, 19
Friedel	1922	*Ann. Physique,* **18,** 273
Goldstein, H	1980	"*Classical Mechanics*", (2nd Edition) Addison-Wesley, UK
Hallam, BT, Yang F and Sambles, JR	1999	"Quantification of the Azimuthal Anchoring of a Homogeneously Aligned Nematic liquid crystal Using Fully-Leaky Guided Modes", *Liq. Cryst*. **26**, 5
Harris JH, Shurbert R and Pelky JN	1970	J. Opt. Soc. Am., **60**, 1007

Hecht, E	1987	"*Optics*", Addison-Wesley, USA
Hodder, B, Yang, F and Sambles, JR	2001	"Optical Characterisation of the Director Profile in a Ferroelectric Liquid Crystal Cell with Homeotropic Alignment", *J. Appl. Phys*. **89**, 1
Huard, S	1997	"*Polarization of Light*", Wiley, Paris
Ito, N, Sakamota, K, Arafune, R and Ushioda, S.	2000	"Relation between the molecular orientations of a very thin liquid crystal layer and an underlying polyimide film", *J. Appl. Phys*. **88** (6) 3235
Jones JC, Brett, P, Bryan-Brown, GP, Graham, A and Wood, EL	2000	"Zenithal Bistable Displays", *Proceedings of Electronic Information Display Conference*, November 2000, London, UK
Kitson, SC and Geisow, A	2002	"Controlable Alignment of Nematic Liquid Crystals Around Microscopic Posts: Stabilization of Multiple States", *Appl. Phys. Lett.* **80** (19) 3635
Ko, DYK and Sambles, JR	1988	"Scattering Matrix Method for Propagation in Stratified Media", *J. Opt. Soc. Am. A*., **5**, 1863
Kuhnau U, Petrov AG, Klose G et al	1999	"Measurements of Anchoring Energy of a Nematic Liquid Crystal 5CB on Langmuir-Blodgett Films of DPPC", *Phys Rev E Part A* **59**, 578
Landau, LD and Lifshitz, EM	1959	"*Fluid Dynamics*", Pergamon, Oxford

Lavers CR and Sambles JR	1990	"Use of Mode Mixing to Determine the Optic Tensor Configuration of a Thin Ferroelectric Liquid Crystal Layer", *Liq. Cryst*. **8**, 577
Lavers CR and Sambles JR	1991	"An Examination of an Optical Dielectric Tensor of a Liquid Crystal Waveguide", *Ferroelectrics*, **113,** 339
Lehmann, O	1890	Z. Krist. **18**, 464
Leslie, FM	1966	"Some Constitutive Equations for Anisotropic Fluids", *Q. J. mech. Appl. Math.,* **19**, 357
Leslie, FM	1968	"Some Constitutive Equations for Liquid Crystals", *Arch. Ration. Mech. Anal*., **28**, 265
Lewis, MR and Wiltshire, MCK	1987	"Hybrid Aligned Cholesteric: A Novel Liquid Crystal Alignment", *Appl. Phys. Lett*. **51**, (15), 1197
Marcerou, JP and Prost, J	1980	"The Different Aspects of Flexoelectricity in Nematics", *Mol. Cryst. Liq. Cryst*., **58**, 259
Maugin, M Ch	1911	"Sur Les Cristaux Liquides de Lehmann", *Bull. Soc. Fran. Min.* **34**, 6
Mazulla A, Ciuchi F and Sambles JR,	2001	"Optical Determination of Flexoelectric Coefficients and Surface Polarization in a Hybrid Aligned Nematic cell", *Phys. Rev. E.* **64**, (2): art. no. 021708

Meyer, RB	1968	"Piezoelectric effects in liquid crystals", *Phys. Rev. Lett*. **22**, 918
Murakami, S, Naito, H, Okuda M and Sugimura A	1995	"Transient Photocurrent in Amorphous Selenium and Nematic Liquid Crystal Double Layers", *J. Appl. Phys*. **78**, (7), 4533
Murthy, PM, Raghunathan, V and Madhusudana, P	1993	"Experimental Determination of the Flexoelectric Coefficients of Some Nematic Liquid Crystals", *Liq. Cryst*. **14** (2) 483
Musgrave, B, Lehmann P and Coles HJ	1999	"A New Series of Chiral Nematic Bimesogens for the Flexoelectro-optic Effect", *Liq. Cryst*. **26**, (8), 1235
Newton, CJ and Spiller, T	2001	Private communication on the subject of mathematical functions suitable for use when modelling director profiles.
Parodi, O	1970	"Stress Tensor for a Nematic Liquid Crystal", *J. Phys. (Paris),* **31**, 581
Ponti,S, Ziherl, P, Ferrero, C and Zumer, S	1999	"Flexoelectro-optic effect in a hybrid nematic liquid crystal cell", *Liq. Cryst.* **26**, 1171
Prost, J and Marcerou, JP	1977	J. de Physique (Paris), **38**, 315
Rapini, A and Papoular, MJ	1969	"Distortion d'une Lamelle Nématique Sous Champ Magnétique Conditions d'Ancrage Aux Parois *", J. Phys. Colloq*. **30** (C4) 54

Raynes, EP	1991	"*Electro-optic Effects in Liquid Crystals. From Electronic Materials – From Silicon to Organics"*, Ed. L.S. Miller and J.B. Mullin, Plenum Publishing Corporation.
Reinitzer, F	1888	*Montash Chem* **9**, 421
Ruan, L and Sambles, JR	1995	"Guided-Wave Study Of Electroclinic Effects In A Homogeneously Aligned Smectic-A Liquid-Crystal", *Liq. Cryst*. **19** (1) 133
Rudquist, P	1997	"*The Flexoelectro-optic Effect in Cholesteric Liquid Crystals*", Ph.D. Thesis, Chalmers University of Technology, Goteborg.
Rudquist, P and Lagerwall, ST	1997	"On the Flexoelectric Effect in Nematics", *Liq. Cryst*. **23**, (4) 503
Schadt, M and Helfrich, W	1971	"Voltage Dependent Optical Activity of a Twisted Nematic Liquid Crystal", *Appl. Phys. Lett. Technol*., **11**, 32
Smith, NJ	2001	"*Convergent Beam Waveguide Studies of Liquid Crystal Cells*", PhD. Thesis, University of Exeter
Smith, NJ and Sambles, JR	2000	"Optically Resolving Dynamic Processes in Commercial Liquid Crystal Cells", *Appl. Phys. Lett*. **77**, 2632
Smith, NJ, Sambles, JR and Tillin MD	2002	"Direct optical quantification of backflow in a 90° Twisted Nematic Liquid Crystal Cell", *Phys. Rev. Lett*. **88**, 8

Sonin, AA	1995	"*The Surface Physics of Liquid Crystals*", Gordon and Breach Publishers, Luxembourg.
Sugimura H, Hayashi K, Saito N, Takai O and Nakagiri N	2001	"Kelvin Probe Force Microscopy Images of Microstructured Organosilane Self-Assembled Monolayers", *Jpn. J. Appl. Phys. Part 1*, **40** 4373
Takahashi T, Hashidate S, Nishijou H et al	1998	"Novel Measurement Method For Flexoelectric Coefficients of Nematic Liquid Crystals", *Jpn. J. Appl. Phys.* **37**, 1865
Taylor, L, Richardson, R, Ebbutt, J and Jones, JC	1996	"X-ray diffraction studies of surface stabilised ferroelectric liquid crystals in both low and high pre-tilt devices.", *Ferroelectrics*, **180**
Tsvetkov, V	1942	*Acta Physicochim* (USSR) **16, 132**
Van Doorn, CZ	1975	"Dynamic Behaviour of Twisted Nematic Liquid Crystal Layers in Switched Fields", *J. Appl. Phys.* **46**, (9), 3738
Van Sprang, HA and Koopman, HG	1988	"Experimental and Calculated Results for the Dynamics of Oriented Nematics with Twist Angles from 210° to 270°", *J. Appl. Phys*. **64** (10) 4873
Vertogen, G and de Jeu, WH	1988	"*Thermotropic Liquid Crystals, Fundamentals*", Springer-Verlag, Berlin
Walton HG and Towler MJ	2000	"On the Response Speed of Pi-Cells", *Liq. Cryst.* **27** (10) 1329

Welford, KR	1986	"*Optical Modes of Layered Structures Containing Nematic Liquid Crystals*", Ph.D. Thesis, University of Exeter.
Welford, KR and Sambles, JR	1987	"Detection Of Surface Director Reorientation In A Nematic Liquid-Crystal", *Appl. Phys. Lett.* **50**, 871
Welford, KR and Sambles, JR	1987	"Analysis of Electric Field Induced Deformations in a Nematic Liquid Crystal for any Applied Field", Mol. Cryst. Liq. Cryst. **87**, (147), 25
Welford, KR and Sambles, JR	1987	"Detection of Surface Director Reorientation in a Nematic Liquid Crystal", *Appl. Phys. Lett*. **50** (14) 871
Welford, KR, Sambles JR and Clark MG	1987	"Guided Modes And Surface Plasmon-Polaritons Observed With A Nematic Liquid-Crystal Using Attenuated Total Reflection", *Liq. Cryst*. **2**, 91
Yang, F, Ruan, L and Sambles JR.	2001	"Homeotropic Polar Anchoring Energy of a Nematic Liquid Crystal Using the Fully-Leaky Waveguide Technique", *J. Appl. Phys.* **88** (11) 6175
Yang, FZ and Sambles, JR	1993	"Optical Characterisation of Liquid Crystals by Means of Half-Leaky Guided Modes*", J. Opt. Soc. Am. B,* **10** 858

Yang, FZ and Sambles, JR	1999	"Optical Fully Leaky Characterisation of a Standard Liquid Crystal Cell", *J. Opt. Soc. Am*. B, **16**, 3
Yang, FZ, Ruan, LZ and Sambles, JR	2000	"Homeotropic Anchoring of a Nematic Liquid Crystal Using the Fully-Leaky Waveguide Technique*", J. Appl. Phys*. **88**, 11
Yang, FZ, Sambles, JR and Bradberry, GW	1999	"Half-Leaky Guided Wave Determination of Azimuthal Anchoring Energy and Twist Elastic Constant of a Homogeneously Aligned Nematic Liquid Crystal*", J. Appl. Phys*. **85**, 2

Appendix I

Relationship Between Miesowicz and Leslie Notations

As the six Leslie coefficients do not relate to specific physical situations, they cannot be measured directly. Therefore, when quantifying the nematodynamics of a liquid crystal system, it is preferable to use the five Miesowicz coefficients described in chapter 6. The relationship between the Miesowicz coefficients ($\eta_1, \eta_2, \eta_3, \eta_{12}$ and γ_1) and Leslie coefficients ($\alpha_1, \alpha_2, \alpha_3, \alpha_4, \alpha_5$ and α_6) are as follows:

$$\eta_1 = \frac{-\alpha_2 + \alpha_4 + \alpha_5}{2} \qquad \eta_2 = \frac{-\alpha_3 + \alpha_4 + \alpha_6}{2} \qquad \eta_3 = \frac{\alpha_4}{2}$$

$$\eta_{12} = \alpha_1 \qquad \gamma_1 = \alpha_3 - \alpha_2$$

From thermodynamic arguments, certain restrictions apply to the possible values that the Leslie coefficients can take, as shown below (Leslie, 1979). In particular, η_1, η_2, η_3 and γ_1 must be positive, whilst η_{12} can be positive or negative.

$$\alpha_4 > 0 \qquad 2\alpha_1 + 3\alpha_4 + 2\alpha_5 + 2\alpha_6 > 0$$

$$2\alpha_4 + \alpha_5 + \alpha_6 > 0 \qquad 4\gamma_1(2\alpha_4 + \alpha_5 + \alpha_6) > (\alpha_2 + \alpha_3 + \alpha_5 + \alpha_6)^2$$

$$\eta_{12} + 2(\eta_1 + \eta_2) > \eta_3 + \gamma_1 \qquad \gamma_1[2(\eta_1 + \eta_2)] > (\eta_2 - \eta_1)$$